POLITECNICO DI TORINO

Master's Degree in Aerospace Engineering

Academic year: 2021/2022

Realization and validation of a breadboard able to simulate the LISA constellation acquisition from the optical point of view

Supervisors:

Fabrizio Stesina

Candidate:

Valentina Antetomaso

Table of Contents

List of Figures

List of Tables

Abstract

This paper is the result of seven months of activity I have completed at the *Optics and Science Solutions Unit* of *Thales Alenia Space Italia*, in Turin. The thesis topic is part of a research program whose main goal is the development of a modular integrated approach to design Pointing, Acquisition & Tracking systems, capable to satisfy the strict pointing and stability requirements of the new generation of space optical payloads.

The *Laser Interferometer Space Antenna* (*LISA*) mission is the best present paradigm of this evolution of optical pointing. Thus, the main objective of this thesis is the realization and validation of a breadboard able to simulate the LISA constellation acquisition from the optical point of view.

This document analyzes the implementation of a test system able to emulate the LISA mission configuration. Furthermore, it outlines the development of the detection software ensuring the proper identification of the target laser beam. In conclusion, it validates the simulation breadboard to demonstrate the optical link acquisition capability in representative conditions. This report is organized as follows:

- the *"Problem Formulation"* chapter introduces the main subject of the research program. It identifies the goals of the thesis and the criticalities that could prevent the objectives from being achieved;
- the *"Setup and Methodologies"* chapter outlines the configuration of the final breadboard. Furthermore, this analyzes the acquisition software able to guarantee the proper identification of the target laser spot;
- the *"Experiments & Results"* chapter outlines the structure of the system control application developed under National Instruments LabVIEW software. Furthermore, it summarizes the results of the validation of the final breadboard;
- the *"Conclusions & Recommendations"* section identifies the major achievements of the thesis and suggests some topics to fix aiming at improving and continuing the research program activity.

1. Problem Formulation

Since the development of the first lasers, optical communications technology (*e.g.*, lasercom) imposed itself as the future of deep-space applications, such as the connection between remote spacecraft for metrology purposes or the rising market of space optical communication. Compared to radio frequency (RF) communication links, the use of lasers can significantly increase the efficiency in delivering the signal energy. This results as the lasercom links use higher carrier frequencies, which cause a much smaller diffraction loss and, thus, a much narrower beamwidth. Therefore, the optical links can concentrate a huge amount of power in a small solid angle, achieving a higher efficiency with a lower transmit power and aperture size.

However, the lasercom systems demand more challenging design requirements than common RF communication systems. Establishing an optical link across space, through very long distances, is extremely difficult. Because the beams spread as the square of the distance, the transmitting optics needs a larger diameter and higher power lasers to increase the isotropically radiated power (EIRP). As the beam divergence is proportional to λ_{laser}/D_{tx} (where λ_{laser} is the transmitted laser wavelength and D_{tx} is the optical transmitting aperture diameter), increasing the D_{tx} to achieve higher EIRP results in a narrower divergence and, thus, more strict pointing requirements. To efficiently deliver the signal, the transmitter allowable error shall be equal to a small fraction of the transmit beamwidth. For a typical deep space lasercom mission, the latter is on the order of a few microradians: thus, the desired accuracy is almost equal to some sub-microradians. Furthermore, this precision shall be achieved and stabilized in the presence of the spacecraft's platform jitter and vibrations, whose magnitude is typically several orders larger than the required accuracy.
In conclusion, the new generation of space optical payloads has the potential to achieve fine pointing at the level of the μrad or a fraction of it, but this goal cannot be fulfilled if an adequate stabilization system does not support the optical squeezed powerful beam.

Pointing is the dominant challenge of deep-space optical communication. The more promising approach for stabilizing a very narrow beam uses natural and artificial celestial sources, inertial and optical sensors, and beam steering and stabilization actuators [1]. The problem of pointing is double: jitter isolation/rejection and precision beam-pointing stabilization. The satellite's platform jitter and vibrations shall be rejected and isolated to stabilize the transmit line of sight (LOS) in inertial space. Then, a dedicated sub-system shall point the stabilized LOS towards the receiver. In practice, the hybrid architecture joins weak beacon tracking and inertial sensors to monitor high-frequency disturbances. Thus, the optical instruments ensure the desired resolution, and the additional systems provide the requested bandwidth. This approach also includes the use of some celestial sources (*e.g.*, Earth, stars) as absolute pointing references.

The study of the tight stability requirements of space optical payloads is the main subject of the *"Fine Pointing Acquisition and Tracking"* program of *Thales Alenia Space Italia*. Its main goal is the development of a modular integrated approach to design Pointing, Acquisition & Tracking sub-systems (PAT) able to fix the issue of optical pointing and be integrated into existing mission frameworks. The long-term objective is to create the basis of a system-level

approach to the problem of analyzing specific PAT solutions and provide a valuable tool to conceive a fully integrated hybrid architecture.

The thesis activity is part of the described *"Fine Pointing Acquisition and Tracking"* program. As the *Laser Interferometer Space Antenna* (*LISA*) mission is the best present example of this increasing evolution of optical pointing, this was selected as the first framework to benefit from the achievements of the proposed activity. Therefore, this paper deals with the design of a Pointing, Acquisition & Tracking system with specific application to the constellation acquisition stage of LISA.

1.1 LISA Mission

1.1.1 Introduction

Laser Interferometer Space Antenna (LISA) is a space mission of discovery jointly envisaged by ESA and NASA, whose main objective is to detect and observe gravitational waves in the low-frequency range, between 0.1 mHz and 1 Hz. Seismic and human-generated noises make this interval inaccessible from common ground-based detectors, which are very sensitive to high frequencies. Thus, LISA will be the first space-based observatory to open a gravitational window on the Universe in the low-frequency regime. This corresponds to the waves emitted by the most violent events, such as the coalescence of massive black holes, the capture of stellar-size compact objects, and the signal from binary systems in our galaxy.

Gravitational waves originate typically from powerful collisions that create distortions in space-time: since they hardly interact with matter, they are also extremely difficult to detect. Their presence is manifested through the effects they produce on the bodies around them. Measuring the change in the distance of spatially separated objects is a common concept to quantify the impact of gravitational waves.

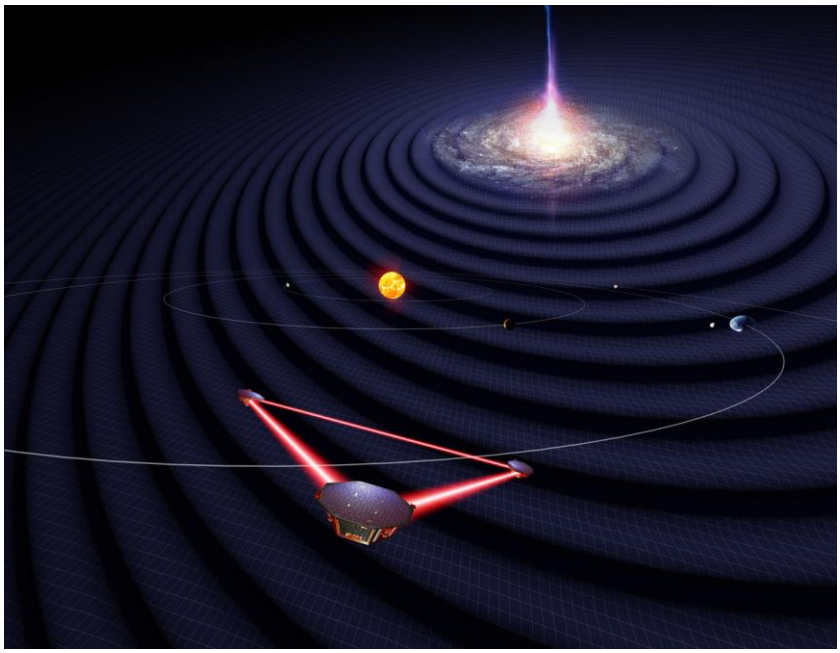

Figure 1. *Artist's impression of the LISA mission satellites in the solar system observing gravitational waves from a distant galaxy.*
CREDIT: University of Florida/Simon Barke.

The LISA mission measurement technique consists of a laser interferometry system, which is based on three satellites flying in a triangular constellation. They form a huge Michelson interferometer. Each spacecraft houses two Optical Assemblies (OA), each containing a test mass (TM). The two masses are free-falling controlled along their geodesics and form the reference points for interferometric measurement of the inter-spacecraft distance. A dedicated Drag Free System ensures the external and internal disturbance rejection.

Gravitational waves cause the length of the optical path between these proof masses to change, and the laser interferometers of both directions of each constellation arm evaluate this pm to nm pathlength variations. The total TM-TM measurement along each side of the triangle comprises:

- the local distance between the optical bench of the first satellite and the TM1 (e.g., d_1 in **Figure 2**);
- the arm distance, *i.e.* the measure between the optical benches of the two spacecraft (e.g., d_{12} in **Figure 2**);
- the local distance between the optical bench of the second satellite and the TM2 (e.g., d_2 in **Figure 2**).

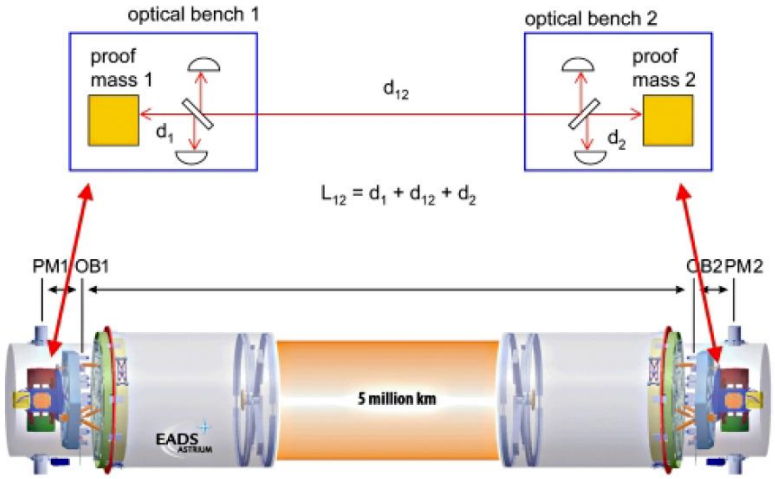

Figure 2. *LISA measurement principle along one interferometer arm. The actual arm length is 2.5e10^6km. CREDIT: EADS Astrium.*

The science of LISA is beyond the scope of this paper and is discussed in detail in [2 - 3].

1.1.2 LISA Constellation Acquisition

LISA comprises three identical spacecraft in a heliocentric orbit trailing the Earth by about 20° and inclined by 60° with respect to (*i.e.*, *w.r.t.*) the ecliptic (**Figure 3**). The three satellites are located at about $50e10^6$ from our planet and form a triangular configuration, whose arm length is equal to $2.5e10^6\ km$. Their orbit is optimized to cause the constellation to maintain its size and shape closely for the nominal duration of the mission. The measure between the triangle center and the Sun is about 1AU, which is the distance from Earth to the Sun (**Figure 4**).

Once the spacecraft reached their correct orbits, they shall prepare to form a single working observatory. This stage includes constellation acquisition [4-5]. The interferometric measurements can start once acquiring the optical links between the three spacecraft on the six quadrant photodiodes (QPD) (one for each optical bench, *i.e.* one for each telescope), which are used as detectors to measure the text masses pathlength variations with high sensitivity. The

constellation acquisition is sequential because it establishes one laser link at a time in an arbitrary order.

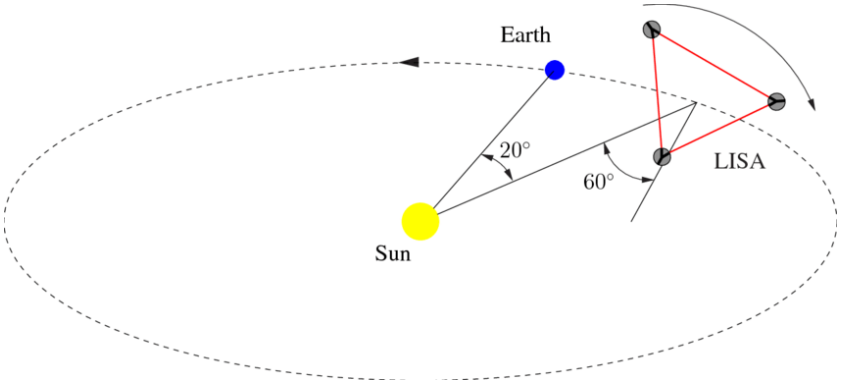

***Figure 3**. LISA constellation orbit-1.*

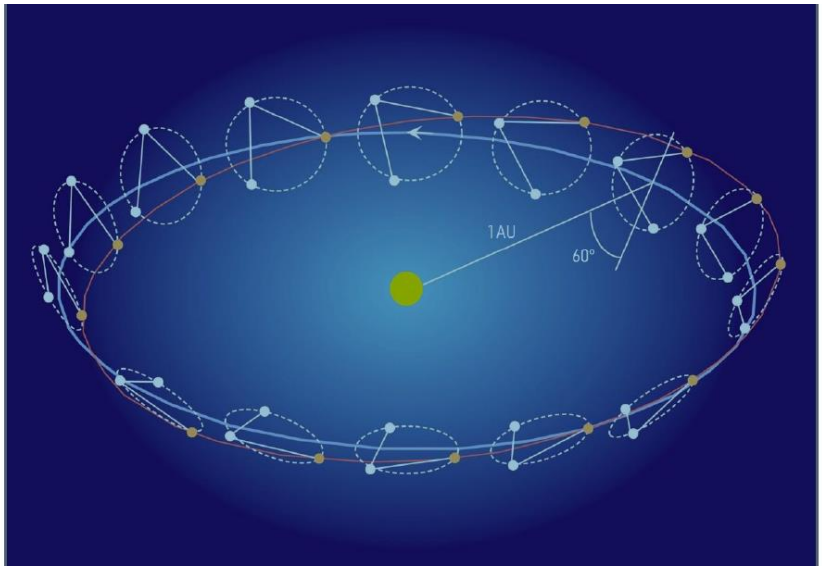

***Figure 4.** Lisa constellation orbit-2.*

The LISA program proposes to use start trackers, CCD detectors, and quadrant photodiodes to achieve laser signal acquisition. This phase is strongly demanding due to the extremely long distance and the laser beam pointing issue. The QPD are not available until receiving a continuous signal and their field of view (FOV) is smaller than the laser beam cone size. Therefore, with such a long distance, detecting the transmitting beam is initially possible with the help of navigation data. A star tracker, together with an optical assembly tracking mechanism (OATM), acts as an auxiliary coarse attitude device when no links are acquired. However, the orbit determination uncertainties and the attitude sensor accuracy introduce some limitations. The portion of the sky where the remote spacecraft is expected to be located is larger than the cone size of the emitted beam. Thus, the acquisition cannot be direct, but the transmitting satellite (*e.g.*, SC1) shall perform a scanning manoeuvre to cover the whole uncertainty area. While the transmitting spacecraft is moving to make itself identifiable by the receiving satellite (*e.g.*, SC2), the latter is also carrying out its scanning manoeuvre. This further complicates the laser signal acquisition.

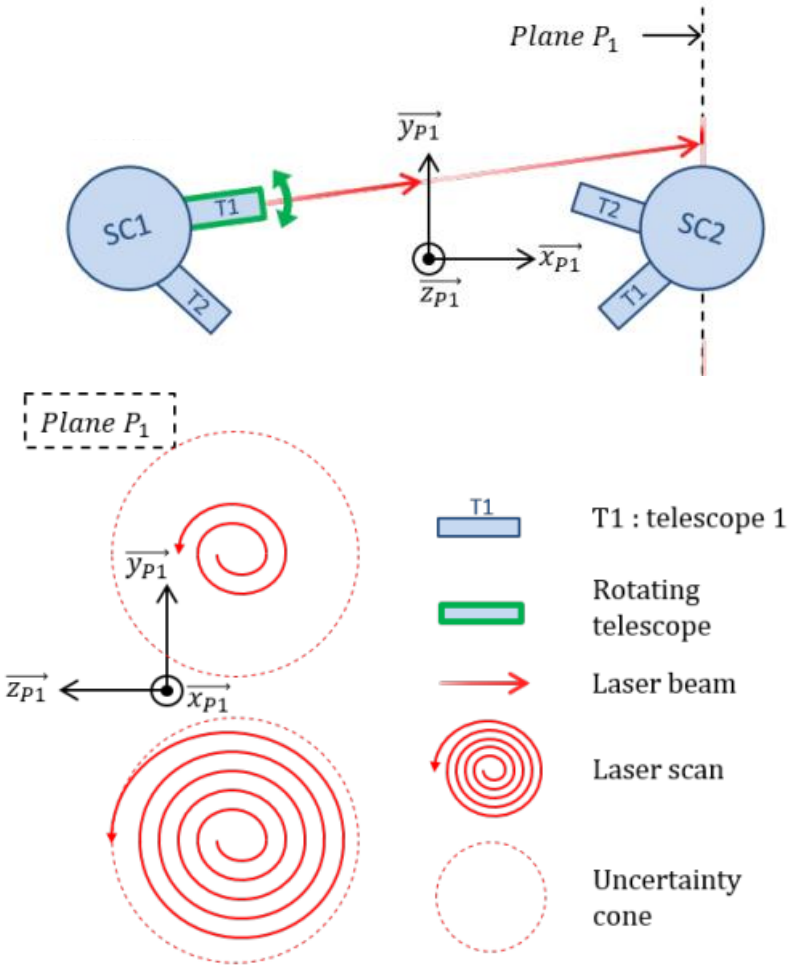

***Figure 5**. Single-link acquisition. Transmitting satellite's scanning manoeuvre.*

In this stage, a fine accuracy acquisition device, called Constellation Acquisition Sensor (CAS), allows for laser pointing determination. As the field of view of this Charged-Coupled Device (CCD) is far larger than the QPD, firstly capturing the signal on this reduces the operating time. The CAS enables laser acquisition only when the beam is visible on the sensor. In the case of no signal, the scanning phase proceeds until achieving the beam detection.

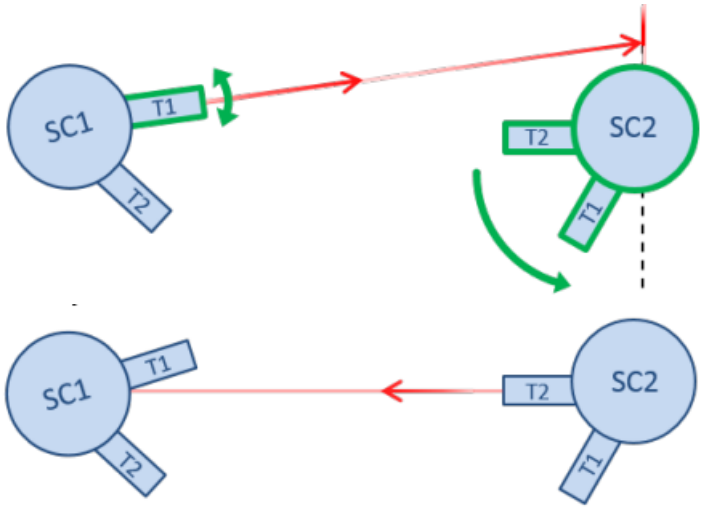

***Figure 6**. Single-link acquisition. Receiving satellite's attitude correction.*

At a certain time, the receiving satellite identifies the laser spot on its CCD, with an offset from the expected reference position. This gap is accurately derived by computing the centroid of the receiving signal and then suppressed by the attitude actuators. Thus, the CAS measurement allows to center the received beam onto the FOV of the quadrant photodiode.

Once applying the attitude correction, the receiving satellite is pointed towards the transmitting spacecraft. Thus, the latter can detect the laser spot of the receiving satellite on its Constellation Acquisition Sensor, and then execute the proper attitude correction by steering its telescope to the updated reference direction.
Then, laser acquisition is accomplished along one arm of the triangular formation.

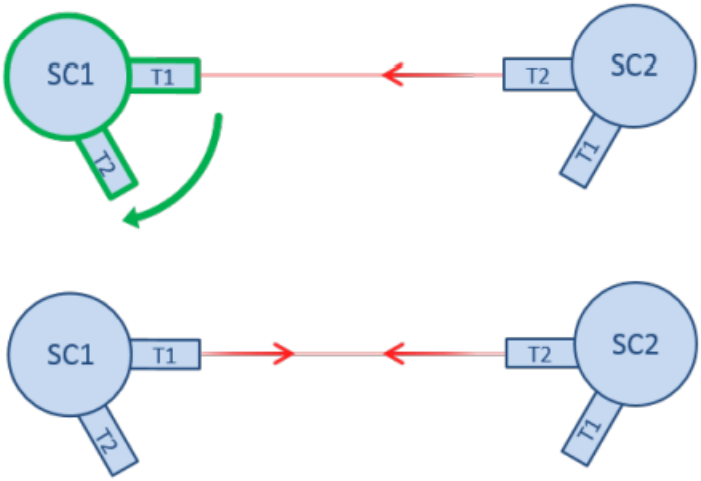

Figure 7. *Single-link acquisition. Transmitting satellite's attitude correction.*

The LISA constellation acquisition is extremely challenging: the beam divergence over several millions km limits the received power to some 100 pW. Furthermore, as the uncertainty area of the spacecraft to be detected is larger than the laser beam cone size, a scanning manoeuvre is needed. The receiving satellite can identify the transmitting spacecraft just when its laser cone invests it.

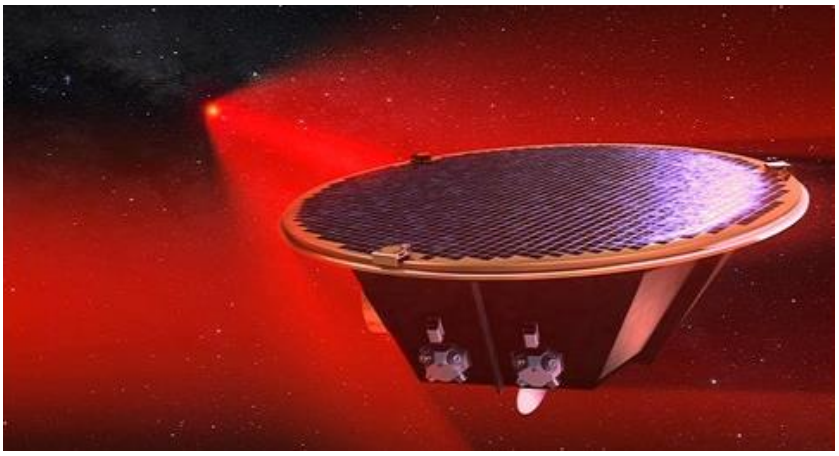

Figure 8. *Artist's impression of a LISA mission concept spacecraft. CREDIT: AEI/Milde Marketing/Exozet.*

The profile of the optical intensity in a plane perpendicular to the beam axis can be described with a Gaussian function. Thus, when the laser cone of the transmitting spacecraft crosses the receiving satellite, its Constellation Acquisition Sensor detects a signal whose intensity varies according to a normal distribution curve. Thus, the transmitting laser beam appears as a beacon. The dynamics of laser pointing induce a modulation of the target source power, drastically reducing the time this is visible at its maximum intensity. Furthermore, in deep space, the number of photons is limited with respect to the noise sources. Therefore, the main issue of the LISA constellation acquisition is the detection of a sub-picowatt variable beam that is embedded in a strongly noisy environment.

1.2 Thesis objectives

The main goal of this thesis is the development of a test facility able to simulate the LISA constellation acquisition, from the transmitting satellite's scanning phase to the attitude correction stage, which is performed by the receiving spacecraft to center the detected spot on the FOV of the QPD sensor. The basic breadboard shall include:

- light source;
- Electronics Variable Attenuator for the attenuation control of the power source;
- piezo tip/tilt platform for noise generation (*e.g.*, the second piezo platform);
- piezo tip/tilt platform for noise correction (*e.g.*, the first piezo platform);
- camera.

The setup shall be fully controlled from a Windows-based workstation connected via Ethernet to a National Instruments (NI) CompactRIO real-time platform. The system control application shall be programmed in LabVIEW development environment. The breadboard shall emulate the LISA mission configuration to demonstrate the link acquisition capability in representative conditions:

- detection of sub-picowatt variable beams;
- noise sources (*e.g.*, background, Straylight, electronics);
- secondary sources (*e.g.*, stars);
- platform jitter.

Starting from the proposal above, the identified primary and secondary goals of the thesis are:

- ***Primary objectives***
  - ✓ Realization and validation of a breadboard able to simulate the LISA constellation acquisition from the optical point of view. The setup shall mimic the mission configuration to demonstrate the link acquisition capability in the following conditions:

    - detection of sub-picowatt variable beams;
    - noise sources (*e.g.*, background, Straylight, electronics);
    - secondary sources (*e.g.*, stars).

    The basic setup shall:

    - simulate the dynamics of the scanning manoeuvre of the satellite to be detected by translating the spiral orbit of the platform into an intensity law for the power source;
    - simulate the dynamics of the laser pointing of the receiving satellite by translating the scanning orbit of the platform into a displacement law for the piezo tip/tilt platform;
    - validate the target identification software against noise sources and secondary sources;
    - simulate the receiving satellite's pointing correction once the beam acquisition is achieved. The introduced reference position shall emulate the CAS pixel corresponding to the FOV of the quadrant photodiode.

- ✓ Development of software able to guarantee laser spot identification in representative conditions. The software shall be developed in C language, to be successfully included into a pre-existing focal plane simulator.

- ***Secondary objectives***
  - ✓ Simulation of the sending satellite's platform jitter to induce a fluctuation of the transmitting beam intensity. Noise generation is accomplished by a dedicated piezo tip/tilt platform;
  - ✓ Compensation of the sending satellite's platform jitter.

The secondary objectives concerning the platform's noise generation and rejection were not analyzed. For the LISA application case, the perturbations due to the spacecraft's dynamics are negligible: thus, the second piezo tip/tilt platform of the basic breadboard acts as a simple mirror in the final setup configuration.

1.2.1 Critical issues

The critical issues that can prevent the satisfaction of the primary objectives of the thesis are:

- ✓ *Detection of sub-picowatt variable beams*

  The main topic of the LISA constellation acquisition is the detection of a significantly weak and infinitely small point laser source. Due to the long propagation distance, at the CCD surface, the laser power is as weak as 100 pW. Furthermore, each satellite shall perform a scanning manoeuvre to cover the whole uncertainty area where the remote spacecraft is expected to be found. This causes both a modular variation of the intensity of the transmitting source and the movement of the field of view of the CAS of the receiving satellite, affecting the performance of the target detection process. Thus, effective software for the identification of sub-picowatt variable beams is needed. The introduced mathematical models are detailed at the pixel level, to be integrated in the previously developed focal plane simulator.

  The first part of the thesis activity was carried out ignoring the exact speed of the satellites' scanning manoeuvre. Thus, some assumptions led to the development of the target acquisition preliminary software.

- ✓ *Noise sources*

  The laser beam shall be detected in a strongly noisy environment. Furthermore, the laser power is weak and subject to modular variation. Thus, the target acquisition process needs effective noise mitigation and Signal-to-Noise ratio enhancement techniques.

  The first part of the thesis activity was conducted ignoring the future introduction of one of the most critical noise sources: the laser speckle [6]. A "speckle pattern" is a random intensity distribution that forms when coherent light is either reflected from a rough surface or propagates through a medium with random refractive index fluctuations. In this work, we are concerned with laser speckle patterns that originate when coherent light is scattered by rough surfaces. For the LISA application case, this roughness arises from a

phenomenon of surface contamination. When a plan is illuminated by a light beam, according to diffraction theory, each point acts as a source of secondary spherical waves. The speckle effect is the result of the interference of many different reflected wavefronts of the incident beam. These have the same frequency, different phases, and amplitudes, and add together to give a resultant wave whose amplitude, and therefore intensity, varies randomly. The figure below shows the typical structure of the laser speckle.

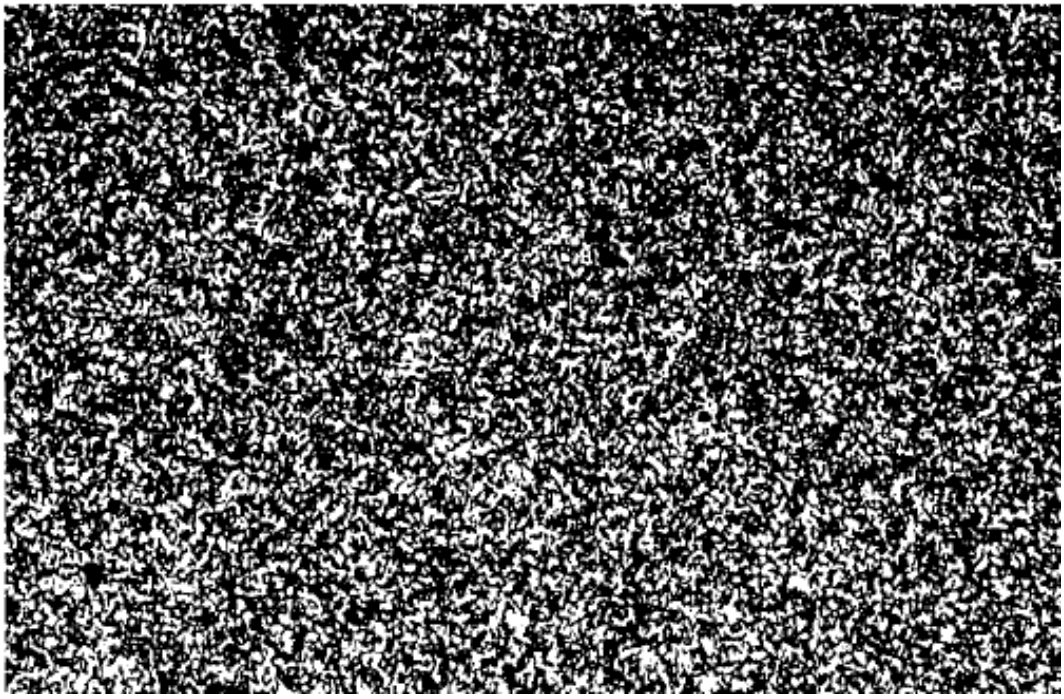

***Figure 9**. Typical structure of the laser speckle pattern.*

The speckle has a peculiar granular appearance, which seems chaotic and unordered: its pattern is quite like a random distribution of ideal point-spread functions (PSF), covering the whole satellite's FOV. These PSFs can be seen as secondary sources, whose size and intensity are completely random. Therefore, they can be strong and equally distributed enough to prevent target identification. The introduction of the laser speckle caused a significant modification of the beam detection preliminary software. Since the exact amount of reflected radiation can be evaluated only after performing Straylight rigorous analysis, the acquisition final algorithm was developed using properly normalized patterns. They were scaled to emulate the LISA mission representative condition: a random intensity distribution whose strength is almost always greater than the beam being detected.

The laser speckle can vary over time if some changes occur to the "roughness" that originated it. For the LISA application case, it is supposed that the intensity pattern can be modified from thermoelastic phenomena. As these have a slow evolution over time, the speckle is assumed to be fixed and unchanged during the constellation acquisition stage.

- ✓ *Secondary sources*

  The need to differentiate the target beam from secondary sources is one of the main criticalities of the LISA constellation acquisition. The ideal point-spread function of an infinitely small point laser source has the same appearance as stars on the CAS detector. Therefore, the observable secondary sources in the satellite's field of view can be of the same size and strength as the laser spot. Thus, an effective method for the identification and removal of secondary sources shall be developed.

- ✓ *Fine pointing requirements*

  The LISA constellation acquisition has very strict pointing and stability requirements. As the receiving satellite detects the laser spot on its CCD, its centroid must be accurately determined, and the computation precision shall be $\leq$0.1 pixels to center the beam onto the FOV of the quadrant photodiodes. However, centroid accuracy is proportional to the Signal-to-Noise ratio: in deep space, the noise sources are greater than the number of photons, and the target beam power is reduced by the long propagation distance. Thus, an effective centroid computation under weak light conditions is essential for the success of LISA.

- ✓ *Real-time centroid computation*

  The target identification and the laser spot centroid estimate shall deal with the real-time requirement, to properly guarantee the success of the LISA constellation acquisition. Therefore, the image processing and centroid computation techniques shall be selected after carefully considering their computational cost.

2. Setup and Mathematical models

The second chapter describes the changes applied to the basic setup (1.2) to emulate the LISA mission configuration. Furthermore, it outlines the steps leading to the development of the target identification software.

The first section (2.1) shows the final breadboard configuration. This is organized as follows:

- *Hardware configuration,* which describes the installed devices, their main characteristics, and their functions in the simulation of the LISA constellation acquisition;
- *Software configuration,* which summarizes the specifications of the NI LabVIEW software used to program the breadboard control application.

The remaining paragraphs analyze the selected solutions to achieve the second primary goal of this thesis: the development of software able to guarantee the proper identification of the target beam in representative conditions.

Section 2.2 describes the proposed method to estimate the laser spot position. It consists of the traditional centroid calculation process, with a partial modification to the dimension of the computational domain. This paragraph outlines the arguments leading to the choice of the improved method, with careful consideration of the need for the satisfaction of the LISA mission strict pointing and real-time requirements.

Paragraph 2.3 is a brief of the target identification preliminary strategy. Its core concept includes the identification and characterization of all visible light sources captured by the receiving satellite's CAS. The Canny edge operator was selected as a fast technique to identify multiple spots; the improved centroid computation method was chosen to characterize the position of each light beam on the CCD reference system. A spot centroid prediction algorithm joins the central core of the preliminary software. This allows the identification of the same light source in subsequent frames after its shift due to the spacecraft's scanning manoeuvre. A detailed analysis of all the stages characterizing the target acquisition preliminary algorithm is provided in this chapter.

The last section (2.4) describes the beam acquisition final software and outlines the reasons that led to the selection of each introduced noise mitigation or Signal-to-Noise ratio enhancement technique. In conclusion, paragraph 2.4.6 demonstrates the effectiveness of the proposed algorithm. The implemented performance analysis identified the pros and cons of each step of the detection software, leading to effective optimization of its control parameters. This resulted in the assessment of the optical link acquisition capability and the establishment of the limits of the suggested target identification process.

2.1 Breadboard description

2.1.1 Hardware configuration

Figure 10 shows a sketch of the final breadboard able to simulate the LISA constellation acquisition.

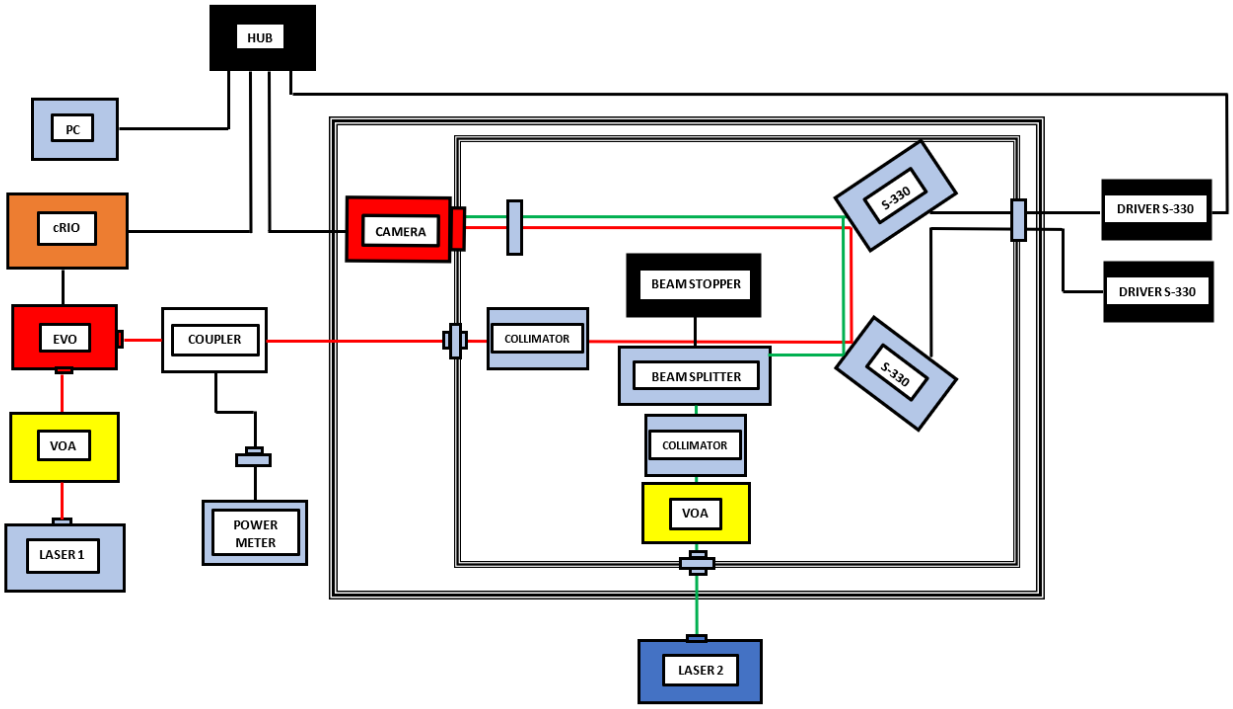

Figure 10. *Sketch of the LISA constellation acquisition breadboard.*

The control system is based on a CompactRIO NI cRIO-9039 platform (labeled as "cRIO" in **Figure 10**). A CompactRIO (*e.g.*, cRIO) is an embedded system containing three components: a processor running a real-time operating system (RTOS), a reconfigurable Field Programmable Gate Array (FPGA), and interchangeable industrial I/O modules. It provides processing capabilities and sensors I/O suitable for control applications in rugged environments.

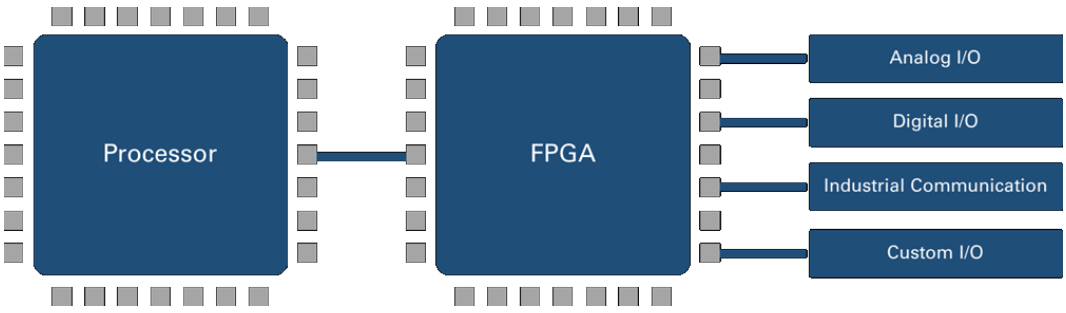

Figure 11. *Heterogeneous architecture of a cRIO platform.*

The NI cRIO-9039 is equipped with a 1.91 GHz Quad-Core Intel Atom Central Processing Unit (CPU) and an FPGA Xilinix Kintex-7. The real-time processor runs the NI Linux Real-Time 64-bits OS (*i.e.*, Operative System). The controller is equipped with 8 slots, one Mini DisplayPort, an SDHC slot, two Gigabit Ethernet,

two USB hosts, one USB 2.0 device, two serial ports, an RS-232 at 115200 bps, and one RS485/422 at 115200 bps.

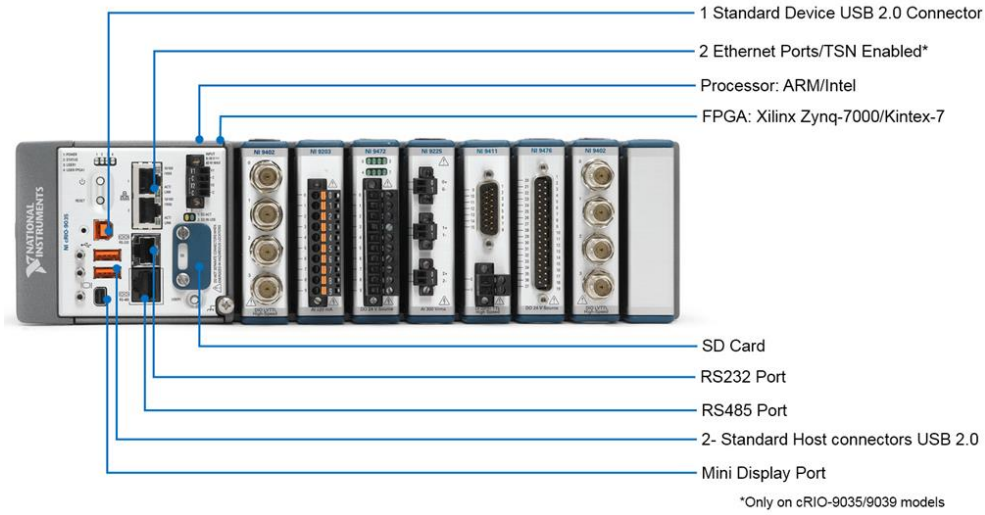

***Figure 12**. NI-cRIO platform.*

The NI 9269 isolated module for the C Series chassis is plugged in one of the cRIO available slots and commands an Electronic Variable Attenuator (labeled as "EVO" in **Figure 10**).

The system architecture incorporates a human-machine interface, which is a Windows-based computer, called a workstation (named "PC" in **Figure 10**).
It allows the operator to monitor the proper function of the simulation and send commands to the embedded system and other devices. The workstation communicates to the CompactRIO hardware with the Ethernet protocol through a connection hub (*e.g.*, "HUB" in **Figure 10**).

The main station also controls the first piezo tip/tilt platform (*e.g.*, the one at the top right in **Figure 10**) and the image acquisition process of the camera.
The installed piezo device is the *S-330.2SH* model of the Physik Instrument (PI) and is controlled by the "E-727 Digital Multi-Channel Piezo Controller". It is a high-dynamics platform equipped with strain gauge sensors, whose tip/tilt range is equal to 2 $mrad$. The following table shows its main specifications.

Piezo Tip/Tilt platform	
Model	*Physik Instrument*/S-330.2SH
Tip/tilt angle in closed-loop θ_x, θ_y, closed-loop [$mrad$]	2
Resolution in θ_x, θ_y, closed-loop [μrad]	0.05
Linearity error in θ_x, θ_y [%]	0.05
Ceramic type	PICMA
Operating temperature range [$°C$]	-20/80

***Table 1**. Piezo Tip/Tilt platform specifications.*

The first tip/tilt platform acts in the succeeding stages of the LISA constellation acquisition to perform different operations. In the first phase, until identifying

the target beam, it mimics the spiral movement of the FOV of the receiving spacecraft. After acquiring the target, the pointing stage begins, and the platform simulates the position correction performed by the receiving satellite's attitude actuators. This results in the centering of the transmitting laser spot in the FOV of the quadrant photodiodes detector.

The test camera (labeled as "CAMERA" in **Figure 10**) acquires the images to be scanned and filtered to search for the target beam. It replaces the Constellation Acquisition Sensor of the receiving satellite. As the mathematical model of the identification software is detailed at the pixel level, the sampled frames are converted to matrices of pixels. The table below summarizes the camera specifications and operating parameters.

Camera	
Model	*MetroLux/*BPC 8301cg
Resolution [*pixel*]	780x580
Sensor	Sony ICX415AL/AQ with HAD technology
Type	Progressive Scan CCD
Cell size [μm]	8.3
Mono format	Mono8, Mono12Packed, Mono12
Exposure control range [μs]	26/60000000
Gain control range [dB]	0/31
Operating temperature range [$°C$]	5/45

Table 2. *Camera specifications and operating parameters.*

The control station displays the sampled images and the output of the detection software.
Both the camera and the digital controller of the piezo platform connect to the workstation through the same hub of the cRIO, as shown in the following figure.

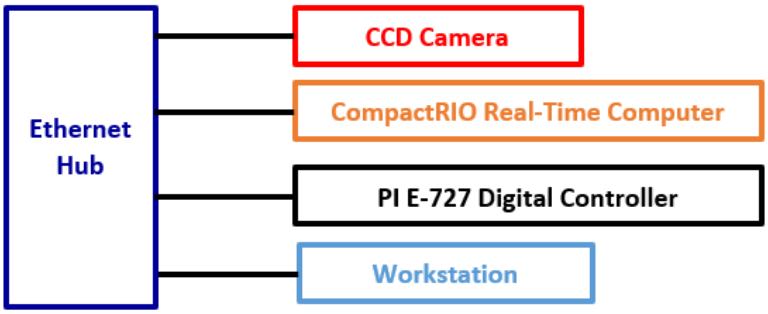

Figure 13. *Test Setup-Ethernet Connections Scheme.*

As can be seen in **Figure 10**, the test setup is equipped with two different laser sources. The first instrument (labeled as "LASER 1") originates the red optical path, which simulates the light beam that is sent by the satellite to be detected.

The power source used in the simulation is an 855 nm laser produced by Thorlabs. **Table 3** shows its specifications and operating parameters.

MCLS Series Multi-Channel Fiber-Coupled Laser Source	
Model	*Thorlabs*/MCLS1-850
Center wavelength [nm]	855
Fiber type	SM800-5.6-125
Active Channel	1
Operating temperature [°C]	25.00
Operating current [mA]	24.39
Fiber output power [mW]	0.100

Table 3. *Target power source specifications and operating parameters.*

As explained in 1.1.2, the dynamics of laser pointing induce a modulation of the transmitting power. Furthermore, the beam intensity is significantly reduced by the long propagation distance. To simulate the LISA mission representative conditions, the laser source is strongly attenuated by a series of devices:

- a Variable Beam Attenuator (named "VOA" in **Figure 10**), which is a passive optical component produced by Thorlabs. It causes the attenuation of the fiber signal ensuring the optical power in a stable level without any changes on its original transmission wave. This device consists of a collimator-based manually variable attenuator: it has a wide range of mitigation levels, available by turning its thumb screw. **Table 4** summarizes the VOA specifications;

Variable Beam Attenuator	
Model	*Thorlabs*/VOA850-FC
Characteristics	Single-Mode Fibres FC/PC narrow key
Wavelength range [nm]	830 – 870
Fiber type	SM800-5.6-125
Attenuation range [dB]	1.8 - 50
VOA technology	Collimator + blocking device

Table 4. *Target source - Variable Beam Attenuator specifications.*

- an Electronics Variable Attenuator (labeled as "EVO" in **Figure 10**), which is an optical instrument designed for single-mode fiber applications. It is produced by Thorlabs and, in the final breadboard, is electronically controlled by the NI 9269 module of the cRIO. While the beam passes through the EVO, a modulating signal is applied to mimic the dynamics of the laser pointing. Unlike usual tracking experiments, in the LISA constellation setup, the scanning manoeuvre of the sending satellite is emulated by translating the spiral orbit of the platform into an intensity Gaussian law for the source. **Table 5** summarizes the EVO specifications;

- a Single-Mode Fused Fiber Optic Coupler (labeled as "COUPLER" in **Figure 10**), which is a variable optical attenuator based on the Micro-Electro-Mechanical System (MEMS) technology. This device can achieve remote control of the power by a MEMS chip with a movable mirror on the silicon. It attenuates the light source by coupling the input beam onto the output fiber. The control voltage acts on the mirror tilt angle, thus on the desired mitigation amount. The main benefits of MEMS instruments are the capability to provide the required accuracy and a wide range of attenuation. **Table 6** summarizes the Fiber Optic Coupler specifications.

Electronics Variable Attenuator	
Model	*Thorlabs*/EVOA800F
Characteristics	Connectors for Single-Mode Fibres FC/PC
Wavelength range $[nm]$	780 – 980

Table 5. *Electronics Variable Attenuator specifications.*

Single-Mode Fused Fiber Optic Coupler	
Model	*Thorlabs*/TW850R1F1
Characteristics	Connectors for Single-Mode Fibres FC/PC
Wavelength band $[nm]$	850 ± 100
Attenuation ratio	99:1 (±0.6%)

Table 6. *Single Mode Fused Fiber Optic Coupler specifications.*

The coupler causes 99% of the beam strength to be transmitted to a Power Meter (named "POWER METER" in **Figure 10**). This device measures the amount of the receiving power, monitoring the attenuation range and the proper dynamics of the laser pointing. The following table shows its specifications.

Power Meter	
Model	*Newport/*POWER_METER_2936-R
Power	100/120/220/240VAC $\pm$ 10%, 50/60 Hz, 70 $Watts$
Display	Graphical LCD ¼ VGA, 5.6 in diagonal, TFT color
Display update rate	≥ 20 Hz
Operating environment	5°C to 40°C; $<$ 70% RH non-condensing
Connectors	Optical Detector 15-Pin D-Sub, BNC Analog Output, Trigger Output Trigger Input, 9-Pin D-Sub RS-232, USB Host, USB Device

Table 7*. Power Meter specifications.*

The remaining 1% of the modulated power represents the target signal to be detected.

Then, the light beam passes through an FC/PC Fiber Collimation Package (labeled as "COLLIMATOR" in **Figure 10**). It consists of a curved lens that narrows the beam causing its alignment in a specific direction. The table below shows the specifications of the collimator.

FC/PC Fiber Collimation Package	
Model	Thorlabs F220FC-850
Focal length [mm]	11.12
Center wavelength [nm]	850

Table 8. *Target source - fiber collimator specifications.*

The narrower beam follows a straight path until it hits the mirror installed on the second piezo tip/tilt platform (*e.g.*, the one at the bottom right in **Figure 10**). This device is the *S-330.2SH* model produced by PI, and its specifications are summarized in **Table 1**. It was originally introduced to simulate the platform's jitter characterizing a more general acquisition and tracking system. As, for the LISA application case, the perturbations due to the satellite's dynamics are recognized as negligible, this tip/tilt platform acts as a simple mirror.

Finally, the laser source is deflected and forced to hit the first piezo tip/tilt platform and then, a focusing lens (f_{lenght} = 50 mm), before entering the FOV of the camera.

The secondary laser source (named "LASER 2" in **Figure 10**) simulates the presence of a star in the FOV of the receiving satellite, to trigger the beam identification process. It generates the green optical path (view **Figure 10**). The secondary source is a 635 nm laser produced by Sch$\ddot{a}$fter&Kirchhoff. The following table shows its specifications and operating parameters.

Laser Diode Collimator	
Model	*Schäfter&Kirchhoff*/58FCM-635-12-N12-P-5-2-20-0-150
Center wavelength [nm]	635
Fiber type	PM single-mode fiber cable, FC-PC connector
Constant power [mW]	12

Table 9. *Secondary source specifications and operating parameters.*

As the laser power of 12 mW is much greater than the primary source strength (view **Table 3**), it is strongly attenuated with a manual device (labeled as "VOA" in **Figure 10**) produced by Thorlabs. This operation allows assessing the effectiveness of the constellation acquisition process with a secondary source, whose power and dimensions are quite like those of the target spot. **Table 10** summarizes the Variable Beam Attenuator specifications.

At the VOA output, the attenuated beam passes through a collimator (view **Table 11**) and then, hits a beam splitter (view **Figure 10**).

Variable Beam Attenuator	
Model	*Thorlabs*/VOA630-FC
Characteristics	Single Mode Fibres FC/PC narrow key
Wavelength range $[nm]$	620 – 650
Fiber type	SM600
Attenuation range $[dB]$	3 - 50
VOA technology	Collimator + blocking device

Table 10. *Secondary source - Variable Beam Attenuator specifications.*

FC/PC Fiber Collimation Package	
Model	*Thorlabs*/F220FC-B
Focal length $[mm]$	10.99
Center wavelength $[nm]$	633

Table 11. *Secondary source - fiber collimator specifications.*

Beam splitters are optical components able to split incident light at a designated ratio into two separate beams. Thus, the green path is deflected to the mirror of the second piezo tip/tilt platform, to follow the same path as the primary source beam and enter the FOV of the camera. The final beam stopper absorbs the remaining intensity.

Real images of the LISA constellation acquisition breadboard are shown below.

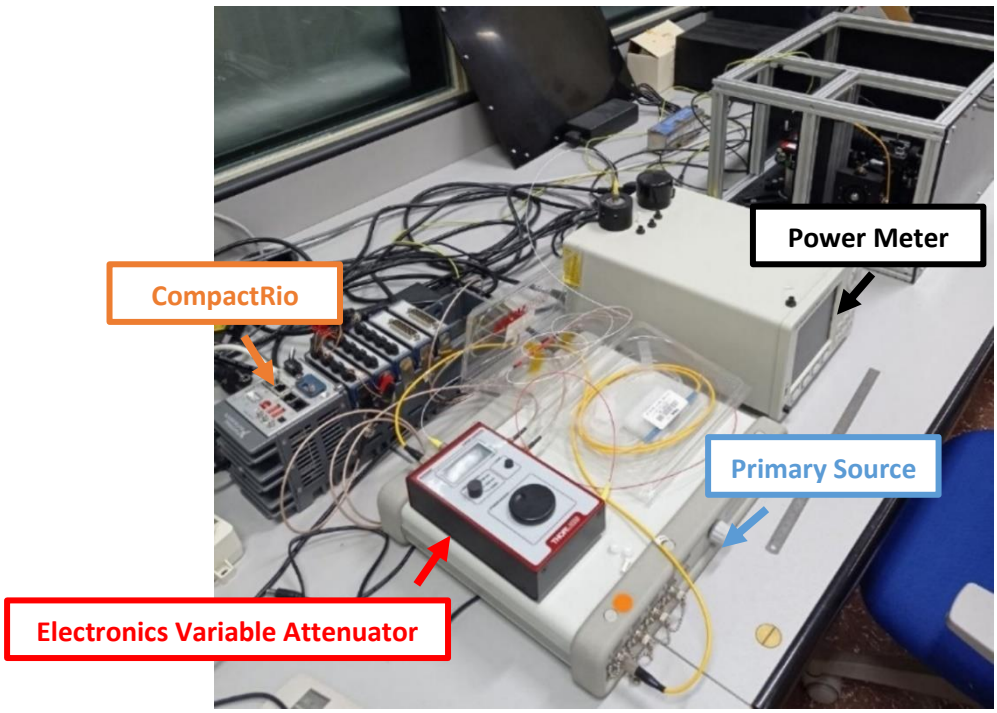

Figure 14*. Test setup-1.*

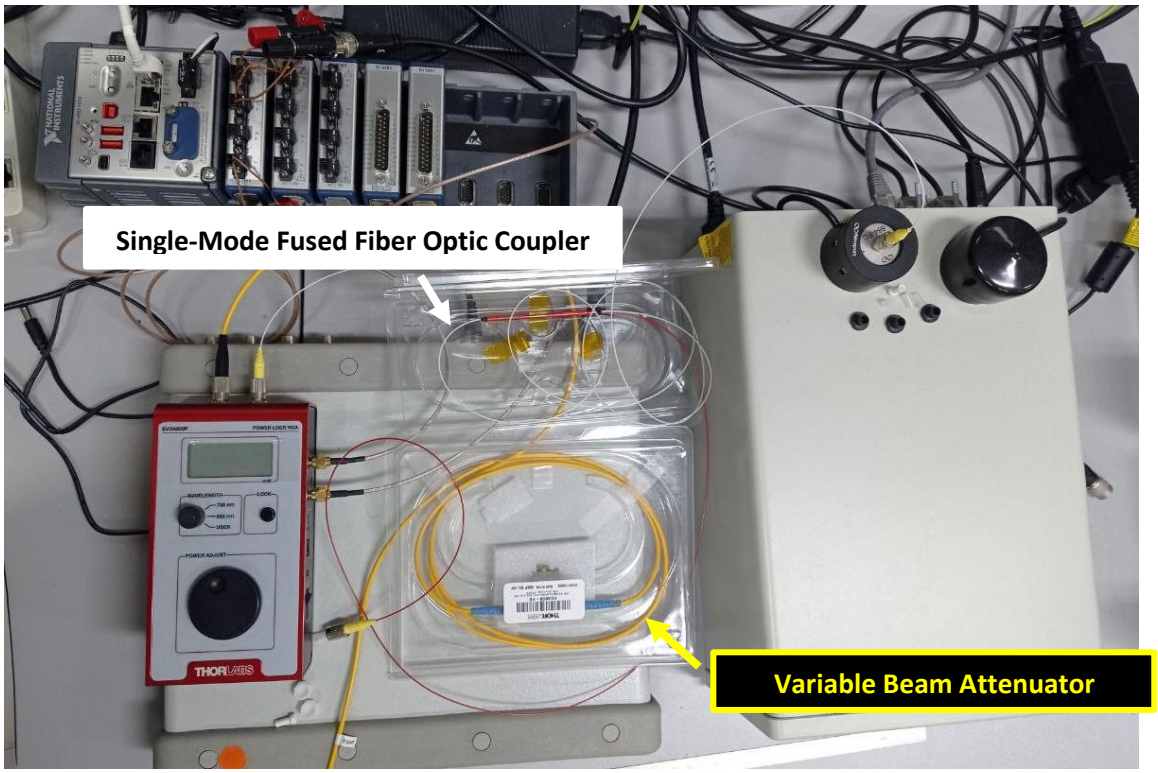

Figure 15. *Test setup-2.*

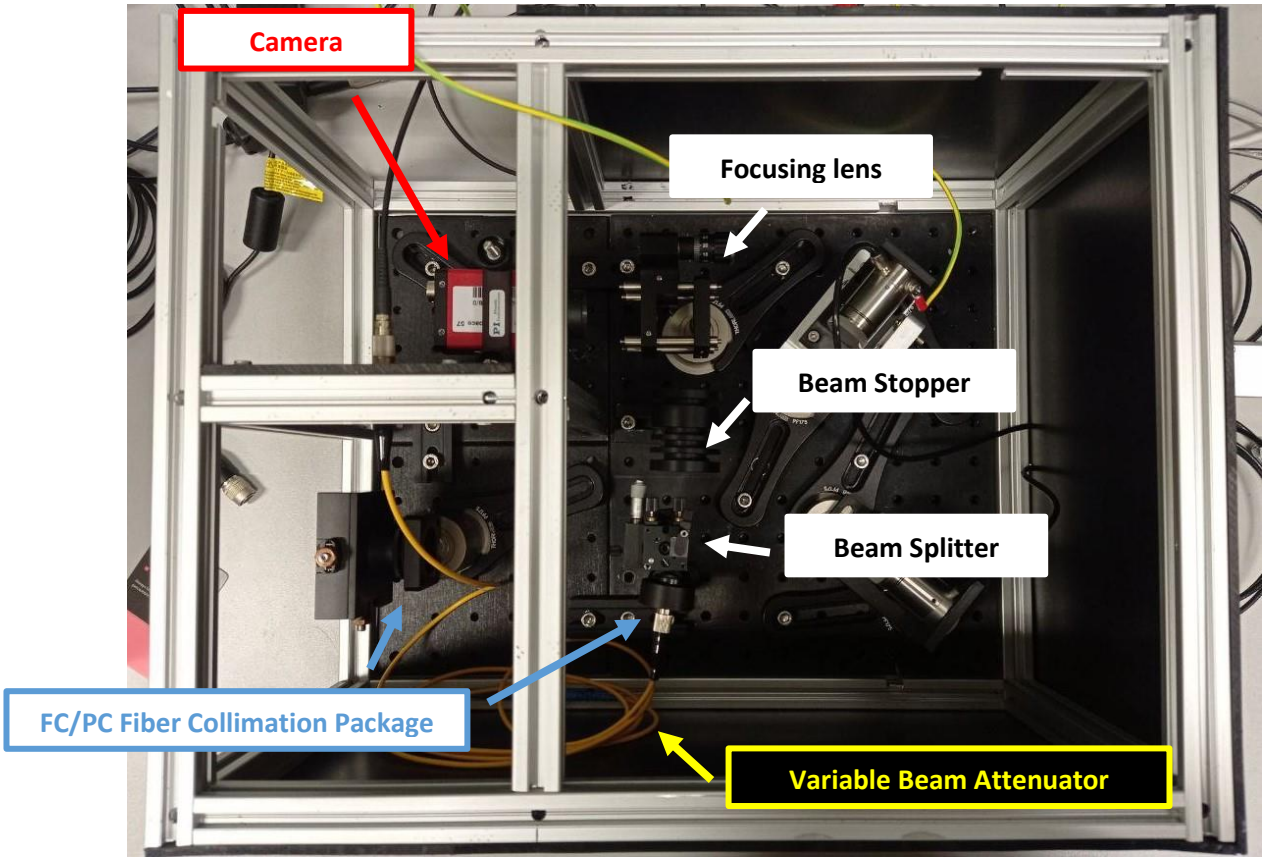

Figure 16. *Test setup-3.*

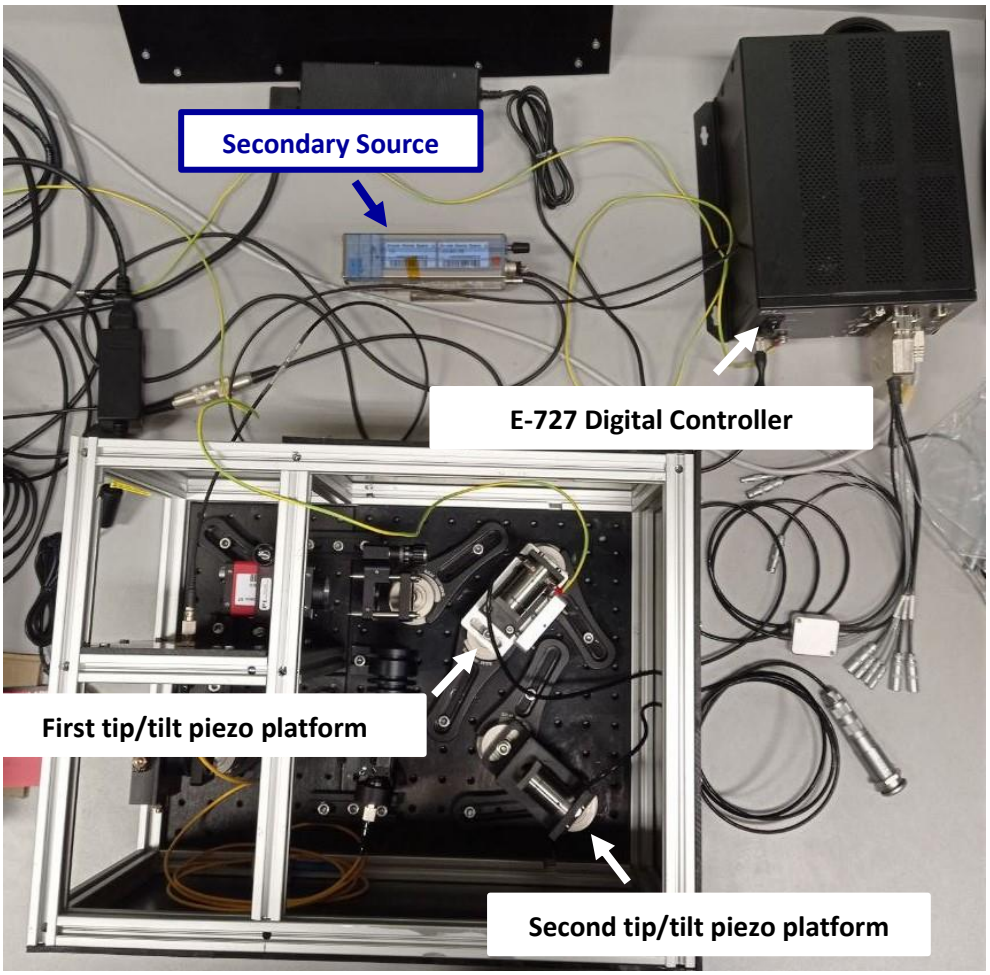

Figure 17. *Test setup-4.*

2.1.2 Software configuration

The design of the breadboard control and monitoring application was performed using the National Instruments LabVIEW software. LabVIEW is a graphical programming environment able to develop sophisticated control systems using icons and wires that resemble a flowchart. It offers integration with thousands of hardware devices and provides hundreds of built-in libraries for advanced control, analysis, and data visualization. Furthermore, in the case of CompactRIO, LabVIEW can access and integrate all the components of the LabVIEW reconfigurable I/O cRIO architecture.

The software version installed on the workstation of the Optics Lab is LabVIEW 2017. This is a collection of different products:

- the development environment (LabVIEW), which includes a variety of programming languages and hardware drivers for interfacing with I/O;
- the application software, that integrates tools to configure and control devices and test sequences;
- the add-ons modules, toolkits, and libraries that extend the capabilities of the programming environment or the application software.

The installed Embedded Control and Monitoring Software Suite include:

- LabVIEW Professional Development System;
- LabVIEW Real-Time Module, to create and debug deterministic applications running on target CompactRIO;
- LabVIEW FPGA Module;
- LabVIEW MathScript RT Module, which allows the integration of custom .m files into the LabVIEW graphical environment;
- LabVIEW Advanced Signal Processing Toolkit;
- Vision Acquisition Software.

The final breadboard control application was designed using mainly the embedded suites of the LabVIEW Professional Development System. Only the camera image acquisition process was implemented using the Vision Acquisition Software drivers. In the first phase, the target acquisition final algorithm (2.4) was developed in MATLAB and added to the control system using the LabVIEW MathScript RT Module. Then, to overcome the computing capabilities limitations, the detection software was rewritten in C language and integrated through the "Call Library Function Node", a Professional Development System tool allowing to directly call a DLL or a shared library function.

The LabVIEW Real-Time Module, based on the RIO Scan Interface technology, was used to program the real-time processor of the CompactRIO and access its I/O modules. In this mode, National Instruments provides a predefined personality for the FPGA (Field Programmable Gate Array) that periodically scans the I/O and places it in a memory map, making it available to LabVIEW Real-Time. Thus, the I/O variables can be instantly read and written scaled, and calibrated without any FPGA programming or compiling. The CompactRIO Scan Mode was suitable for the LISA application case as it allows single-point access to I/O at rates of a few hundred Hertz. It does not support streaming data at high frequencies.

2.2 Laser spot centroid computation

2.2.1 Introduction

The LISA constellation acquisition has very strict pointing and stability requirements. As the receiving satellite detects the transmitting laser on its CCD, the spot centroid shall be accurately determined. Then, the offset existing between the sending and the receiving spacecraft's reference position shall be evaluated and properly corrected by the attitude actuators.
To let the beam enter the FOV of the QPD detector, the centroid computation precision shall be ≤0.1 pixels. However, at the CAS surface, the source power is as weak as 100 pW, due to the inter-satellite long propagation distance. Furthermore, the scanning spot time visibility is short because of the beacon behavior of the laser intensity. Therefore, a high-precision, real-time method for centroid computation is essential for the success of LISA.

The traditional approach is one of the most efficient in the calculation of the laser spot center position. On a CCD detector, the centroid coordinates along the horizontal and vertical directions are

$$x_C = \frac{\sum_{i,j=1}^{n} x_i N_{i,j}}{\sum_{i,j=1}^{n} N_{i,j}} \qquad y_C = \frac{\sum_{i,j=1}^{n} y_i N_{i,j}}{\sum_{i,j=1}^{n} N_{i,j}}$$

where x_i and y_i denote the positions of the i_{th} pixel (*e.g.*, the column and the row indices respectively), N_i stands for the detected photo events, and n is the number of pixels involved in the calculation. In the traditional method, n is usually the total amount of pixels of the CCD detector.
As the algorithm is computationally simple, it can cope with the real-time requirements of LISA. However, this is sensitive to noise and usually has low precision, especially under weak light conditions.

Centroid accuracy is proportional to the Signal-to-Noise ratio: the detected photo events (N_i) contain both the photoelectrons inspired by the incident light and the noise electrons. In deep space, the number of photons is limited with respect to the noise sources (*e.g.*, read noise, background, Straylight, electronics). Furthermore, for the LISA application case, the transmitting laser power is weak and subject to modulation due to the dynamics of laser pointing.
To reduce the noise impact on the conventional method, the spot centroid estimate shall be performed on a smaller computational domain [7]. This kind of Region of Interest (ROI) must contain several photoelectrons and a few noise electrons, to properly increase the centroid precision. However, the number of pixels involved in the calculation needs to be carefully selected, so as not to sacrifice accuracy and achieve precision in the order of a tenth of a pixel or less.

The idea of executing the centroid computation on a small domain, containing as few pixels as possible around the spot real center, is the core concept of the suggested "improved method". It has the potential to address the high-precision positioning requirements under weak light conditions characterizing the LISA program.

2.2.2 Improved Centroid Computation Method

As described above, a smaller computational domain greatly reduces the number of perturbative pixels and increases the positioning precision. Based on the conventional method, the improved centroid computation process consists of three stages:

1. *Rough computational domain definition*
   To define a smaller computational area, the first step searches for the CCD pixel with the maximum gray value. Then, this brightest pixel turns into the center of a 5x5 pixels rough domain. The ROI size was chosen considering that the laser spot dimension on the real CAS is expected to be equal to about 3x3 pixels. The 5x5 value results from a trade-off between the need to minimize the number of noise pixels involved in the centroid calculation and correct errors in the brightest pixel computation, which are caused by the high noise levels and can lead to a shift of the rough domain.

2. *Beam centroid rough estimate*
   The traditional method defines the rough centroid of the identified computational domain.

3. *Beam centroid high-precision estimate*
   The first rough estimate of the spot centroid is rounded to the nearest integer point and then selected as a new center of a 5x5 pixels area. Finally, the traditional method is applied again, to achieve a high-precision centroid computation. The beam position estimate is performed twice as the offset existing between the domain center and the spot real centroid can become smaller the second time.

The feasibility of the improved method was validated under the LISA mission representative conditions (*e.g.*, detection of sub-picowatt beams and high noise levels) using MATLAB software. The tests performed to verify the algorithm compliance to the mission pointing requirements are described in the following paragraphs (2.4.6), contextually to the implemented strategies for noise mitigation and Signal-to-Noise ratio enhancement.

2.3 Edge Detection

2.3.1 Introduction

As explained in 1.2.1, the first part of the thesis activity was conducted ignoring the future introduction of the laser speckle. Thus, the issues leading to the selection of the spot identification preliminary algorithm were:

- the need for detection of weak and variable beams;
- the presence of secondary sources (*e.g.*, stars);
- the need for noise mitigation.

The most troubling topic was the need to differentiate the target spot from secondary sources. The stars visible in the FOV of the receiving satellite's CAS have the same appearance as the ideal point-spread function of an infinitely small point laser source. Their magnitude is fixed, and they can be of the same size and strength as the target beam. The transmitting source feature that makes it different from secondary sources is its variable intensity. The target laser is detectable just if the remote satellite's beam cone invests the receiving spacecraft. If this occurs, the CAS identifies a light spot whose power varies modularly according to the Gaussian distribution, due to the dynamics of laser pointing. If not, signal acquisition cannot be achieved. Furthermore, because in deep space the number of photons is limited, the detection is accomplished if the beam intensity is at least higher than the background noise average value.
The fundamental difference introduced by the transmitting satellite's scanning manoeuvre is the core concept of the target identification preliminary software. It works through the detection and characterization of all visible sources acquired by the receiving spacecraft's Constellation Acquisition Sensor. The classification stage involves the computation of each light spot centroid. For each pair of subsequent images, the algorithm compares the number of identified sources and their center estimates. If differences occur, the software recognizes that a light source has appeared/disappeared from the FOV of the spacecraft's sensor, just like a beacon does. In this case, this spot is identified as the target beam, and then, its centroid is saved and used for pointing purposes.

Another issue of the LISA constellation acquisition is the receiving satellite's scanning manoeuvre, which causes the spiral movement of the FOV of the detector. The final breadboard simulates the dynamics of the transmitting laser pointing by translating the platform's spiral orbit into an intensity law for the source. Thus, the target power being detected varies modularly at f_{source} = 1 Hz. Conversely, the first piezo tip/tilt platform mimics the movement of the receiving satellite's FOV (2.1.1). If both the FOV motion is fast enough and the image acquisition frequency is sufficiently small, the centroids of the same source are always different for each next pair of images. This can compromise the proper identification of the target. Because during the first part of the thesis activity the exact speed of the spacecraft's scanning manoeuvre was unknown, the worst-case was analyzed: the operating speed and the image sampling rate such as to cause the centroids of the same spot to be different in two subsequent frames.
To fix this critical issue, a position prediction algorithm joins the central core of the target identification process. It works through the computation of the centers

of the identified sources. Then, it processes the resulting values to determine the estimates of the spot centroids in the next sampled frame. These estimates result from the dynamics of laser pointing and the specifications of the receiving satellite's CAS. Finally, the algorithm compares the "predicted" centroids to the centers of the light sources detected in the new image.

The main topic in the development of the target acquisition preliminary process was the selection of a fast method able to identify multiple light sources. After careful consideration, a simple edge detection algorithm was chosen: its benefit is the ability to simplify the determination of the image pixels corresponding to the acquired spots and, thus, the centroid computation.

2.3.2 Canny Edge Detection-Step by Step

Edge detection is one of the most important processes in image analysis. Edges are significant changes in local intensity and are clues to separate regions within an object. Image edge information can also describe the outline of a generic target, its relative position within a selected area, and so on.
One of the most common edge detection algorithms was developed by Jhon F. Canny in 1986 and is still widely used due to its excellent performance.

The "Canny edge detector" is an operator that uses a multi-stage algorithm to detect a wide range of edges in images. The edge detection traditional procedures work by identifying the maximum value of the first derivative or zero crossing of the second derivative of an image. Although they have many advantages, such as simple computation, they are more sensitive to noise and their detection capability is inefficient for most applications. In 1986, Canny proposed a method to judge the performances of an edge detection operator [8]. This is based on the following three criteria:

- maximum of Signal-to-Noise ratio (good detection), *i.e.* the probabilities of failing to detect real edge points and falsely marking non-edged points should be low;
- good localization, *i.e.* the points that are marked by the operator as edge points should be as close as possible to the center of the true edge;
- one response to a single edge, *i.e.* there should be only one response output for a single edge, and the faint edges should be suppressed.

However, noise suppression and edge accurate location cannot meet the requirements simultaneously: while the edge detection operator smoothes the image to remove the noise, the uncertainty of the edge increases; in contrast, when the sensitivity of edge detection raises, the noise does. Canny operator executes a trade-off between noise cancellation and good localization and deduces an approximate implementation of the optimal edge detector.

The Canny edge detection algorithm is based on grayscale images and is composed of five steps [9]:

1. *Noise reduction*
   Noise mitigation is usually accomplished by Gaussian smoothing. Canny operator smoothes the original image with the first derivative of the 2-D Gaussian function, which is defined as

$$G_{x,y} = \frac{1}{2\pi\sigma^2} e^{-\frac{x^2+y^2}{2\sigma^2}}$$

where σ stands for the standard variance of $G_{x,y}$ and determines the width of the Gaussian filter and, thus, the outcome of smoothing.

The Gaussian filter removes noise but at the same time smooths the edges and other intensity discontinuities within the images, causing the loss of valuable information. The amount of blurring depends on the standard deviation and its value is a trade-off between noise removal and edge enhancement: small filters (*e.g.,* smaller σ) result in too many noise points, and large filters (*e.g.,* larger σ) tend to dislocate the edges.

2. *Gradient calculation*
   The second step consists of the computation of the magnitude and direction of the gradient of the smoothed image. The derivatives I_x and I_y *w.r.t* x and y can be calculated by convolving the image with Sobel kernels K_x and K_y, respectively

$$K_x = \begin{pmatrix} -1 & 0 & 1 \\ -2 & 0 & 2 \\ -1 & 0 & 1 \end{pmatrix} \quad K_y = \begin{pmatrix} 1 & 2 & 1 \\ 0 & 0 & 0 \\ -1 & -2 & -1 \end{pmatrix}$$

   Then, the following equations allow the estimate of the magnitude G and the slope θ of the gradient

$$|G| = \sqrt{I_x^2 + I_y^2}$$
$$\theta_{x,y} = \tan^{-1}\left(\frac{I_x}{I_y}\right)$$

3. *Non-maximum suppression*
   After deriving the magnitude of the gradient, the non-maximum suppression stage accurately positions the edges. This process guarantees that each edge is one-pixel width. Its functioning is simple: the algorithm uses a 3x3 neighboring area, which consists of eight edge directions, and goes through all the points on the intensity matrix to search for the pixels with the maximum gray value in each edge orientation. Thus, the brightest pixels are marked as candidate-edge points, while the others are recognized as non-edge points.

4. *Double Threshold*
   The Canny operator produces the final edges from the candidate-edge points with a double-threshold stage. This step aims at identifying three kinds of pixels:

   - strong pixels, whose intensity is so high that it's sure they contribute to the final edges;
   - weak pixels, which have an intensity value that is not high enough to be considered strong ones, but not small enough to be recognized as non-relevant for edge detection;
   - other pixels, which are considered non-relevant.

   The high threshold identifies the strong pixels (*e.g.*, intensity higher than the high threshold); the low threshold detects the non-relevant pixels (*e.g.*,

intensity lower than the low threshold). All pixels having intensity between both thresholds are flagged as weak, and the last step of the multi-stage algorithm allows to distinguish the strong pixels from the non-relevant ones.

4.1 Fix-Double Threshold method

The traditional Canny algorithm uses fixed double-threshold values. However, to avoid the loss of local edge information, high and low thresholds must change regularly. Thus, the conventional fix-threshold method lacks the capability of self-adaptation, and, in most cases, cannot satisfy the detection requirements.

To enhance Canny edge operator performances, an adaptive threshold selection method is needed [10]. The improved algorithm can fix the described issues, obtaining the threshold values automatically in the process of edge detection.

4.2 Adaptive-Double Threshold method

The proposed adaptive method is suitable for images with a large field of view, rich edge information, and scattered gradient magnitude distribution, in which the contrast of each part of the entire image is inconsistent, and the image gradient standard deviation is large enough. In this case, a fixed double-threshold for the whole image cannot accomplish edge detection: thus, the proper values must be selected for each pixel.

The improved algorithm works in the following way. Firstly, the mean of the gradient magnitude is calculated by

$$G_{avg} = \sum_{i=1}^{m} \sum_{j=1}^{n} \frac{|G_{i,j}|}{(m*n)}$$

where G_{avg} denotes the gradient magnitude average value, m and n are the number of pixels on the image width and height directions respectively, and $G_{i,j}$ stands for the image gradient magnitude.
Secondly, the process scans the whole image to detect the pixels whose gradient magnitude $G_{i,j}$ is smaller than 20% of the G_{avg}. These are marked as non-edge points directly. Then, the algorithm estimates the double-threshold for the remaining pixels starting from the mean of the gradient magnitude and the standard deviation of the elements in a 20×20 image gradient matrix, which is centered on each analyzed pixel. These parameters are calculated as follows

$$G_{avg,20} = \sum_{i=1}^{m} \sum_{j=1}^{n} \frac{|G_{i,j}|}{(m*n)}$$

$$\sigma_{20} = \left(\sum_{i=1}^{m} \sum_{j=1}^{n} \frac{|G_{i,j} - G_{avg,20}|^2}{(m*n)} \right)^{1/2}$$

where σ_{20} stands for the 20x20 image standard deviation, $G_{avg,20}$ is the 20x20 image gradient magnitude average value, and m and n are the number of pixels on the 20x20 image width and height directions respectively. Finally, the process estimates the threshold values of each pixel as

$$T_{h_{i,j}} = G_{avg,20} + k\,\sigma_{20}$$

$$T_{l_{i,j}} = \frac{T_{h_{i,j}}}{2}$$

where k is fixed to 1.2 and $T_{h_{i,j}}$, $T_{l_{i,j}}$ denote the high and low thresholds.

5. *Edge tracking by hysteresis*
   Based on the results of the double-threshold step, the hysteresis transforms the weak pixels (considered suspected edge points) into strong ones after analyzing their connectivity: if their adjacent pixels are edge pixels, then they are also recognized as edge pixels, otherwise, they are non-edge pixels.

2.3.3 Centroid Computation Method

After completing the edge detection step, the improved centroid computation method (2.2.2) is used. The Canny edge operator achieves the identification of the image pixels corresponding to the light sources. Then, for each detected area, the algorithm searches for the brightest pixel and derives the rough computational domain. Then, the calculation continues, and the process estimates the centroids of the identified sources. Finally, the introduced prediction algorithm processes the resulting values to determine the spot predicted centroids to be used for the comparison.

2.4 Target acquisition final algorithm

2.4.1 Introduction

During the second part of the thesis activity, some new issues led to a substantial modification of the described target detection process (2.3): the laser speckle and the exact speed of the receiving satellite's scanning manoeuvre.

The main topic was the removal of laser speckle. It is a random intensity distribution that forms when coherent light is reflected from a rough surface. This roughness may result from a phenomenon of optical surface contamination, as is the case for LISA. It has a peculiar granular appearance, which seems chaotic and unordered.
Speckle granularity is a major issue in the target identification process. Its pattern is quite like a random distribution of PSFs, three-dimensional diffraction patterns of light emitted from stars, or infinitely small point laser sources. These *"pseudo"* point-spread functions are analogous to secondary sources covering the whole satellite's detector, and whose size and intensity are completely random. Therefore, they can be strong and equally distributed enough to prevent the identification of the target beam.
The core concept of the suggested speckle removal strategy arises from its root mechanism. As explained in 1.2.1, the laser speckle is fixed on the satellite's CCD and does not change over time, as it arises from light reflection from a rough surface. Therefore, the easiest and fastest way to remove it consists of a difference operation between two subsequent frames. This action shall be performed first, so as not to affect the proper functioning of the target acquisition process.

The second issue is the spiral movement of the receiving satellite's FOV. The exact speed of the spacecraft's scanning manoeuvre is 1 $\mu rad/s$. This corresponds to about 0.6 $pixel/s$ on the CAS detector. Therefore, assuming an image acquisition frequency of 1 Hz, this scanning velocity implies that the difference between the centroids of the same source in two subsequent frames is less than 1 pixel. As a result, the position of the same light spot is nearly stationary in a next pair of images sampled at a proper distance. Thus, the analyzed worst-case (2.3) is quite far from the real configuration of the LISA mission. This caused a substantial modification of the identification preliminary algorithm (2.3).

The need for laser speckle removal causes the introduction of a difference operation between two subsequent frames. Assuming an image acquisition frequency of 1 Hz, due to the spiral orbit of the platform and the specifications of the satellite's CAS, the difference results in the cancellation of both the laser speckle and the secondary sources. This happens because their intensity is fixed. Conversely, as explained in 2.3.1, the power of the target source varies modularly at f_{source} = 1 Hz. Therefore, if the transmitting laser beam invests the receiving satellite, the difference cannot remove it from the image obtained by subtracting two subsequent frames sampled by the CAS at 1 Hz. The target acquisition is still possible by detecting its change in intensity.

If stars are cancelled, the Canny edge detection process of identification of multiple light sources is not needed. Therefore, the discussed solution (2.3) is not suitable for the LISA application case. Although the removal of secondary sources is a benefit for the constellation acquisition, the difference operation causes a significant reduction in the beam power, which is initially below 100 pW. Furthermore, the laser speckle induces a notable increase in shot noise, whose strength is directly related to the root square of signal power. Indeed, the speckle random pattern causes an augmentation of the average intensity, resulting in enhanced shot noise levels.
Due to the dual effect of the beam power reduction and noise augmentation, the target acquisition final process needs effective noise mitigation and Signal-to-Noise ratio enhancement techniques.

As a result, the identification software was developed in four steps:

1. *Ensemble averaging filtering method & Speckle removal*
2. *Gaussian smoothing filtering method*
3. *Background Thresholding*
4. *Centroid Computation*

2.4.2 Ensemble averaging filtering method & Speckle removal

As explained in 1.2.1, one of the main issues in the LISA constellation acquisition is the ability to detect a sub-picowatt laser beam embedded in a strong noisy environment. The major obstacle is the shot noise, whose intensity is further increased by the laser speckle.

Shot noise is a perturbation due to the corpuscular nature of transport. Current flow is not continuous, but results from the motion of charged particles (*e.g.*, electrons and/or holes) which are discrete and independent. Assuming to "observe" the carriers passing a point in a conductor for some time interval, it would find that a "few" more or less vectors would pass in a one-time gap versus the next. It is impossible to predict the motion of individual electrons, but it is possible to calculate the average net velocity of an ensemble of electrons, or the average number of electrons drifting past a particular point per time interval. The variation about the mean value or average of these quantities is the shot noise. Since particle events are random and independent, the continuous flow of these discrete pulses gives rise to almost white noise, which can be described by a Poisson statistic.
Shot noise may be dominant when the finite number of energy carriers is sufficiently small so that uncertainties due to the Poisson distribution are significant. The magnitude of shot noise increases according to the root square of the expected number of events, such as the electric current or intensity of light. The more signal, the smaller the fraction coming from shot noise. Thus, it is frequent with small currents or low light intensities.

The most effective way to reduce the shot noise without compromising the target information is the so-called ensemble averaging filtering method [11], whose core concept is noise cancellation. The shot noise has random nature, and its average value at different time instants is zero. Ensemble averaging is based on

the collection of signals over the same time or frequency domain: therefore, successive sets of acquired data are summed point by point. Sampling the signal and averaging the samples result in the cancellation of the noise component, due to its random nature.

Let n be the number of measurements to sum to obtain the ensemble average. The signal S_i adds for each repetition. The total signal S_n is given by

$$S_n = \sum_{i=1}^{n} S_i = nS_i$$

For noise, the variance is additive. Thus, the Total Variance is

$$\sigma_n^2 = \sum_{i=1}^{n} \sigma_i^2 = n\sigma_i^2$$

The estimate of the standard deviation or the total RMS (Root Mean Square) noise is

$$\sigma_n = \sqrt{n}\, \sigma_i$$

As the power of random variables equals the mean-squared value, the following equation is introduced

$$\sigma_n = \sqrt{n}\, N_i$$

where N_i denotes the power of random noise.
An estimate of the Signal-to-Noise ratio (SNR) is given by

$$SNR \approx \frac{S}{N}$$

that is the Signal-to-Noise power ratio. Thus, the SNR after n repetitions can be determined as

$$\left(\frac{S}{N}\right)_n = \frac{nS_i}{\sqrt{n}\, N_i} = \sqrt{n} \left(\frac{S}{N}\right)_i$$

This result implies that the ensemble averaging filtering method can improve the Signal-to-Noise ratio in proportion to the root square of the number of repetitions of the signal: as it increases, the SNR grows too, and noise mitigation is achieved.

Due to the need for noise reduction, the ensemble averaging filtering method consists of the first step of the target detection process. Thus, the final algorithm does not perform the speckle removal difference operation between two subsequent "single" images, but between the frames resulting from averaging two succeeding sets of images. The number of collected frames and the CAS acquisition frequency was selected to prevent the averaging from compromising the beam shape and intensity. As the laser strength changes modularly at f_{source} = 1 Hz and the shift caused by the receiving satellite's scanning manoeuvre equals 0.6 $pixel/s$, the detection software makes the difference between the averages of two sets of 9 frames sampled at f_{acq} = 10 Hz. Therefore, the ensemble averaging works on images acquired within 1 s, that is the time interval for which the beam position and intensity are almost fixed. As a result, the first step of the target detection software fulfills the following goals:

- reduction of the shot noise standard deviation to $1/3$ of its original value;
- removal of both laser speckle and secondary sources;

- preserving of target detection information.

2.4.3 Gaussian smoothing filtering method

After ensemble averaging filtering and speckle removal, noise mitigation is accomplished but the difference operation has drastically reduced the intensity of the laser source. Therefore, the second step of the target detection software consists of an effective Signal-to-Noise ratio enhancement technique. The selected and optimized method is the Gaussian smoothing filtering [12].

Smoothing is a process that averages each data point with its neighbors in a series or image. Its basic function is simple: this scans point by point the collected data and replaces each measure with a new value that is some function of both the original point and the surrounding ones. Two-dimensional smoothing consists of convolution: in image analysis, it transforms an image by applying a kernel over each pixel and its local neighbors. The kernel is a matrix whose size and values determine the transformation effect of the convolution. The whole process involves these steps:

- the central pixel of the kernel matrix is placed over each pixel of the image matrix. Then, the algorithm multiplies each of the pixels of the kernel by the corresponding image pixel it is over;
- the procedure sums the derived estimates, and the result is recognized as the new value of the pixel of the image matrix the kernel central pixel is over;
- these actions are repeated across the entire image.

There are different methods of 2-D smoothing, but, for the LISA application case, filtering with a Gaussian kernel is significant.
The smoothing kernel defines the shape of the function that is used to take the average of the neighboring points. Thus, a Gaussian kernel has the shaping of a normal distribution curve. In the classic statistical way, the standard deviation σ defines the width of the Gaussian. However, when the Gaussian kernel is used for smoothing, it is common to describe its width with another related measure: the Full Width at Half Maximum ($FWHM$). The $FWHM$ is the width of the Gaussian shape at half of its maximum height and can be calculated with the following formulae

$$FWHM = 2\sqrt{2\ln 2}\,\sigma$$

As explained in 2.3.2, the width of the Gaussian kernel determines the outcome of smoothing, affecting the spread of the kernel weights.

Smoothing can increase the Signal-to-Noise ratio according to the matched filter theorem [13-14]. Matched filtering is a widely used signal processing technique in target detection. This filter consists of a linear operator with a transfer function that maximizes the output Signal-to-Noise ratio for an input wavelet with known properties. This goal is accomplished by cross-correlating the contaminated signal with the pure wavelet.
Two-dimensional matched filters are common in image processing because of their effectiveness against additive stochastic noise. To maximize the SNR, this theorem states that the optimum filter is the one matched to the “object” being

identified. In the case of smoothing, the filter is a Gaussian kernel. Therefore, if the target signal has a Gaussian shape and its $FWHM$ is known, then it will best be detected after smoothing the image with a Gaussian filter of the same $FWHM$. The ideal point-spread function of the target beam has a Gaussian shape (1.1.2). Therefore, smoothing the images with a Gaussian kernel that is matched to the light spot being detected maximizes its output Signal-to-Noise ratio.

The second step of the target acquisition software smoothes the image resulting from the speckle removal difference operation with a 5x5 pixels Gaussian kernel. The general equation for a Gaussian filter of size $(2k+1)$x$(2k+1)$ is given by

$$K_{i,j} = \frac{1}{2\pi\sigma^2} e^{-\frac{(i-(k+1))^2 + (j-(k+1))^2}{2\sigma^2}} \quad ; \quad 1 \leq i,j \leq (2k+1)$$

where i and j are the pixel indices on kernel width and height directions respectively, and σ stands for the standard deviation of the Gaussian in pixel unit. The optimal width σ of the smoothing kernel was estimated starting from the characteristics of the real target point-spread function, ensuring that the simulations conform to the context of LISA. The table below shows the real and simulated Gaussian shape parameters.

	FWHM	*Standard deviation*
Real PSF parameters [µrad]	*3.64*	*1.55*
Simulated PSF parameters [pixels]	*1.26*	*0.54*

Table 12. *Real and estimated target point-spread function parameters.*

The Gaussian smoothing filtering step fulfills the following objectives:

- significant increase in the output Signal-to-Noise ratio;
- further noise mitigation.

The tests concerning the effectiveness of Gaussian smoothing are described in 2.4.6. At this stage, great attention was paid to the effects of convolution on the target beam shape and intensity, to properly assess the risk of loss of valuable detection information.

2.4.4 Background Thresholding

The main goal of the second step of the identification software is the maximization of the target beam output Signal-to-Noise ratio. Assuming the transmitting laser cone is investing the receiving satellite, the laser spot to be detected is visible in the image acquired by the receiving spacecraft's CAS. Theoretically, after smoothing filtering, if the beam intensity differential is sufficiently strong, the centroid computation method (2.2.2) can directly estimate the target position. If not, the direct evaluation of the smoothed image's brightest pixel leads to an erroneous assessment of the laser spot centroid. This results as, after both ensemble averaging and smoothing filtering, noise is not completely suppressed, but just reduced.

So as not to compromise the proper function of the improved centroid computation, the third step of the detection software consists of a background threshold. It aims at scanning the smoothed image to identify two kinds of pixels:

- strong pixels, whose intensity is higher than the background threshold and which are recognized as part of the target beam. Thus, their brightness value remains unchanged;
- non-relevant pixels, whose strength is lower than the background threshold and which are considered *"noise"* pixels. Therefore, the algorithm sets their intensity value to null.

The background threshold was selected by testing, starting from the analysis of the brightness of noise pixels remaining after Gaussian filtering. This study was conducted applying the first two steps of the target detection software on images containing just noise sources (*e.g.*, laser speckle and related shot noise). One of the main disadvantages of thresholding is the loss of the beam shape and intensity information. Due to the low power of the detection objective, the need for noise cancellation can lead to the suppression of the whole target or its external pixels, whose intensity level is significantly small. In the last case, the laser information is compromised, and this affects the precision of the centroid estimate. Paragraph 2.4.6 contains the analysis of the effects of background threshold on the accuracy of the beam position computation.

The third step of the detection algorithm fulfills the following objectives:

- noise suppression;
- detection of the laser beam (if present with sufficient power). Identification of the laser spot pixels to be used for centroid computation.

2.4.5 Centroid Computation

The selected centroid computation process is the described improved method (2.2.2). After background thresholding, the algorithm scans the whole image to search for the brightest pixel. If the intensity of all pixels in the scanned image is null, the brightest pixel value is set to $(0,0)$ and the centroid computation stops. If not, the process defines the 5x5 pixels computational domain that is centered on the estimated brightest pixel. Then, the centroid calculation is performed twice according to the improved algorithm.

After estimating the beam position, the target identification is achieved. Then, the pointing stage of the LISA constellation acquisition processes the beam centroid to derive the satellite position offset that the attitude actuators shall correct to accomplish the centering of the transmitting laser on the FOV of the QPD detector.

2.4.6 Performance analysis

The last section of the second chapter examines the performance of the detection software. This analysis allowed the identification of the pros and cons of each step, leading to effective optimization of the acquisition algorithm control parameters. All tests were executed in MATLAB. The strategies used to emulate the LISA mission representative conditions are:

- introduction of *"synthetic"* images of laser speckle. This study analyzed two random intensity normalized patterns, to assess the effectiveness of the

detection on different noise spreads. The selected images are in 8-bit grayscale (*e.g.*, *GLS-8*);

- introduction of 8-bit grayscale images of a 3x3 pixels laser spot. To represent the source modularity and validate the detection of different signal powers, the beam image magnitude was scaled with respect to the noise power.

1. *Noise mitigation*

The goal of the first analysis was the assessment of the effectiveness of the ensemble averaging filtering on noise mitigation. This objective was accomplished by estimating the shot noise standard deviation of the images resulting from:

- the difference operation between two frames collected at f_{acq} = 1 Hz. This case is called "*No Averaging*";
- the difference operation between the images obtained by averaging two sets of *9* frames sampled at f_{acq} = 10 Hz. This case is the *"Averaging"* one.

Filtering is successful if the standard deviation in the "*Averaging case"* is reduced to $1/3$ of its initial estimate. As shot noise is random, the standard deviation was derived numerous times for both cases. Then, the resulting values were averaged to perform the comparison. The analyzed images did not contain the target laser spot, so as not to alter the results of noise mitigation.

The shot noise standard deviation was estimated as follows

$$\sigma = \sqrt{\frac{\sum_{i=1}^{m}\sum_{j=1}^{n}\left(I_{i,j} - I_{avg}\right)^2}{(m*n-1)}}$$

$$I_{avg} = \frac{\sum_{i=1}^{m}\sum_{j=1}^{n} I_{i,j}}{(m*n)}$$

where σ stands for the standard deviation, $I_{i,j}$ is the image magnitude, I_{avg} is the image magnitude average value, and m and n are the numbers of pixels in the image width and height directions respectively.

The following formula allowed the evaluation of the so-called Standard Deviation ratio

$$\sigma_{ratio} = \frac{\sigma_{No\ Averaging\ case}}{\sigma_{Averaging\ case}}$$

where σ denotes the standard deviation average value.

This first test analyzed two different laser speckle patterns, to accurately assess the performance of the ensemble averaging filtering. **Table 13** summarizes their characteristics.

	First Speckle pattern	*Second Speckle pattern*
Standard Deviation [GLS-8]	*2.9393*	*1.8182*
Average Intensity Value [GLS-8]	*3.1964*	*1.3697*

Table 13. *Laser Speckle patterns parameters.*

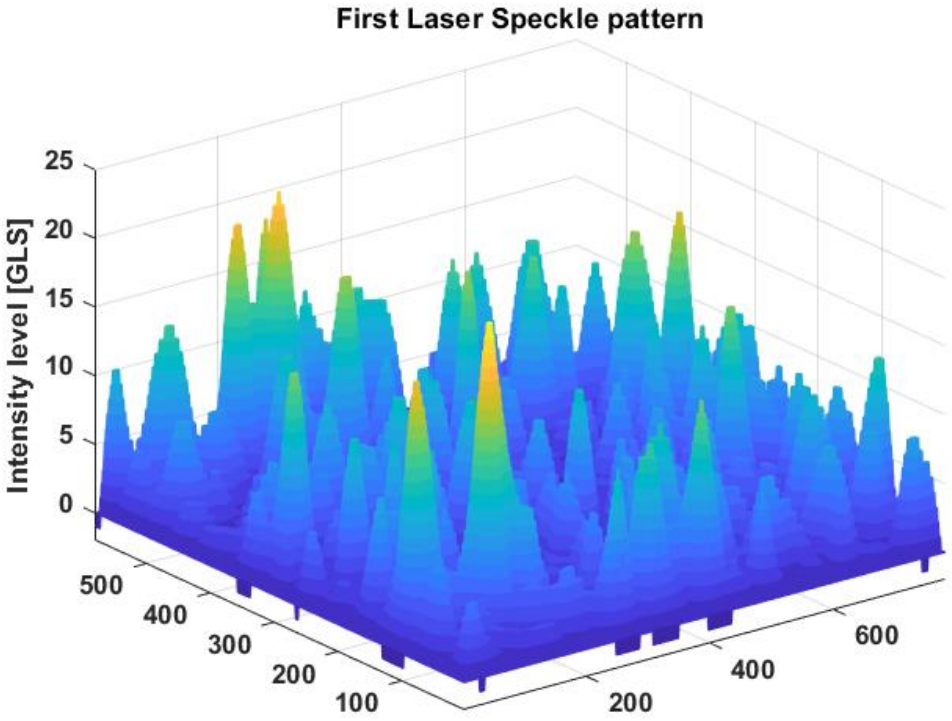

***Figure 18**. First Speckle pattern-Relative intensity level.*

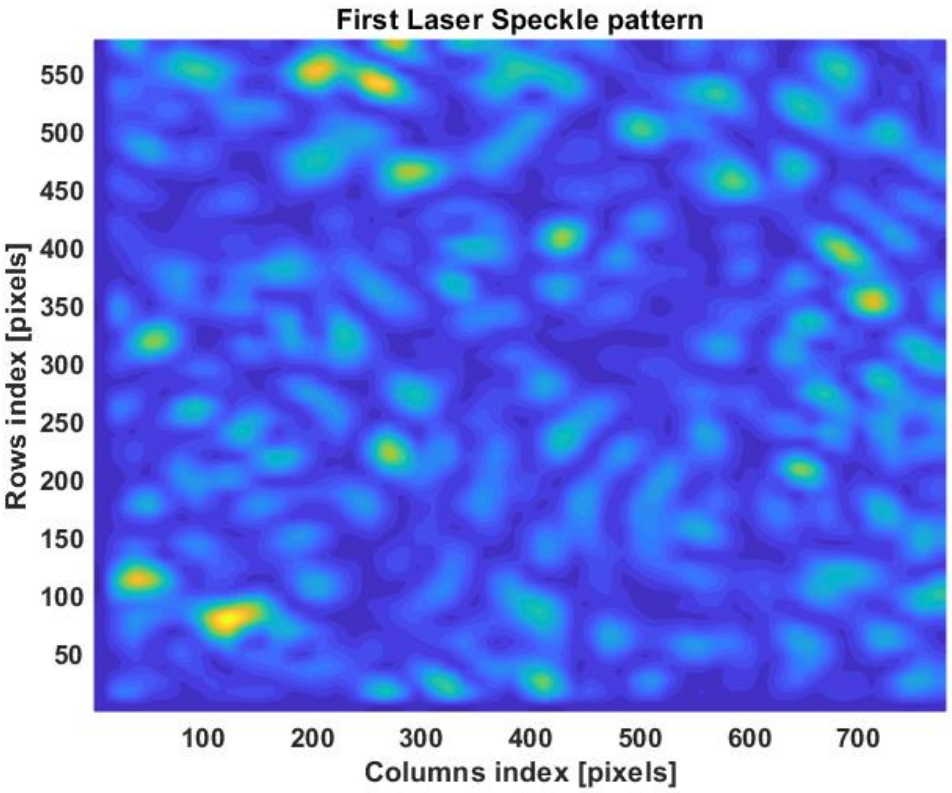

***Figure 19.** First Speckle pattern-Image matrix.*

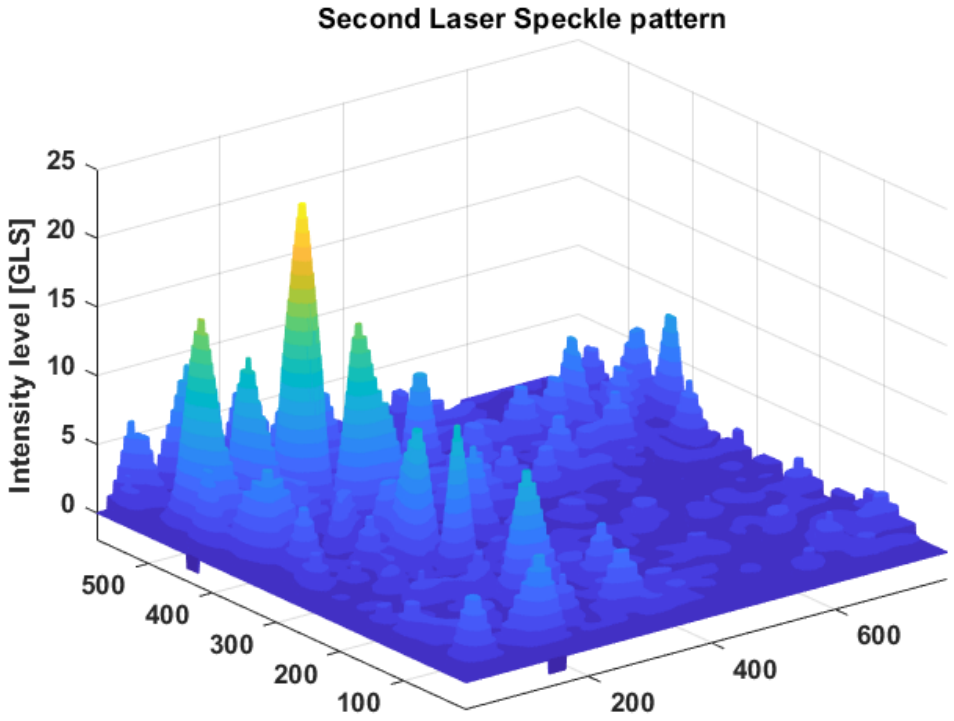

Figure 20. *Second Speckle pattern-Relative intensity level.*

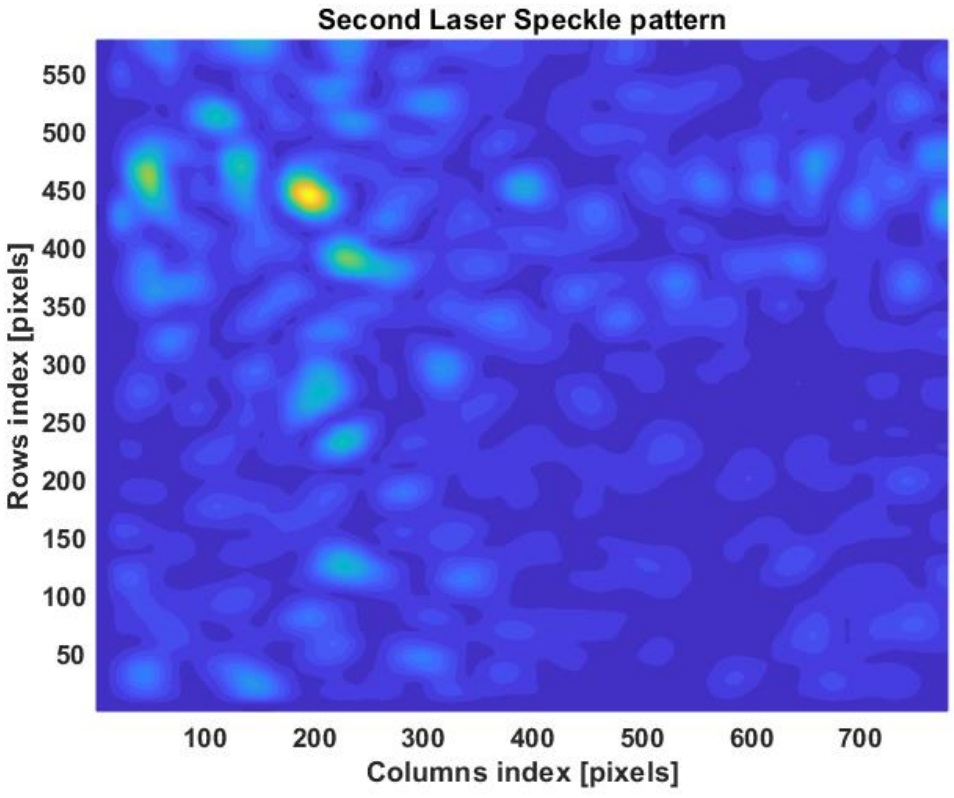

Figure 21. *Second Speckle pattern-Image matrix.*

The first laser speckle pattern has both standard deviation and average intensity value greater than the second one. As shot noise is related to the root square of signal power, the shapes of both the shot noise spreads are expected to be like those of patterns that originated them and then, different from each other.
Table 14 shows the results of the first test.

		First Speckle pattern	*Second Speckle pattern*
Shot noise Standard Deviation [GLS-8]	***No Averaging case***	*2.5562*	*1.6875*
	Averaging case	*0.8539*	*0.5624*
Standard Deviation ratio		***2.9935***	***3.0004***

Table 14. *Ensemble averaging filtering test results.*

As explained previously, for the "*No Averaging case"* the estimates of the shot noise standard deviations are quite like those of their respective speckle patterns. The ensemble averaging filtering significantly reduced the standard deviation average values, as shown from the results of the "*Averaging case"*. In conclusion, the Standard Deviation ratio is equal to 3 for both noise patterns.

Thus, the shot noise standard deviations of the "*Averaging case"* are equal to $1/3$ of their estimates in the "*No Averaging case"*. Therefore, ensemble averaging filtering is effective in noise mitigation of different noise patterns.

2. *Signal-to-Noise ratio enhancement*

The main goal of the analysis performed on both the ensemble averaging and the Gaussian smoothing was the assessment of their effectiveness in Signal-to-Noise ratio enhancement. This objective was accomplished by evaluating the achieved SNR after each filtering operation.

The formula below gives an estimate of the Signal-to-Noise ratio

$$SNR \approx \frac{S}{N} = \frac{S}{\sigma}$$

where S and N stand for signal and noise average power respectively. The second equivalence exists as the power of a random variable equals its mean-squared value, that is its standard deviation σ.

As for the noise mitigation analysis, this test analyzed both the described representative speckle patterns (view **Table 13**). To emulate the LISA mission representative conditions, the image of a 3x3 pixels laser spot was added to the speckle synthetic frames. **Figure 22** shows the ideal point-spread function of the simulated beam. To assess the filtering effects on different signal powers, the intensity of the light source was scaled with respect to the speckle pattern standard deviation σ.

For both the considered speckles, this test studied five relative intensity levels. The power levels that are shown in **Table 15** are the most significant as they emulate the most critical condition of the LISA constellation acquisition: the need for the detection of a sub-picowatt beam embedded in a strong

noisy environment. The analyzed levels correspond to the lowest powers of the intensity curve for the source able to mimic the dynamics of the laser pointing of the satellite being identified.

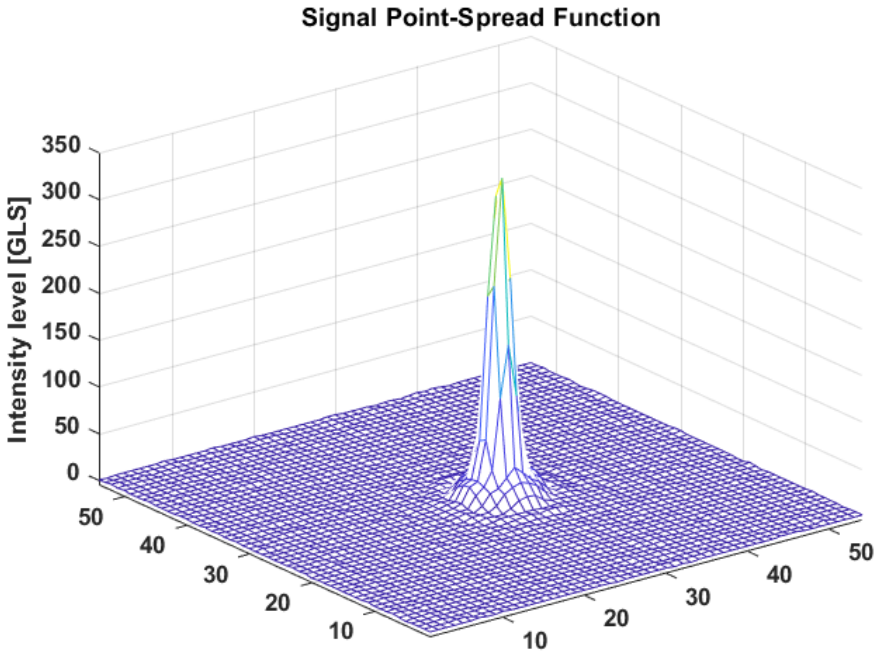

Figure 22. *Source beam ideal point-spread function.*

		First Speckle pattern ***σ = 2.9393 [GLS-8]***	*Second Speckle pattern* ***σ = 1.6875 [GLS-8]***
Signal Average Intensity Level [GLS-8]	**5σ**	*4.8280*	*2.9865*
	4σ	*3.8624*	*2.3892*
	3σ	*2.8968*	*1.7919*
	2σ	*1.9312*	*1.1946*
	1σ	*0.9656*	*0.5973*

Table 15. *Signal relative intensity levels.*

For each average intensity level, the performance analysis estimated the following parameters:

- ✓ the starting Signal-to-Noise ratio SNR_0 before filtering operations. This is equal to

$$SNR_0 = \frac{I_{avg}}{\sigma_0}$$

where I_{avg} is the beam average magnitude and σ_0 stands for the noise initial standard deviation;

- ✓ the Signal-to-Noise ratio SNR_{avg} after ensemble averaging filtering. It is evaluated by

$$SNR_{avg} = \frac{I_{avg}}{\sigma_{avg}}$$

where I_{avg} is the beam average magnitude (that is unchanged after applying the first filter) and σ_{avg} denotes the standard deviation of the mitigated noise pattern;

- ✓ the Signal-to-Noise ratio $SNR_{smoothing}$ after Gaussian smoothing. It is given by

$$SNR_{smoothing} = \frac{I_{avg,smoothing}}{\sigma_{smoothing}}$$

where $I_{avg,smoothing}$ denotes the average magnitude of the smoothed signal and $\sigma_{smoothing}$ is the standard deviation of the smoothed noise pattern.

The formulae used to derive both the signal average magnitude I and the noise standard deviation are the same introduced in the noise mitigation test. As done for the previously described analysis, all the listed parameters were estimated numerous times for both noise patterns and each relative intensity level. Then, the resulting values were averaged and discussed to assess the achievements of the filtering operations.

Table 16 shows the test results.

		First Speckle pattern ***σ = 2.9393 [GLS-8]***			*Second Speckle pattern* ***σ = 1.6875 [GLS-8]***		
		SNR_0	SNR_{avg}	$SNR_{smoothing}$	SNR_0	SNR_{avg}	$SNR_{smoothing}$
Signal Average Intensity Level [GLS-8]	**5σ**	*1.6426*	*5.6540*	*16.3721*	*1.6426*	*5.2927*	*15.2339*
	4σ	*1.3141*	*4.5280*	*12.9425*	*1.3141*	*4.2450*	*12.2263*
	3σ	*0.9855*	*3.3959*	*9.6069*	*0.9855*	*3.1831*	*9.1632*
	2σ	*0.6570*	*2.2608*	*6.5015*	*0.6570*	*2.1271*	*6.3488*
	1σ	*0.3285*	*1.1274*	*3.7123*	*0.3285*	*1.0575*	*2.9743*

Table 16. *Gaussian smoothing filtering - SNR test results.*

To estimate the contribution of the ensemble averaging and the Gaussian smoothing to the Signal-to-Noise ratio enhancement, for each relative intensity level the following parameters were derived

$$K_{avg} = \frac{SNR_{avg}}{SNR_0}$$

$$K_{smoothing} = \frac{SNR_{smoothing}}{SNR_{avg}}$$

$$K_{global} = K_{smoothing} * K_{avg}$$

where K is a factor that measures the effectiveness of both filtering methods on the SNR.

Table 17 shows the obtained estimates. For both random noise patterns, the ensemble averaging filtering causes an increase in the Signal-to-Noise ratio of about 3 times if compared to its original value. This finding is consistent with paragraph 2.4.2: the slightest differences with the theoretical rate results as the SNR is estimated with an approximate relation. Furthermore, after Gaussian smoothing, the SNR grows about 3 times its previous estimate.

Finally, both the filtering operations make the Signal-to-Noise ratio approximately *9* times greater than its starting measure.

		First Speckle pattern σ = 2.9393 [GLS-8]			*Second Speckle pattern* σ = 1.6875 [GLS-8]		
		K_{avg}	$K_{smoothing}$	K_{global}	K_{avg}	$K_{smoothing}$	K_{global}
Signal Average Intensity Level [GLS-8]	5σ	*3.4422*	*2.8957*	*9.9745*	*3.2260*	*2.9260*	*9.4566*
	4σ	*3.4519*	*2.8583*	*9.8493*	*3.2286*	*2.8563*	*9.6135*
	3σ	*3.4457*	*2.8408*	*9.7539*	*3.2295*	*2.9432*	*9.4719*
	2σ	*3.4409*	*2.8854*	*9.8941*	*3.2398*	*2.9070*	*9.7094*
	1σ	*3.4317*	*2.9161*	*9.9549*	*3.2212*	*2.9617*	*9.6902*

Table 17. *Effectiveness parameters - Computation results.*

Therefore, both the ensemble averaging filtering and the Gaussian smoothing are effective in the Signal-to-Noise ratio enhancement of different signal powers embedded in strong noise patterns.

3. *Signal average intensity level detection threshold*

As shown in **Table 17**, the filtering actions implemented by the target acquisition software can boost the Signal-to-Noise ratio at least *9* times its initial estimate. However, the increase of the laser strength with respect to the shot noise average power cannot ensure the proper identification of the target beam.

Both the ensemble averaging filtering and the Gaussian smoothing induce significant noise mitigation. However, after filtering, some shot noise peaks may still be present. The main issue arises as the intensity of these peaks can be higher than the signal. If the remaining shot noise is not completely suppressed, the direct use of the improved centroid computation method and the search for the brightest pixel can lead to the erroneous assessment of a “noise” pixel as a target one. In this case, the wrong estimate of the beam position would cause the receiving satellite to perform a pointing manoeuvre that could move him away from the remote spacecraft.
Thus, before centroid computation, the background thresholding step of the acquisition software ensures the shot noise cancellation. However, due to the low power of the laser beam, this can lead to the suppression of the whole target and prevent the final algorithm from identifying signals below a certain intensity level.

One of the main objectives of the performance analysis was the identification of the signal average intensity level detection threshold. This consists of the minimum power level the background thresholding cannot suppress. This goal was accomplished by applying the target acquisition software to the images obtained by adding the synthetic speckle patterns to the 3x3 pixels laser spot. The intensity of the source was properly scaled with respect to the noise power and the previously identified signal average intensity levels (view **Table 15**) were analyzed.

The parameters affecting the limits of the final algorithm are:

- the width of the Gaussian filter that determines the outcome of smoothing;
- the background threshold.

As fully explained in 2.4.3, the matched concept states that the filter optimum width that maximizes the SNR is the one matched to the detection "object". Thus, the Gaussian kernel standard deviation is fixed (view **Table 12**): this value cannot change to impact the amount of blurring, as it affects the Signal-to-Noise ratio enhancement.

The background threshold is a kind of fixed parameter too. Its estimate arises from the analysis of the brightness of noise pixels remaining after Gaussian smoothing. It was selected by testing for both the considered laser speckle patterns and was set to T_{bkg} *= 5 GLS-8*.

Due to the random nature of noise, the detection threshold analysis was repeated numerous times, to properly assess the performance of the final algorithm. The test results show how the signal minimum average intensity level the acquisition process can identify is $\mathbf{3}\boldsymbol{\sigma}$, where σ is the standard deviation of the starting noise pattern.

4. *Centroid accuracy estimate*

The last analysis evaluates the risk of loss of detection information introduced by both smoothing and background thresholding. Even if the Gaussian kernel is of matched $FWHM$ to the laser beam, the convolution process causes minimal changes in the signal magnitude distribution. Furthermore, if the beam power is significantly small, the background thresholding can lead to the suppression of the whole spot or its external pixels. In both cases, the target shape and intensity are compromised, and this affects the precision of the centroid estimate.

The objective of the first test was the assessment of the effects of Gaussian smoothing on the accuracy of the beam position computation. This goal was accomplished by applying the acquisition software up to Gaussian filtering to the images obtained by adding the synthetic speckle patterns to the 3x3 pixels laser spot and then, by estimating the beam centroid with the improved method. As for the previous analysis, the calculation was executed numerous times and, obviously, only on the signal average intensity levels the final algorithm can identify. The resulting estimates were averaged and compared with the target real centroid, to verify the achievement of the desired accuracy.

To satisfy the LISA pointing specifications, the precision of the laser spot centroid computation shall be ≤0.1 pixels (2.2.1). The position accuracy $\overline{\Delta x_c}$ is given by

$$\overline{\Delta x_c} = \left|\bar{x}_{c,real} - \bar{x}_c\right|$$

where $\bar{x}_{c,real}$ is a vector of two coordinates representing the real centroid and $\bar{x}_c$ denotes the target estimated position.

The following table summarizes the test results.

		CENTROID ACCURACY ESTIMATE-Gaussian smoothing			
		First Speckle pattern σ = 2.9393 [GLS-8]		*Second Speckle pattern* σ = 1.6875 [GLS-8]	
		Centroid estimate [pixels]	***Accuracy [pixels]***	***Centroid estimate [pixels]***	***Accuracy pixels]***
Signal Average Intensity Level [GLS]	5σ	*(205.86,206.09)*	*(0.02,0.08)*	*(205.87,206.08)*	*(0.01,0.09)*
	4σ	*(205.83,206.08)*	*(0.05,0.09)*	*(205.82,206.09)*	*(0.06,0.08)*
	3σ	*(205.88,206.11)*	*(0.00,0.06)*	*(205.86,206.09)*	*(0.02,0.08)*
		Real centroid [pixels]: *(205.88,206.17)*			

Table 18*. Centroid accuracy test results-Gaussian smoothing.*

As shown in **Table 18**, the Gaussian smoothing does not prevent the satisfaction of LISA strict pointing requirements. However, the resulting estimates suggest that the convolution process causes some minimal changes in the target magnitude distribution. The filtering cannot change the signal average intensity level as the applied kernel is normalized with respect to the sum of its elements. However, the shot noise corrupts the image magnitude, and mainly the laser spot external pixels, whose intensity is significantly small. Thus, the dual effect of both the noisy environment and the Gaussian smoothing produces the loss of valuable detection information and affects the centroid accuracy, especially for the y coordinate.

Once analyzed the impact of Gaussian filtering, another analysis was executed to assess the effects of the background thresholding. This goal was accomplished by applying the whole target identification software to the same images of the previous test.

		CENTROID ACCURACY ESTIMATE-Background thresholding			
		First Speckle pattern σ = 2.9393 [GLS-8]		*Second Speckle pattern* σ = 1.6875 [GLS-8]	
		Centroid estimate [pixels]	***Accuracy [pixels]***	***Centroid estimate [pixels]***	***Accuracy pixels]***
Signal Average Intensity Level [GLS-8]	5σ	*(205.99,206.47)*	*(0.11,0.30)*	*(206.00,206.48)*	*(0.12,0.31)*
	4σ	*(206.02,206.49)*	*(0.14,0.32)*	*(206.00,206.41)*	*(0.12,0.24)*
	3σ	*(206.00,206.48)*	*(0.12,0.31)*	*(206.00,206.49)*	*(0.12,0.32)*
		Real centroid [pixels]: *(205.88,206.17)*			

Table 19*. Centroid accuracy test results-Background Thresholding.*

As shown in **Table 19**, the centroid computation cannot satisfy LISA strict pointing requirements after background thresholding. The need for shot noise cancellation causes a significant worsening of the performance of the improved method: as the beam power is significantly reduced by the long propagation distance, the threshold step induces the suppression of the target spot less intense pixels. This results in the cancellation of their contribution to the centroid computation. However, despite the loss of valuable detection information, the background thresholding ensures the proper operation of the constellation acquisition in case the transmitting

laser cone is not investing the receiving satellite. As explained in 2.4.4, the background threshold was selected by testing to guarantee the suppression of the shot noise peaks remaining after Gaussian smoothing. In case of no signal, the image resulting from this step is a null matrix. Thus, as the improved method estimates its brightest pixel, the output value equals $(0,0)$. This causes the stop of the centroid computation, avoiding the erroneous assessment of a "noise" pixel as a target one. Therefore, the background thresholding cannot be removed from the target detection software.

To satisfy the accuracy requirements and achieve the proper centering of the laser beam on the FOV of the QPD detector, the simplest way is to apply the improved centroid computation method to the images resulting from the Gaussian filtering step. As shown in **Table 18**, the smoothing effect causes minimal changes in the beam shape and intensity distribution. This result arises from the core concept of the matched filter: to maximize the output Signal-to-Noise ratio, the applied kernel shall be of the same size and shape as the target beam. Under these conditions, the convolution process can point out the laser signal and suppress noise, without altering and deleting the spot information.

In conclusion, to guarantee the satisfaction of the LISA mission strict pointing requirements, the target detection software shall be updated as follows:

- after Gaussian smoothing, the background thresholding step is executed to guarantee the proper function of the constellation acquisition process;
- then, the algorithm searches for the brightest pixel of the image resulting from background thresholding;
- then, if the estimated brightest pixel equals $(0,0)$, the centroid computation is not performed. If not, the improved method is applied to the image that emerged from the Gaussian smoothing step to derive the beam position.

3. Experiments & Results

The third chapter describes the implementation and validation of the LISA constellation acquisition breadboard.

The test system control application was developed using LabVIEW software. The LabVIEW programs are called Virtual Instruments (VI). The VIs contain three main components: the front panel, the block diagram, and the icon with the box of the connectors.
The front panel is the VI user interface, and includes two types of interactive terminals:

- *controls*, such as potentiometers, buttons, and dials. They simulate the instrument input devices and provide data to the block diagram of the VI;
- *indicators*, such as graphics, LEDs, and other displays. They emulate the output device tools and display the data that the block diagram captures or generates.

The block diagram contains the graphic format of the source code, which consists of the graphical representation of the functions able to control the terminals on the front panel. The block diagram includes subVIs, functions, constants, structures, and links that transfer data among other terminals and other objects of the block diagram.

A subVI corresponds to a subroutine in textual programming languages. To use a VI within another VI (*e.g.*, a subVI), the icon with the box of the connectors must be created. Each VI displays an icon, which is a kind of graphic representation that identifies a subVI in the block diagram of the main VI. The box of the connectors is a collection of terminals that correspond to the controls and indicators of a VI, similarly to the list of parameters of a function in textual programming languages. Thus, this defines the inputs and outputs to be connected to the VI to use it as a subVI.

The final control application consists of the main VI containing several subVIs, which group the block functions able to control specific devices or simulate different stages of the LISA constellation acquisition. This organization allows the user to easily monitor the proper operation of the test system and identify any causes of failure. It results as the development of the breadboard control application was a step-by-step process, in which the functions capable of emulating the different acquisition phases were gradually introduced.

The basic architecture of the main VI is organized in three segments:

- *Initialization*, a section able to initialize the hardware, read the configuration information files, or set the flags and control parameters default value;
- *Main application*, which consists of at least one cycle (*e.g.*, a loop) that comes repeated until the user decides to exit the program, or the program stops for other reasons such as the completion of an I/O or the satisfaction of the cycle exit conditions;
- *Closure*, a section usually dealing with closing the files and hardware connections, writing the configuration information on disk, or restoring the I/O on the default state and post-processing the results of the experimental test.

The final breadboard control application was developed starting from a basic VI which was used to validate a pre-existing focal plane simulator. Its structure is shown in **Figure 23**.

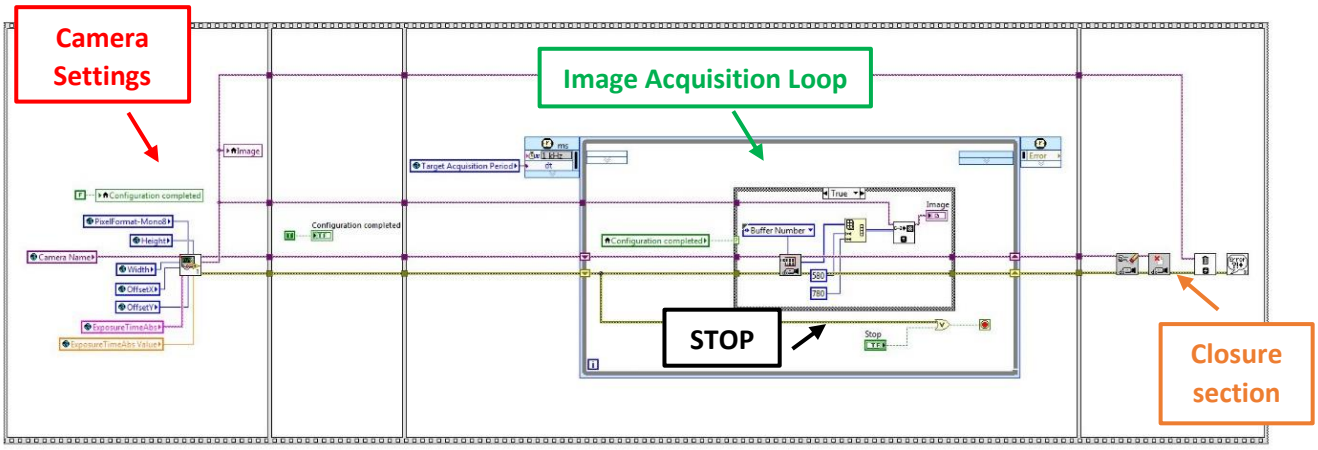

Figure 23. *Basic test breadboard control application.*

The initial main VI contains the block functions able to control the camera image acquisition process. The initialization section includes the "Camera Settings" subVI, which is used for opening the connection, initializing the installed hardware, and configuring the acquisition. The user can modify the controls on the front panel to set the camera operating parameters. The following table shows the hardware default settings.

Camera settings configuration	
Pixel Format	Mono 8
Height [pixels]	580
Width [pixels]	780
Offset X-Axis [pixels]	0
Offset Y-Axis [pixels]	0
Exposure time [µs]	4000

Table 20. *Camera configuration settings.*

The "Height" and "Width" variables allow the user to select a proper Region of Interest (ROI) from the whole resolution of the camera. Furthermore, this ROI can be moved with respect to the origin of the CCD reference system (located in the left top corner) using the "Offset X-Axis" and "Offset Y-Axis" parameters.

The main application section consists of a Timed Loop (called "Image Acquisition"), containing the functions that control the camera acquisition process and display the sampled images through the front panel. The source code of the core segment is contained in a LabView Conditional Case Structure, which is controlled by the "Configuration Completed" boolean indicator. This logic flag activates if the configuration of the hardware settings completes. If not, the image acquisition process cannot start. The Timed Loop end condition consists of the user acting on the STOP button on the front panel or the occurrence of a failure. Finally, the closure stage shuts down the connection with the selected camera.

A LABVIEW Flat Sequence Structure contains and separates all phases of the breadboard control application. Each section is enclosed in a flat structure frame: thus, they execute sequentially.

The basic control application was changed to properly control the final breadboard (2.1.1) able to simulate the LISA constellation acquisition. Each segment of the source code was updated as follows:

- *Initialization section*
  The basic initialization stage was modified with the introduction of:
  - the "Variables Initialization" subVI, which sets the default values of the boolean flags and the control parameters. Furthermore, this reads and configures the hardware command files (*e.g.*, the CompactRIO and piezo tip/tilt platform command files);
  - the "Piezo Connection, ATZ & SERVO ON" subVI, which initializes the piezo tip/tilt platforms.

  The "Camera Settings" subVI configuring the image acquisition process was unchanged.

- *Main application section*
  The final main application segment includes:
  - the "Piezo Command" Timed Loop, which controls the first piezo tip/tilt platform, emulating the spiral movement of the receiving spacecraft's FOV and the laser spot centering stage of the constellation acquisition process;
  - the "Laser Modulation Command" Timed Loop, which commands the NI 9269 module of the CompactRIO, to simulate the dynamics of the laser pointing of the sending satellite;
  - the "Target Acquisition" Timed Loop, which adds to the source code the identification algorithm able to detect the laser beam. The "Image Acquisition" Timed Loop was included in the "Target Acquisition" loop.

- *Closure section*
  The closure section of the breadboard control application contains:
  - the block functions which close the camera acquisition process;
  - the "Piezo Disconnection & SERVO OFF" subVI, which disconnects the link to the piezo tip/tilt platform;
  - the command which restores the default value of the AO variable that is connected to the 9269 module of the cRIO;
  - the "Image Saving" subVI, which performs post-processing operations on the acquired target images.

The step-by-step process leading to the development of a LabVIEW source code able to control the final breadboard and validate the simulation of the LISA constellation acquisition was long and difficult. The validation of the final setup is proved in this chapter through the characterization of 5 Experimental Tests:

- *Experimental Test 1*, which validated the simulation of the dynamics of the laser pointing of the sending and the receiving satellites;

- *Experimental Test 2*, which was used to assess the proper integration of the target identification final algorithm in the system control application;
- *Experimental Test 3*, which validated the simulation of the pointing stage of the LISA constellation acquisition process;
- *Experimental Test 4*, which demonstrated the effectiveness of the target acquisition software against the laser speckle;
- *Experimental Test 5*, which proved the effectiveness of the identification software against the secondary sources. It represented the final implementation of the constellation acquisition in LISA mission representative conditions.

These tests are characterized through the description of the setup, the main objectives, and the developed algorithms. Furthermore, a detailed description of the test results is provided to demonstrate the breadboard capability to simulate the LISA constellation acquisition from the optical point of view.

3.1 Experimental Test 1

3.1.1 Test setup

The setup of the first experimental test is the described final breadboard (2.1.1). However, in this phase, all the devices able to simulate the presence of a secondary source in the FOV of the receiving spacecraft were disabled.

3.1.2 Test objectives

The test objectives are summarized as follows:

1. to simulate the dynamics of the laser pointing of the sending satellite by translating the spiral orbit of the platform into an intensity law for the source;
2. to simulate the dynamics of the laser pointing of the receiving satellite by translating the spiral orbit of the platform into a displacement law for the first piezo tip/tilt platform. This results in the mimicking of the movement of the field of view of the spacecraft;
3. to properly control the first piezo tip/tilt platform;
4. to properly command the Electronics Variable Attenuator (EVO) by the NI 9269 module of the CompactRIO;
5. to monitor the state of the system.

3.1.3 Test algorithms

- *Test objective 1.*

  To simulate the dynamics of the laser pointing of the sending satellite, the modulation of the power source was added to the breadboard basic control application. The intensity law able to mimic the spiral orbit of the spacecraft's platform was derived by the *Guidance, Navigation & Control Department*, and provided in form of experimental data. The power of the laser source varies modularly at f_{source} = 1 Hz and the shape of the peak profile is of Gaussian type.

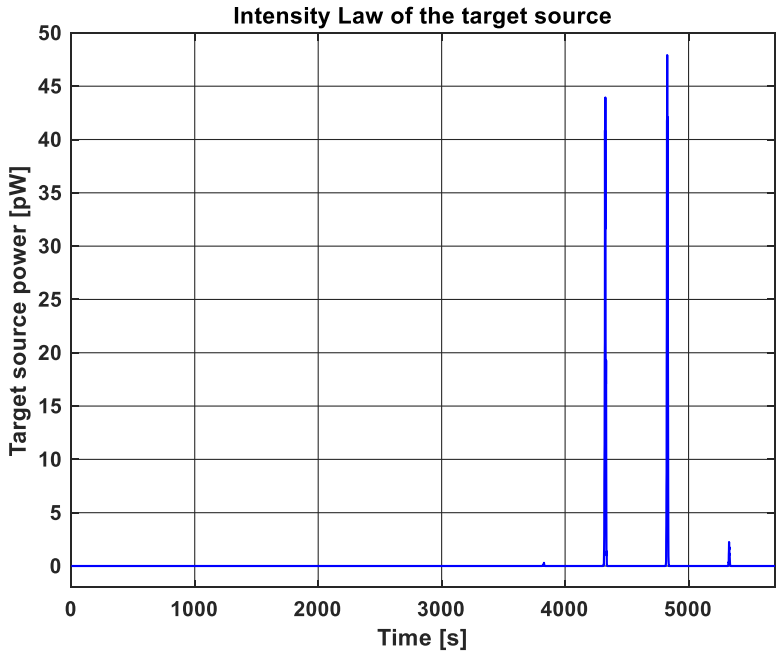

Figure 24. *Intensity law of the target source.*

The whole scanning manoeuvre lasts T_{scan} = 5700 s. However, the period during which the transmitting laser cone is investing the receiving spacecraft is reduced to $t_{detectable}$ = 32 s. Furthermore, the power curve outlines two peaks, which can both be detected by the target acquisition software.

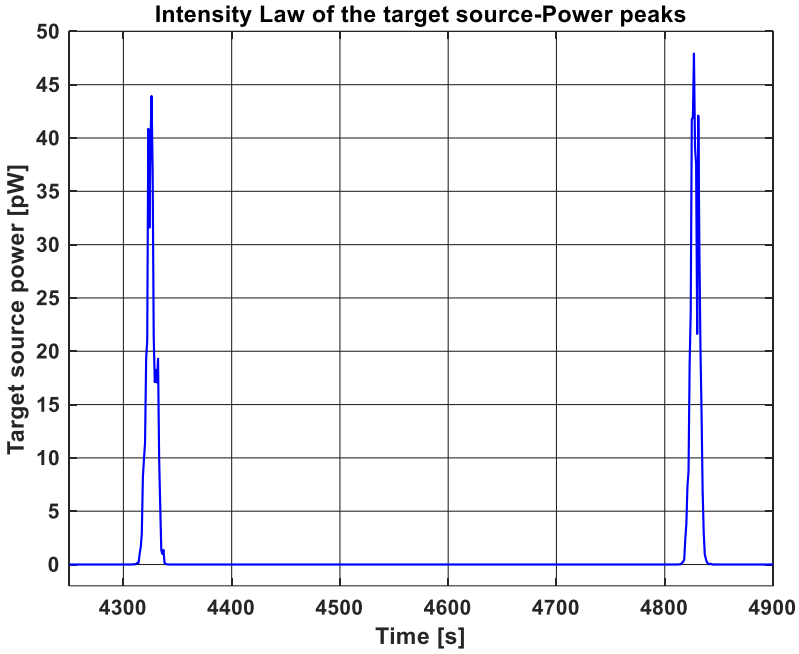

Figure 25. *Intensity law of the target source-Power peaks.*

Starting from the experimental data, the modulating signal to apply to the primary laser source through the Electronics Variable Attenuator was derived.

The selected device allows two analog methods for attenuation control:

- to rotate the manual power adjustment knob on the front panel. This offers the full range of attenuation: rotating the knob clockwise increases the output power, while rotating it counterclockwise causes the output power to reduce;
- to apply a voltage to the SMA (*e.g.*, Sub-Miniature A version) modulation input on the EVO side utility panel.

The second technique allows the command of the Electronics Variable Attenuator without the need for manual intervention: thus, this was preferred to the first one. The power source is attenuated through the EVO SMA modulation input by applying a voltage up to 4.9 V. To use the full attenuation range, the manual control knob is fully rotated clockwise to the maximum power setting. As the EVO internal variable optical attenuator is biased at almost 0 V at minimum attenuation, the following steps were needed to derive the modulating signal:

- normalization of the provided intensity law for the power source with respect to its maximum;
- mirroring of the normalized curve with respect to the time axis;

- multiplication of the resulting values by the maximum applicable voltage (*e.g.*, 4.9 V);
- translation of the multiplied curve to achieve a minimum voltage equal to 0 V.

The following figure shows the modulating signal applied to mimic the dynamics of the laser pointing of the sending satellite.

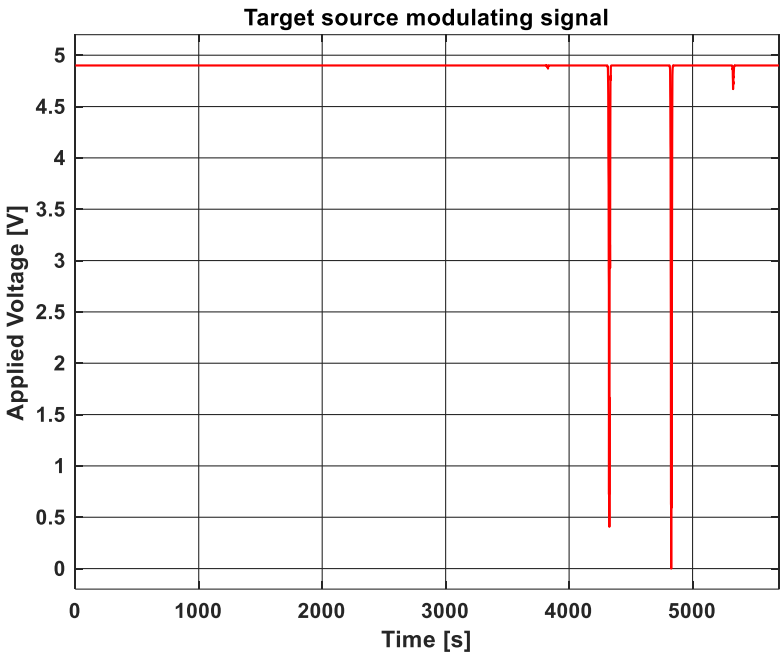

Figure 26. *Modulating signal of the target source.*

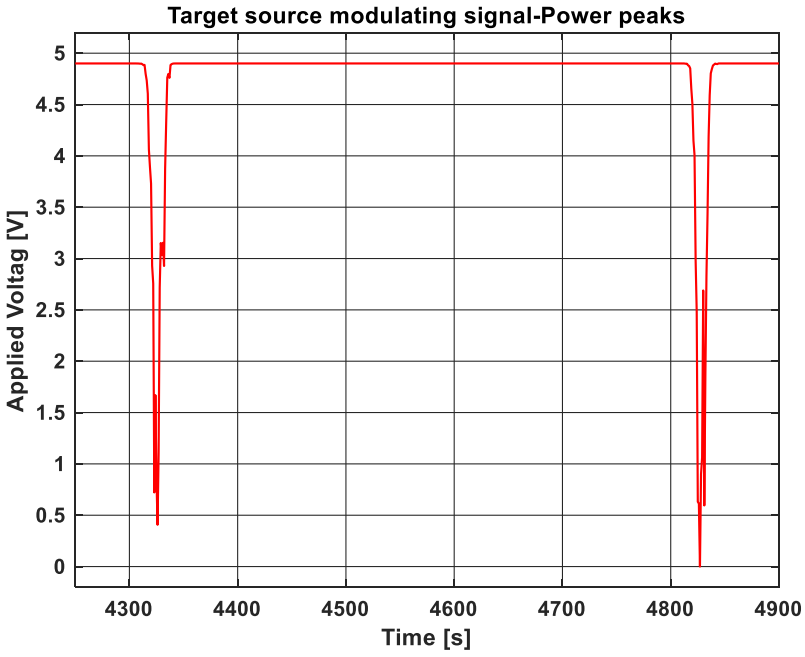

Figure 27*. Modulating signal of the target source-Power peaks.*

To control the modulation of the signal power within the final breadboard, the resulting voltages were saved in a text file. In the initialization section of

the control VI, the "Variables Initialization" subVI was introduced. It contains the LabVIEW block functions that convert the modulating commands to a 1-D array, named "Laser Modulation Command", which contains the voltages to send to the Electronics Variable Attenuator. Then, the "Laser Modulation Command" Timed Loop was added to the main application segment. During the simulation, this cycle scans the command vector at the same frequency the variation of the laser intensity occurs (*e.g.*, f_{source} = 1 Hz). As the CompactRIO platform electronically controls the EVO, each modulating voltage is applied to the attenuator by sending the proper command to the NI 9269 module to which the device is connected. The implementation of the spiral orbit of the sending satellite stops if one of the following events occurs:

- the user enables the STOP button by acting on the front panel;
- the command file to be scanned is ended.

The closure stage of the system control application contains a command restoring the default value of the AO variable which connects to the NI 9269 module of the CompactRIO.

- *Test objective 2.*

To simulate the dynamics of the laser pointing of the receiving satellite, the breadboard basic control application was modified by introducing the functions able to control the first piezo tip/tilt platform.
The spiral law able to mimic the FOV movement of the receiving spacecraft was supplied by the *Guidance, Navigation & Control Department*, and provided in form of experimental data. The resulting displacements are measured in μrad and represent the target position to command the piezo tip/tilt actuators. As not to exceed the platform's tit/tilt range (*e.g.*, 2 $mrad$), the control values were centered on the platform axes's mid-range positions, *e.g.* (1000,1000) μrad.

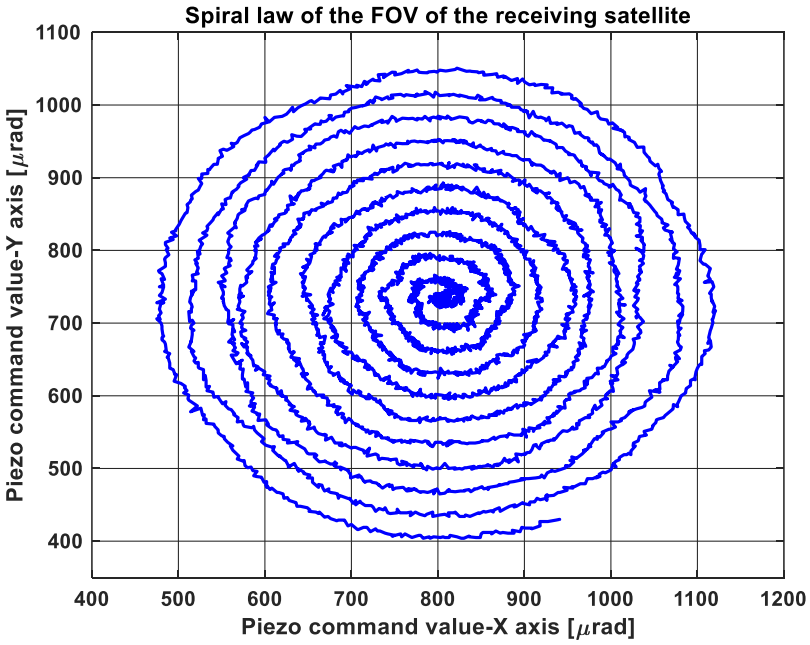

***Figure 28**. Spiral law of the FOV of the receiving spacecraft.*

As done for the modulation control of the primary laser source, the angles able to emulate the spiral orbit of the satellite's platform were saved in a text file. In the initialization section of the control application, this is converted to a 2-D array, called "Spiral Command", from the "Variable Initialization" subVI. Furthermore, the "Piezo Command" Timed Loop was introduced in the main application section. The command file of the piezo tip/tilt platform can mimic the speed of the satellite's scanning manoeuvre (*e.g.*, 1 $\mu rad/s$) and is constructed to be scanned at $f_{piezo\ command}$ = 1 Hz. Thus, every second the proper platform axes position is selected and sent to the E-727 digital controller of the piezo actuators to mimic the dynamics of laser pointing.

To ensure the proper command of the piezo platform, the breadboard control application was modified as follows:

1. *Initialization section*
   This section guarantees the correct initialization of the selected hardware. The platform is controlled by the "E-727 Digital Multi-Channel Controller", which is interfaced to the workstation through a connection hub. The first executed operation is the establishment of an Ethernet link between the main computer and the digital controller. When stable communication is achieved, the control VI transmits a series of command strings to the driver of the piezo tip/tilt platform, to execute the following actions:

   - Automatic Zero Point adjustment, a procedure that sets the output voltage which is to be applied at the zero position of the platform axes. Once this command is accomplished, a boolean indicator (*e.g.*, the so-called "ATZ Completed") activates;
   - Servo On, a command that fixes the servo-control state of the platform axes to closed-loop operation. If the correct servo-state is achieved, the "SERVO ON" flag is enabled.

   As the Servo On operation is performed, a "Configuration Completed" indicator activates. This flag states if the piezo tip/tilt platform initialization is accomplished: when its value is TRUE, the core section of the system control application can start. As the sending and the receiving satellites' scanning manoeuvres are simultaneous, the "Configuration Completed" indicator allows the implementation of both the "Laser Modulation Command" and the "Piezo Command" loops. Therefore, the block functions of both the Timed Loops are contained within a LabVIEW Conditional Case structure controlled by the described flag. Furthermore, the latter sets the beginning of the image acquisition process of the camera, which provides visual feedback about the dynamics of the laser pointing. The "Image Acquisition Loop" was unchanged *w.r.t.* the basic VI.

2. *Main application section*
   As the setting configuration is achieved, the "Configuration Completed" flag activates and the "Laser Modulation Command", the

"Piezo Command" and the "Image Acquisition" loops can start. At this stage, the piezo command matrix is scanned at $f_{piezo\ command}$ = 1 Hz. Each selected pair of angles (θ_x, θ_y) is sent to the digital controller and represents the target position to be reached by the piezo actuators. The E-727 driver converts these angles to proper voltage commands. Then, the closed-loop operation mode ensures that the actual piezo position is on the target. To assess the proper implementation of the spiral orbit, the current axes position of the piezo tip/tilt platform is verified by sending the command string <POS?> to the E-727 digital controller.

The "Piezo Command" Timed Loop of the breadboard control application stops if one of the following events occur:

- the user enables the STOP button;
- the command file to be scanned is ended.

These conditions cause the arrest of all the block functions of the main segment (*e.g.*, both the "Image Acquisition" and the "Laser Modulation Command" loops).

3. *Closure section*
   When both the "Laser Modulation Command", the "Piezo Command", and the "Image Acquisition" loops stop, the closure section of the system control application can start. The E-727 digital controller receives the following series of command strings:

   - Servo Off, a procedure that sets the servo-control state of the platform axes to open-loop mode. Then, the "SERVO ON" flag is disabled;
   - Closure of the Ethernet connection.

   Before interrupting the communication with the driver of the piezo tip/tilt platform, the control VI sends the command string <ERR?> to the E-727. This gets the error code of the last occurred error, which is then reset to its default 0 value. If some errors arise, a *"Controller Error"* flag activates. Thus, the main VI recovers the error code to be used to analyze the causes of the occurred failure.

Figure 29 shows a sketch of the breadboard control application of the Experimental Test 1.

- *Test objective 3.*
  To properly command the piezo tip/tilt platform the following operations are performed:

  - the "ATZ Completed" flag provides feedback about the correct implementation of the Automatic Zero Point adjustment procedure;
  - the "SERVO ON" indicator allows the user to monitor the servo state of the axes of the platform;

- the “Configuration Completed” flag states the successful closing of the piezo platform’s settings configuration. Furthermore, this commands the switch to the core section of the control application;
- the <POS?> string is sent to the E-727 digital controller to get the current position of the platform’s axes and provides the user with feedback about the implementation of the derived angles of the piezo mirror;
- the “Controller Error” flag informs the user that a failure occurs to the E-727 digital controller.

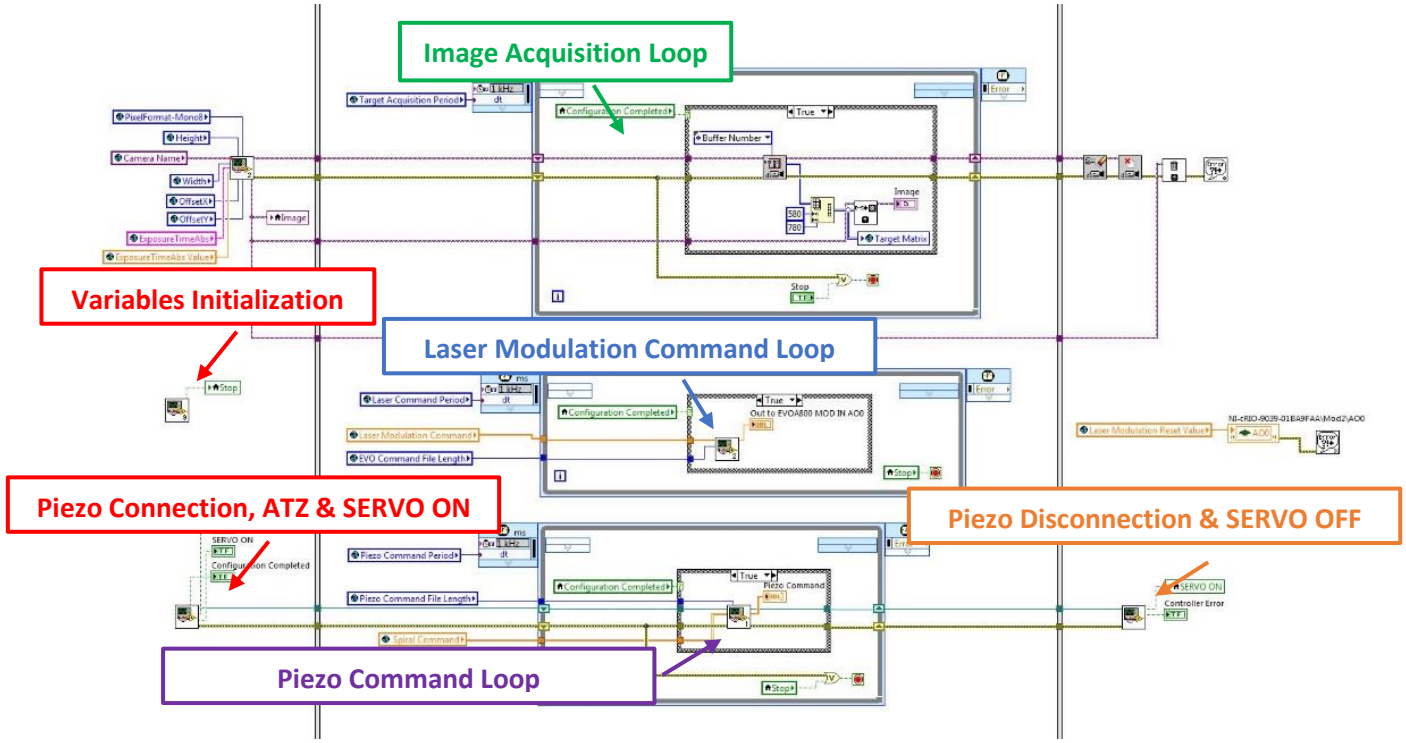

Figure 29. *Control Application of the Experimental Test 1.*

- *Test objective 4.*
  To assess if the Electronics Variable Attenuator is correctly controlled by the NI 9269 module of the CompactRIO, the following actions are implemented:
  - the reading from the Power Meter allows to monitor the trend of the attenuation of the laser source power;
  - the NI 9222 module of the CompactRIO is linked to the second SMA connector of the EVO. It consists of output for power monitoring: thus, this validates the correct implementation of the derived modulating voltages.
- *Test objective 5.*
  The introduced visual feedback to properly monitor the state of the system are:
  - a STOP button, which allows the user to suppress the experimental test if an obvious failure occurs;

- the “Controller Error” flag, which informs the user that an error happens in the E-727 digital controller;
- the LabVIEW “General Error Handler VI”, which connects to the block functions that control the piezo tip/tilt platform. If an error occurs, this VI returns a description of the failure and displays a dialog box on the front panel;
- the LabVIEW “General Error Handler VI”, which connects to the block functions that command the camera image acquisition process;
- the LabVIEW “General Error Handler VI”, which connects to the AO variable of the NI 9269 module of the CompactRIO that guarantees the proper attenuation of the power source.

3.1.4 Test results

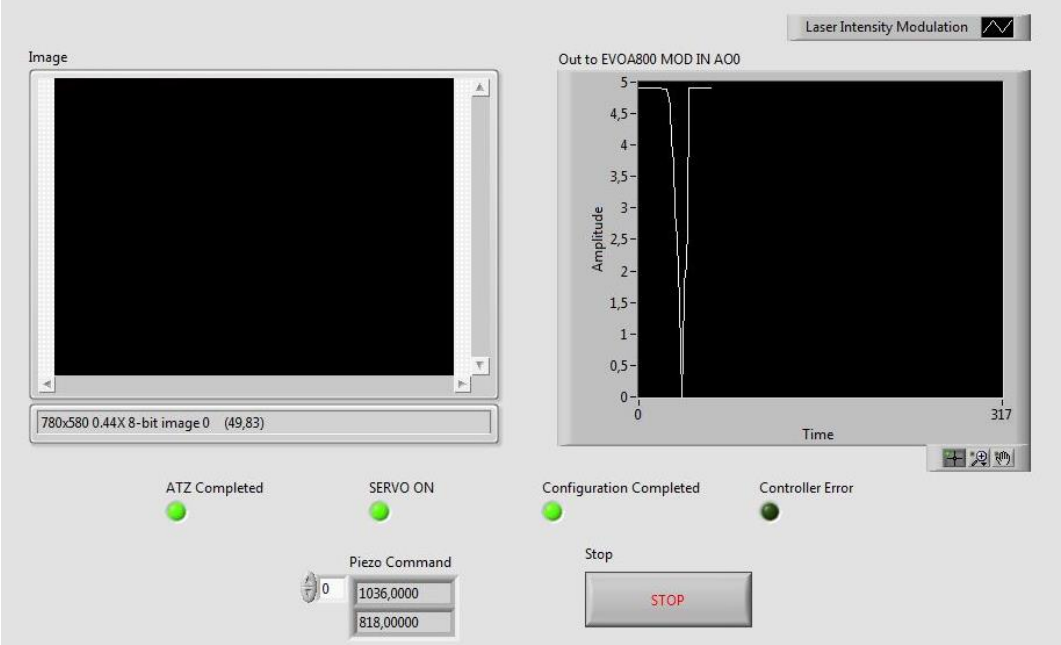

Figure 30. *Experimental Test 1-Front Panel.*

Figure 30 shows the front panel of the control application of the Experimental Test 1. It contains the following terminals:

- the graph “Image” at the top left, which displays the images collected by the breadboard camera. It provides visual feedback about the appearance/disappearance of the source beam to be detected;
- the graph “Out to EVOA800 MOD IN A00” at the top right, which displays the output voltages of the EVO output connector that is directly linked to the NI 9222 module of the CompactRIO. It validates the correct implementation of the power source modulation;
- the “ATZ Completed”, “SERVO ON”, “Configuration Completed” and “Controller Error” boolean terminals, which inform the user about the proper control of the first piezo tip/tilt platform;
- the “Piezo Command” indicator, which displays the output of the <POS?> command string. This shows the current position of the piezo platform’s axes

and provides feedback about the correct mimicking of the dynamics of the laser pointing of the receiving satellite;
- the STOP button, which can arrest the whole simulation.

The results of the Experimental Test 1 can be summarized as follows:

- the dynamics of the laser pointing of the sending satellite were correctly simulated by the implementation of the provided intensity Gaussian law for the power source;
- the dynamics of the laser pointing of the receiving satellite were correctly emulated by the derived displacement law of the piezo tip/tilt platform;
- the proper control of the piezo platform was achieved;
- the proper control of the Electronics Variable Attenuator by the NI 9269 module of the CompactRIO was accomplished;
- no failures occurred.

Thus, the Experimental Test 1 fulfilled all the listed test objectives in 3.1.2.

3.2 Experimental Test 2

3.2.1 Test setup

Same as the Experimental Test 1 (3.1.1).

3.2.2 Test objectives

The test objectives are summarized as follows:

1. to emulate the LISA constellation acquisition until the target identification is achieved (*e.g.*, the pointing stage is not performed). In this phase, laser speckle and secondary sources are not added to the process;
2. to assess the proper function of the detection software and evaluate the centroid of the laser spot;
3. to monitor the state of the system.

3.2.3 Test algorithms

- *Test objective 1.*

  To fulfill the first goal of the Experimental Test 2, the core section of the control application of the Experimental Test 1 (3.1.3) was updated with the integration of the final algorithm (2.4). As explained in 2.4.1, the beam acquisition software shall be applied to the images sampled by the test camera, which replaces the CAS of the receiving spacecraft. Thus, the identification algorithm was added to the "Image Acquisition Loop", which turned into the "Target Acquisition" Timed Loop. This is executed at f_{acq} = 10 Hz and contains the block functions able both to control the image acquisition process and involve the detection software. As the latter is based on a mathematical model which is detailed at the pixel level, at first the LabVIEW Vision Acquisition Software functions convert the camera images to 580x780 matrix arrays. Thus, the final software can scan and analyze them.

  As explained in 2.4, the target acquisition process consists of four steps:

  1. *Ensemble averaging filtering method & Speckle removal*
  2. *Gaussian smoothing filtering method*
  3. *Background Thresholding*
  4. *Centroid Computation*

  The ensemble averaging method and the speckle removal involve simple mathematical operations, such as adding, dividing, and differentiating matrices. Thus, they are implemented by the block functions of the LabVIEW Professional Development System. Conversely, to be consistent with the achieved MATLAB test results (2.4.6), a LabVIEW "Call Library Function Node" calls a dynamic link library (DLL) to execute the remaining steps of the target identification algorithm. To properly synchronize the mimicking of the dynamics of the laser pointing and the beam identification process, the same described "Configuration Completed" flag (3.1.3) enables both the "Target Acquisition" Timed Loop, and the "Laser Modulation Command", and the "Piezo Command" loops. The last two cycles are unchanged with respect to the main VI of the Experimental Test 1.

The following figures show a sketch of the modified section of the breadboard control application.

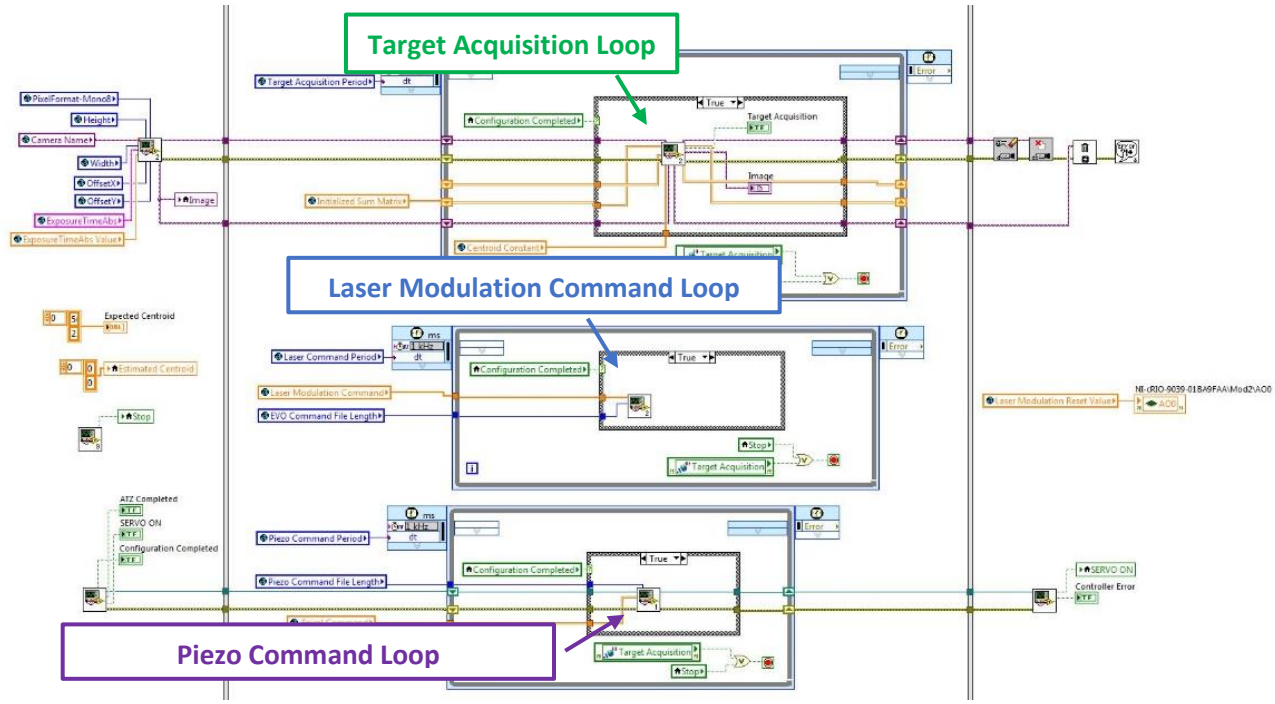

Figure 31. *Control Application of the Experimental Test 2.*

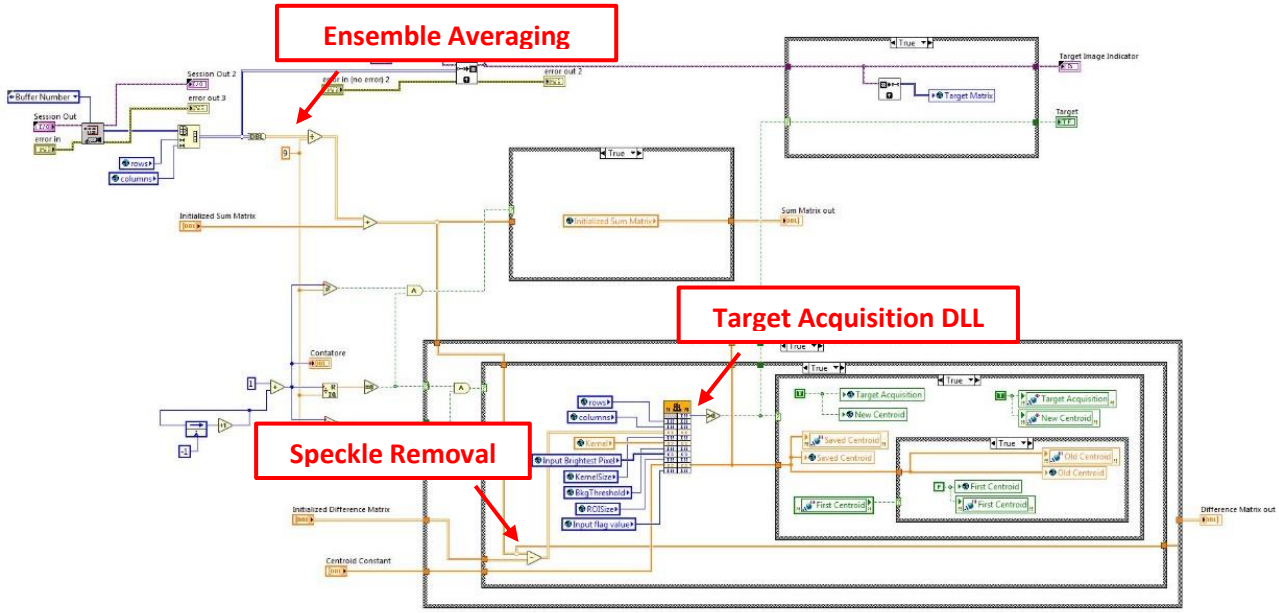

Figure 32. *Sketch of the "Target Acquisition" Timed Loop.*

The output of the developed dynamic link library consists of:

- a boolean indicator called “Target Acquisition”;
- the estimated centroid of the laser spot.

If the beam acquisition is fulfilled, the “Target Acquisition” flag activates, and the spot centroid is saved. If not, the indicator is disabled, and the centroid computation is not performed. In this case, the target position equals its (0,0) default value.

The “Target Acquisition” loop of the Experimental Test 2 stops if one of the following events occurs:

- the user enables the STOP button;
- the “Target Acquisition” flag is activated.

This causes the arrest of all the block functions of the main segment. The initialization and closure stages of the breadboard control application of the Experimental Test 2 are unchanged with respect to the main VI of the Experimental Test 1. The “Camera Settings” subVI and the LabVIEW functions able to close the camera connection are simply directly linked to the “Target Acquisition” loop that replaces the “Image Acquisition” one.

- *Test objective 2.*
  The target detection phase is successfully completed if the following conditions occur:

  - no obvious failures are identified;
  - no errors occur in the camera acquisition process and in the LabVIEW functions that simulate the dynamics of the laser pointing of the sending and the receiving satellites;
  - the “Call Library Function Node” does not display any error dialog box on the front panel;
  - the target beam is identified, and the laser spot estimated centroid is saved. Then, the “Target Acquisition” flag activates. This results in the arrest of the LISA constellation acquisition process;
  - the “Controller Error” flag of the piezo tip/tilt platform is disabled at the end of the simulation.

  The implemented feedback to properly assess the effectiveness of the target identification software are:

  - the “Target Acquisition” boolean indicator;
  - the estimate of the spot centroid. Its value can be compared to the beam’s expected position to verify that no “noise” pixels were erroneously assumed to be part of the target. This results in the validation of the identification final algorithm against the noise levels characterizing the installed hardware and the test environment.

- *Test objective 3.*
  Same as the Experimental Test 1 (3.1.3).

3.2.4 Test results

Figure 33 shows the front panel of the control application of the Experimental Test 2. It contains the following terminals:

- the graph “Image” at the top left, which displays the images sampled by the breadboard camera;
- the “ATZ Completed”, “SERVO ON”, “Configuration Completed” and “Controller Error” terminals, which allow the user to monitor the proper function of the piezo platform;
- the “Target Acquisition” flag, which activates if the source beam identification is achieved;
- the “Estimated Centroid” indicator, which displays the estimate of the detected spot centroid;
- the “Expected Centroid” indicator, which shows the real centroid of the laser beam. Its value is compared to the “Estimated Centroid” to assess the effectiveness of the target identification software;
- the STOP button, which can arrest the whole simulation.

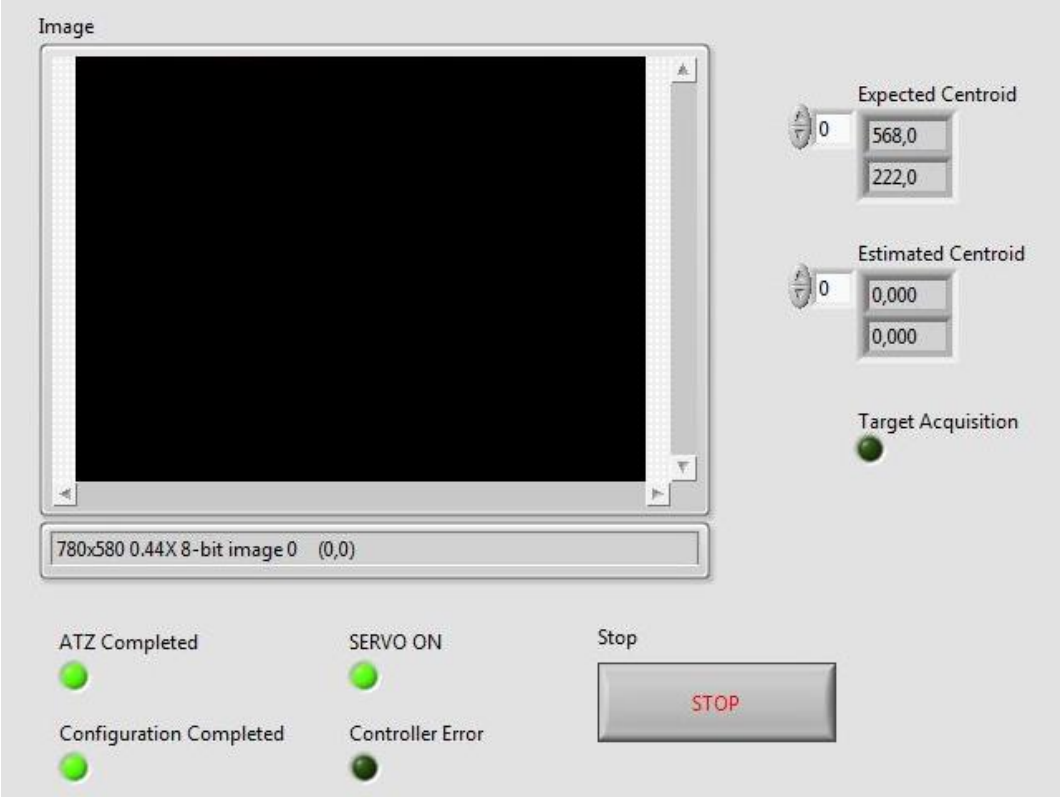

Figure 33. *Experimental Test 2-Front Panel.*

The results of the Experimental Test 2 can be summarized as follows:

- the LISA constellation acquisition until target identification is achieved was correctly simulated;
- the target source beam was identified by the developed acquisition algorithm. The “Target Acquisition” flag activated and caused the Experimental Test to stop. The “Estimated Centroid” was equal to (x_C, y_C) = $(568{,}222)$ pixel. The “Expected Centroid” was $(x_{C,expected}, y_{C,expected})$ = $(568{,}222)$ pixel. Therefore, no “noise” pixels were erroneously assumed to

be part of the target. This results in the validation of the identification software against the implemented noise levels;

- no failures occurred.

Thus, the Experimental Test 2 fulfilled all the listed test objectives in 3.2.2. The results are shown in **Figure 34**.

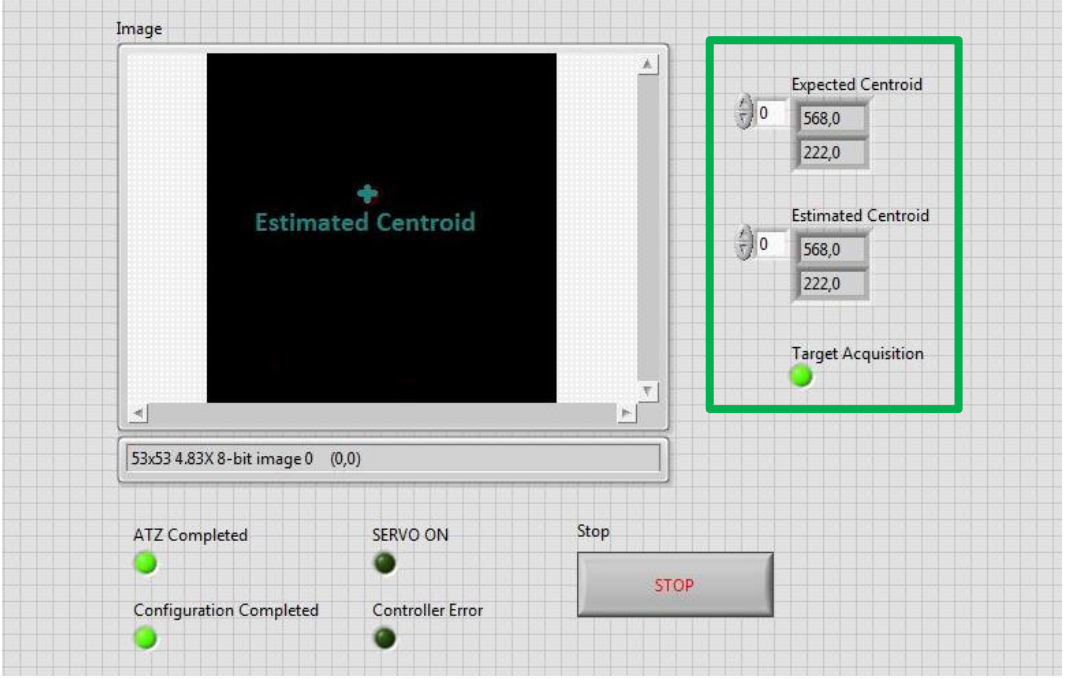

Figure 34. *Experimental Test 2-Results.*

3.3 Experimental Test 3

3.3.1 Test setup

Same as the Experimental Test 1 (3.1.1).

3.3.2 Test objectives

The test objectives are summarized as follows:

1. to simulate the LISA constellation acquisition (*e.g.*, the pointing stage is performed). In this phase, laser speckle and secondary sources are not added to the process;
2. to assess the proper function of the detection software and evaluate the centroid of the laser spot;
3. to validate the centroid correction phase and achieve the LISA mission pointing accuracy;
4. to monitor the state of the system.

3.3.3 Test algorithms

- *Test objective 1.*

  To simulate the whole LISA constellation acquisition, the breadboard control application of the Experimental Test 2 (3.2.3) was updated by emulating the pointing stage. As explained in 2.1.1, the same piezo tip/tilt platform acts in succeeding phases of the constellation acquisition to execute different operations. Until the target identification is achieved, it mimics the dynamics of the laser pointing of the receiving spacecraft. This results in the simulation of the spiral movement of the satellite's FOV. Then, the piezo platform emulates the position correction performed by the receiving satellite's attitude actuators.

  To properly switch from the spiral orbit implementation to the pointing stage, the "Piezo Command" Timed Loop (3.1.3) was modified by the introduction of a boolean flag and an "outer" Conditional Case structure. The command logic indicator is the so-called "Target Acquisition" (3.2.3). Until the light beam is identified, its value equals FALSE: thus, the implementation of the dynamics of the laser pointing of the receiving satellite executes continuously. When the source identification is achieved, the "Target Acquisition" flag activates and the tip/tilt platform operation mode changes to the pointing stage. Starting from the first light beam acquisition, this flag remains unchanged to TRUE.
  As the "Target Acquisition" indicator is set to TRUE, the "Laser Modulation Command" and "Target Acquisition" loops are unchanged. Thus, the CompactRIO continues to command the Electronics Variable Attenuator to mimic the dynamics of the laser pointing of the sending satellite, and the camera proceeds to acquire images. Then, the target identification software continues to scan and analyze them, to monitor the movements of the laser spot on the CCD reference system and evaluate the updated centroid.

  A simple scheme of the function of the pointing correction loop is provided in **Figure 35**. As the laser beam is detected, its centroid (x_C, y_C) is accurately determined. Thus, the offset existing between the target reference position

($x_{C,reference}$, $y_{C,reference}$) and the spot current location is evaluated: this is called (Δx_C, Δy_C). The reference centroid ($x_{C,reference}$, $y_{C,reference}$) is introduced in the system control application as a fixed value, representing the pixel on which is expected the FOV of the QPD is centered. It was selected aiming at moving the target spot by 2/3 pixels on the camera CCD, so as not to exceed the tip/tilt range of the piezo platform.

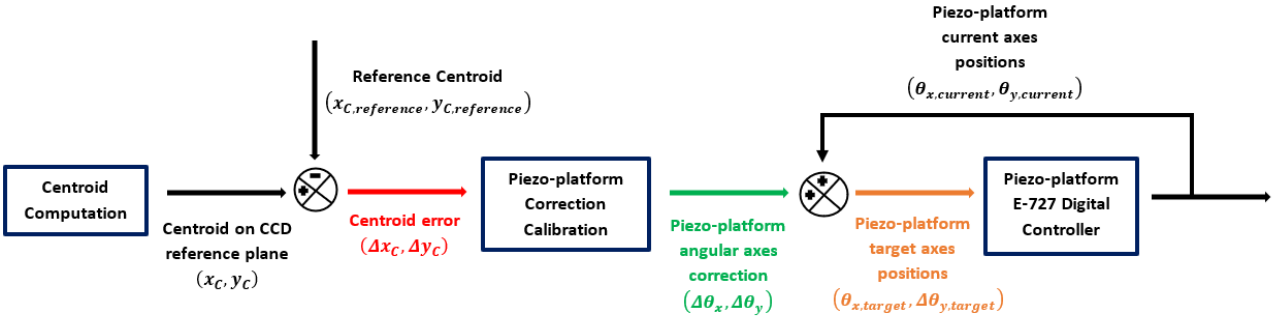

Figure 35. *Pointing Loop.*

The pointing stage shall correct the centroid error (Δx_C, Δy_C). The commands sent to the E-727 digital controller shall be the reference position to be reached by the piezo actuators. Thus, starting from the centroid error, a proper calibration shall be used to derive the angular correction ($\Delta\theta_x$, $\Delta\theta_y$). Then, the resulting value is added to the current axis positions ($\theta_{x,current}$, $\theta_{y,current}$) to obtain the command able to simulate the attitude correction ($\theta_{x,target}$, $\theta_{y,target}$). After executing the pointing adjustment, the closed-loop mode of the tip/tilt platform ensures that the piezo actual position is on the target.

The main issue of the pointing stage was the establishment of the relationship to be used to derive the tip/tilt angular correction ($\Delta\theta_x$, $\Delta\theta_y$). This kind of calibration of the pointing stage was performed by a previous trainee for the same piezo tip/tilt platform installed in the final breadboard. Thus, the results of this work allowed the simulation of the attitude correction phase of the LISA constellation acquisition.

A brief of the pointing calibration theory is provided in the following [15]. The core concept is that the centroid error (Δx_C, Δy_C) is a linear function of the angles of the mirror of the tip/tilt platform. Starting from the small-angles assumptions, this linear relation is written as follows

$$\begin{pmatrix} \Delta x_C \\ \Delta y_C \end{pmatrix} = \begin{pmatrix} \alpha_1 & \alpha_2 \\ \beta_1 & \beta_2 \end{pmatrix} \begin{pmatrix} \Delta\theta_x \\ \Delta\theta_y \end{pmatrix}$$

where α_1, α_2, β_1, and β_2 stand for the linear coefficients. Thus, the change in the orientation of the piezo mirror able to suppress the centroid error is given by

$$\Delta\theta_x = \frac{1}{\alpha_1\beta_2 - \alpha_2\beta_1}(\beta_2\Delta x_C - \alpha_2\Delta y_C)$$

$$\Delta\theta_y = \frac{1}{\alpha_1\beta_2 - \alpha_2\beta_1}(-\beta_1\Delta x_C + \alpha_1\Delta y_C)$$

The matrix coefficients for the calibration of the pointing correction were estimated by a linear regression implemented under LabVIEW software. The following table summarizes the derived values.

Pointing correction calibration coefficients [pixels/μrad]			
α_1	α_2	β_1	β_2
-81.2944	5.80157	7.01052	134.628

Table 21. *Correction calibration coefficients.*

As explained above, when the "Target Acquisition" flag activates, the piezo tip/tilt platform operation mode changes to the pointing stage. At the same time, the target identification software continues to scan the acquired images for updating the spot's current centroid. As the beam power is strongly reduced by the difference operation performed by the first step of the detection algorithm, it is not always possible to identify the transmitting laser (2.4.6), even if it is investing the receiving spacecraft. Thus, starting from the first acquisition there are no continuous updates on the laser spot's current position. Therefore, the pointing correction shall be executed just if a new beam centroid has been estimated by the final algorithm. If not, no angular correction shall be commanded to the piezo tip/tilt platform by the E-727 digital controller. Then, an "inner" LabVIEW Conditional Case Structure (CS) was introduced within the "outer" structure. A proper flag, called "New Centroid", controls the implementation of the inner CS and, thus, the pointing correction. Unlike the "Target Acquisition" indicator, the "New Centroid" value is continuously updated as the output of the target identification software and equals TRUE if a spot new centroid exists.

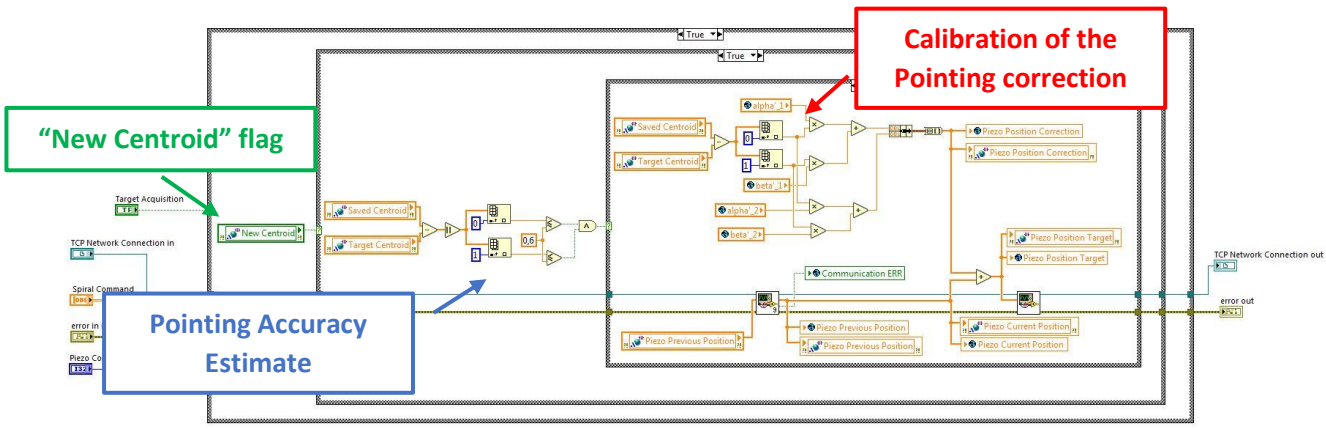

Figure 36*. Sketch of the "Piezo Command" Timed Loop.*

The condition that causes the correction loop to stop is the satisfaction of the pointing requirements. The maximum allowed error is set to 1 μrad, which equals a spot centroid displacement on the CCD reference system of 0.6 pixels. Thus, the desired pointing accuracy is ($\Delta x_{C,target}$, $\Delta y_{C,target}$)≤ (*0.6, 0.6*) pixels. Starting from the first beam identification, when an updated target position is available, the centroid error (Δx_C, Δy_C) is estimated and compared with the desired accuracy. Then, if the pointing precision is not fulfilled, the

attitude correction is performed. If not, the centroid error is assumed to be suppressed. Therefore, the so-called "Right Pointing" boolean indicator activates, the spot centroid is saved, and the LISA constellation acquisition process stops.
Furthermore, the simulation arrests if the user enables the STOP button on the front panel.

Figure 37 shows a sketch of the breadboard modified control application.

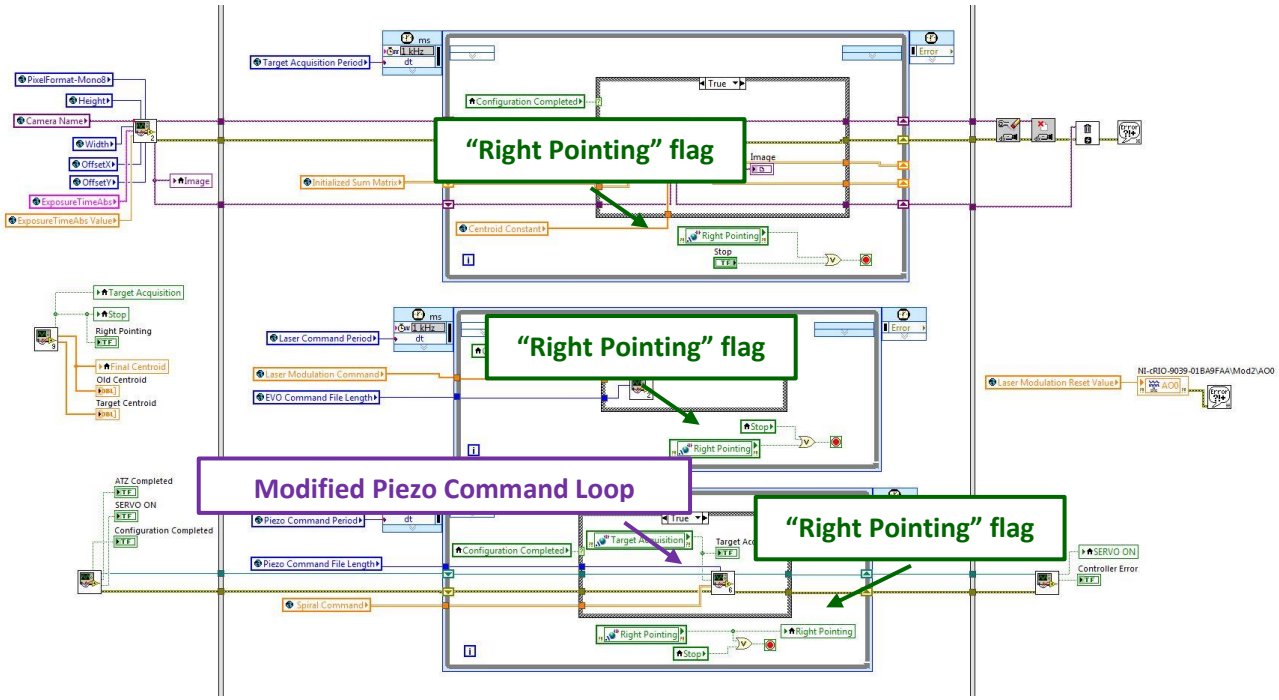

Figure 37. *Control Application of the Experimental Test 3.*

- *Test objective 2.*

The target detection phase is successfully completed if the following conditions occur:

- no obvious failures are identified;
- no errors occur in the camera acquisition process and in the LabVIEW functions able to simulate the dynamics of the laser pointing of the sending and the receiving satellites;
- the "Call Library Function Node" does not display any error dialog box on the front panel;
- the target beam is identified, and the laser spot estimated centroid is saved. Then, the "Target Acquisition" flag activates. This causes the piezo tip/tilt platform's mode to change to the pointing stage.

The implemented feedback to properly assess the effectiveness of the target identification software are:

- the "Target Acquisition" boolean indicator;
- the estimate of the spot centroid. Its value can be compared to the laser beam's expected position to verify that no "noise" pixels were erroneously assumed to be part of the target. This results in the

validation of the identification final algorithm against the noise levels characterizing the installed hardware and the test environment.

- *Test objective 3.*
  The centroid correction phase is successfully completed if the following conditions occur:

  - the piezo tip/tilt platform operation mode changes correctly to the pointing stage when the “Target Acquisition” flag equals TRUE;
  - the pointing correction is executed, and the desired accuracy is achieved. Thus, the “Right Pointing” indicator activates and the LISA constellation acquisition process stops;
  - the “Controller Error” flag of the piezo tip/tilt platform is disabled at the end of the simulation.

  To properly assess the satisfaction of the LISA mission pointing requirements, the following operations are performed:

  - the “Right Pointing” boolean indicator is introduced;
  - the spot centroid is saved. Thus, its value can be compared to the laser beam reference position to estimate the achieved pointing accuracy.

- *Test objective 4.*
  Same as the Experimental Test 1 (3.1.3).

3.3.4 Test results

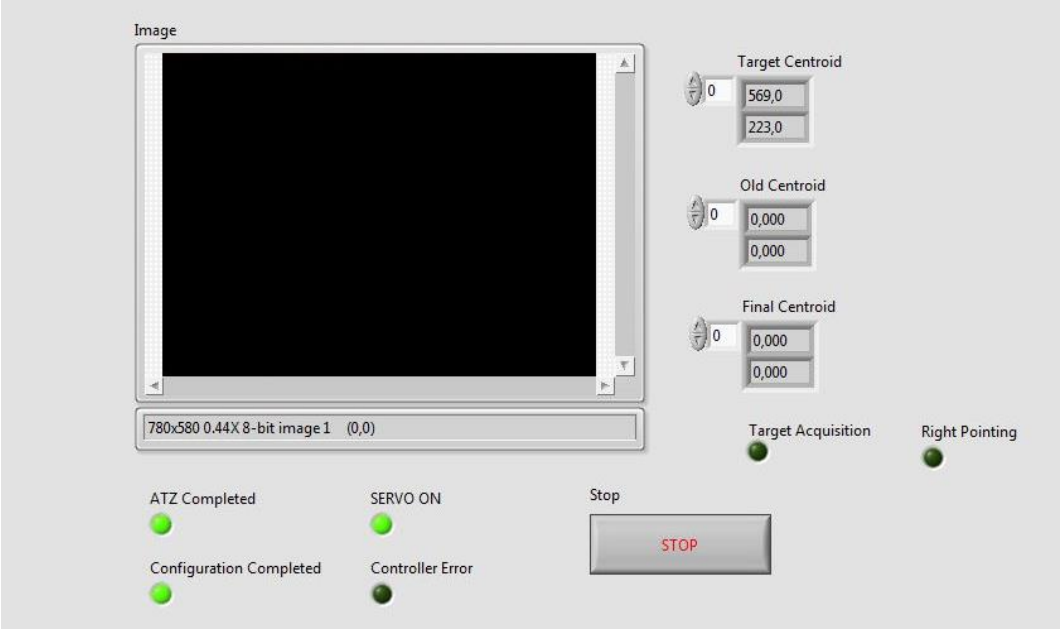

Figure 38. *Experimental Test 3-Front Panel.*

Figure 38 shows the front panel of the control application of the Experimental Test 3. It contains the following terminals:

- the graph “Image” at the top left, which displays the images collected by the test camera. It provides visual feedback about the appearance/disappearance of the beam to be detected. At the end of the simulation, it shows the laser spot starting position and its final centroid (*e.g.*, after pointing is executed);

- the “ATZ Completed”, “SERVO ON”, “Configuration Completed” and “Controller Error” flags, which allow the user to monitor the proper function of the piezo platform;
- the “Target Acquisition” flag, which activates if the target identification is achieved;
- the “Right Pointing” flag, which is enabled if the pointing requirements are satisfied;
- the “Target Centroid” indicator, which represents the reference position to be reached to demonstrate the acquisition link capability;
- the “Old Centroid” indicator, which displays the estimate of the starting position of the detected spot. Its value is compared to the beam expected centroid to assess the effectiveness of the target identification software;
- the “Final Centroid” indicator, which shows the position of the spot centroid after the pointing correction stage. Its value is compared to the “Target Centroid” to verify the satisfaction of the accuracy requirements;
- the STOP button, which can arrest the whole simulation.

The following figure shows the test results.

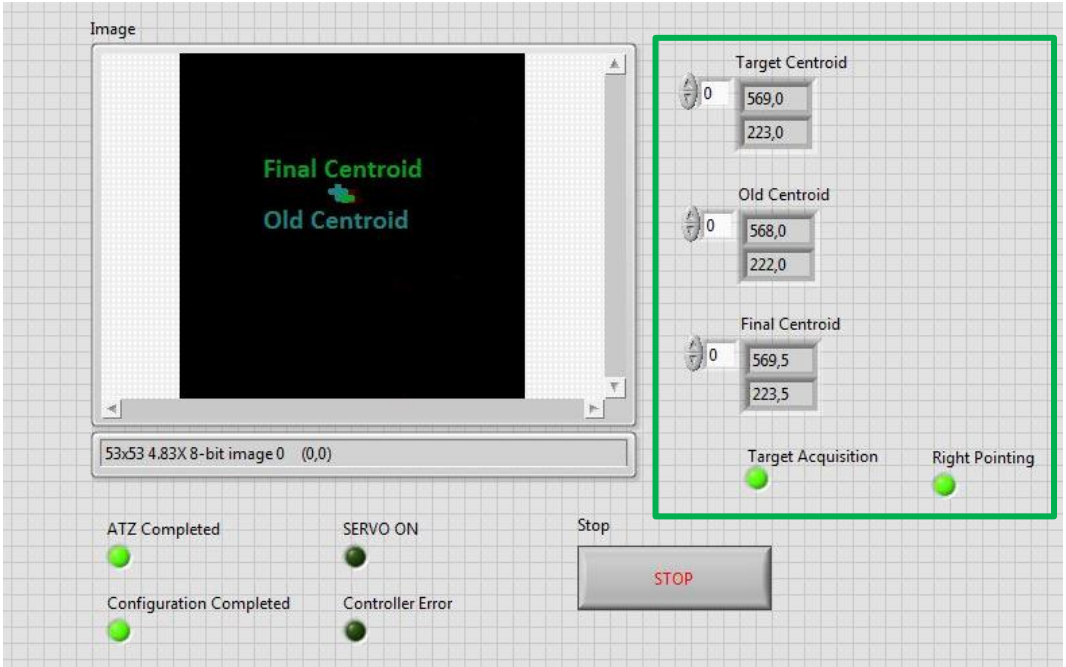

***Figure 39**. Experimental Test 3-Results.*

The results of the Experimental Test 3 can be summarized as follows:

- the LISA constellation acquisition was correctly simulated;
- the target source beam was identified by the developed acquisition algorithm. The “Target Acquisition” flag activated and caused the piezo platform’s mode to change to the pointing stage. The “Old Centroid” was equal to (x_C, y_C) = $(568{,}222)$ pixels. The target spot expected position was $(x_{C,expected}, y_{C,expected})$ = $(568{,}222)$ pixels. Therefore, no “noise” pixels were erroneously assumed to be part of the target;

- the pointing accuracy was accomplished. The pixel representing the FOV of the QPD detector was the “Target Centroid” $(569,223)$. The “Final Centroid” was equal to $\left(x_{C,final}, y_{C,final}\right)$ = $(569.5,223.5)$ pixels and the achieved precision was $(\Delta x_C, \Delta y_C)$ = $(0.5,0.5)$ pixels. Thus, the “Right Pointing” flag activated and caused the simulation to stop;
- no failures occurred.

Thus, the Experimental Test 3 fulfilled all the listed test objectives in 3.3.2.

3.4 Experimental Test 4

3.4.1 Test setup

Same as the Experimental Test 1 (3.1.1).

3.4.2 Test objectives

The test objectives are summarized as follows:

1. to simulate the LISA constellation acquisition. In this phase, the laser speckle is added to the process. Secondary sources are still not considered;
2. to assess the effectiveness of the target identification software when laser speckle is introduced and evaluate the laser spot centroid;
3. to validate the centroid correction phase and achieve the LISA mission pointing accuracy;
4. to monitor the state of the system.

3.4.3 Test algorithms

- *Test objective 1.*

  The control application of the Experimental Test 3 (3.3.3) was updated with the introduction of the laser speckle. Due to the lack of physical components able to mimic the effects of Straylight, "synthetic" images of speckle patterns were used.

  As explained in 2.4, the speckle causes an increase in the shot noise, whose nature is purely random. To properly simulate this augmentation of the noise levels, the "Variables Initialization" subVI was modified: firstly, the block functions of the LabVIEW Professional Development System convert the image of the selected laser speckle pattern to a matrix array. Then, a "Call Library Function Node" calls the "Speckle Generation" dynamic link library. This scans the matrix of the laser speckle and, for each of its pixels, derives the corresponding shot noise. Lastly, this is added to the starting image magnitude.
  The dynamic library generates 10 images of laser speckles, whose shot noise levels are random and different from each other. These 10 frames consist of matrices, whose dimensions are equal to the resolution of the Metrolux camera. Once the speckle generation is completed, these matrices are saved in the so-called "Speckle Global Matrix" array, whose size is 580x7800 pixels.

  Each of the speckle frames within the "Speckle Global Matrix" shall be added to the real image collected by the test camera, to be analyzed by the target identification software. Thus, the actual laser speckle introduction is performed in the core section of the LabVIEW control application, and precisely to the "Target Acquisition" Timed Loop. As the image acquisition frequency is equal to 10 Hz, the "Speckle Global Matrix" is scanned with the same period by a kind of row pointer. This selects one of the 10 speckle frames to add to the sampled image. Then, the resulting matrix is available to be analyzed by the final algorithm. A sketch of the breadboard modified control application is provided in the following.

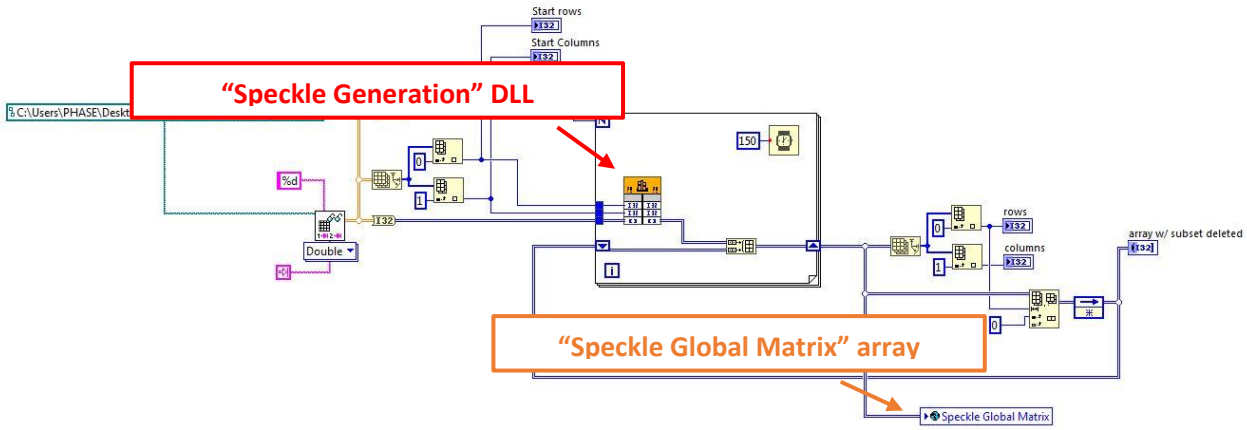

Figure 40. *Sketch of the modified section of the "Variables Initialization" subVI.*

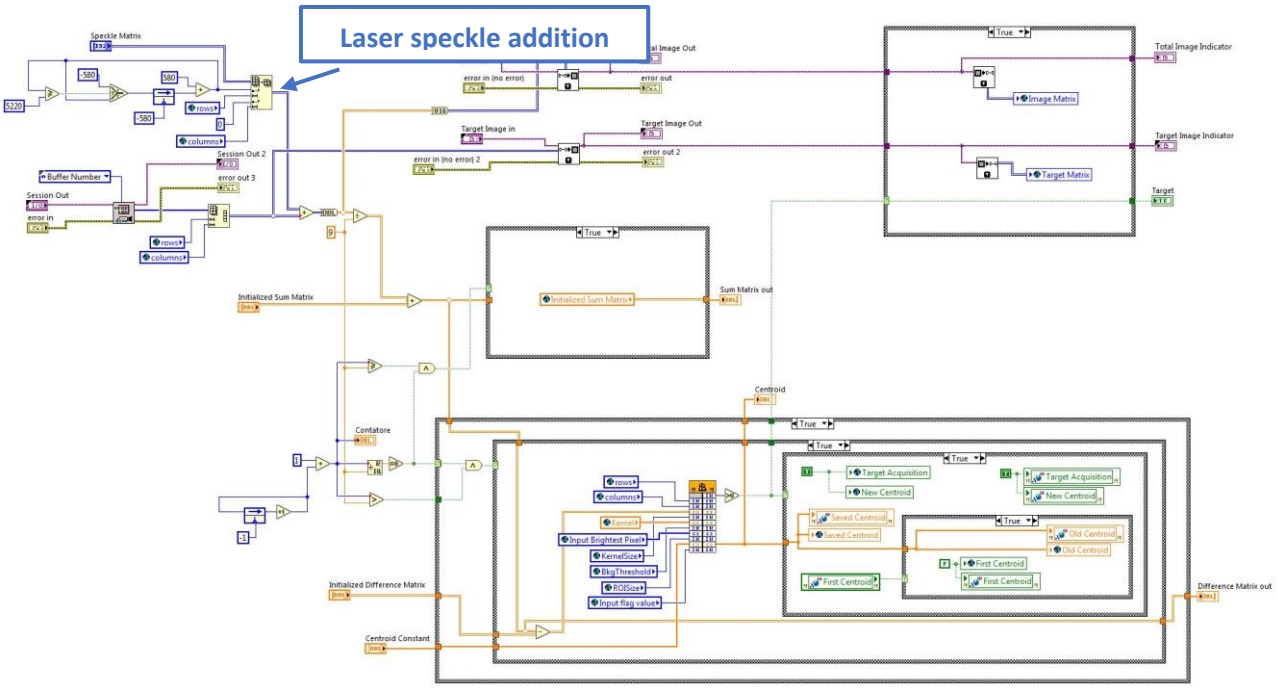

Figure 41*. Sketch of the modified "Target Acquisition" Timed Loop.*

- *Test objective 2.*
  The target detection phase is successfully completed if the following conditions occur:
  - no obvious failures are identified;
  - no errors occur in the camera acquisition process and in the LabVIEW functions able to simulate the dynamics of the laser pointing of the sending and the receiving satellites;
  - the "Call Library Function Node" does not display any error dialog box on the front panel;
  - the target beam is identified, and the laser spot estimated centroid is saved. Then, the "Target Acquisition" flag activates. This causes the piezo tip/tilt platform's mode to change to the pointing stage.

The implemented feedback to properly assess the effectiveness of the target identification software are:

- the “Target Acquisition” boolean indicator;
- the estimate of the spot centroid. Its value can be compared to the beam’s expected position to verify that no “noise” pixels were erroneously assumed to be part of the target. This results in the validation of the identification final algorithm against the noise levels characterizing the laser speckle, the installed hardware, and the test environment.

- *Test objective 3.*
  Same as the Experimental Test 3 (3.3.3).
- *Test objective 4.*
  Same as the Experimental Test 1 (3.1.3).

3.4.4 Test results

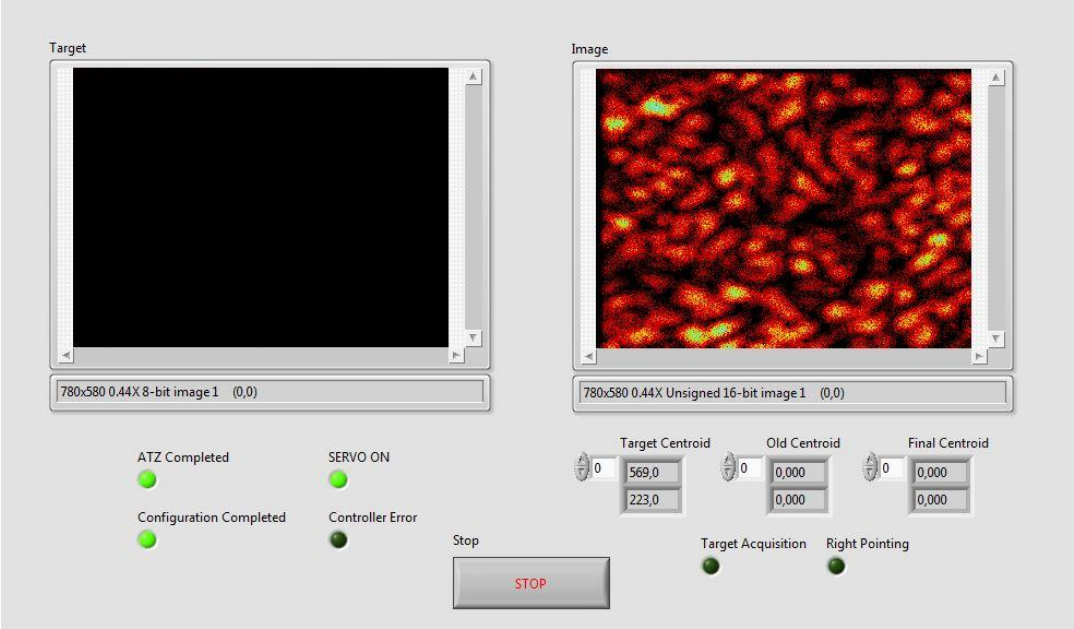

***Figure 42**. Experimental Test 4-Front Panel.*

Figure 42 shows the front panel of the control application of the Experimental Test 4. It contains the following terminals:

- the graph “Target” at the top left, which displays the images sampled by the test camera. It provides visual feedback about the appearance/disappearance of the beam to be detected;
- the graph “Image” at the top right, which displays the images obtained after the laser speckle addition is performed. The selected laser speckle pattern is the “First Speckle Pattern” analyzed in 2.4. At the end of the simulation, this terminal shows the beam starting position and its final centroid;
- the “ATZ Completed”, “SERVO ON”, “Configuration Completed” and “Controller Error” flags;
- the “Target Acquisition” flag, which causes the piezo platform’s mode to change to the pointing stage;

- the “Right Pointing” flag, which is enabled if the pointing requirements are satisfied;
- the “Target Centroid” indicator, which represents the reference position to be reached to demonstrate the acquisition link capability;
- the “Old Centroid” indicator, which displays the estimate of the starting position of the detected spot;
- the “Final Centroid” indicator, which shows the position of the spot centroid after the pointing correction stage;
- the STOP button, which can arrest the whole simulation.

Figure 43 shows the test results.

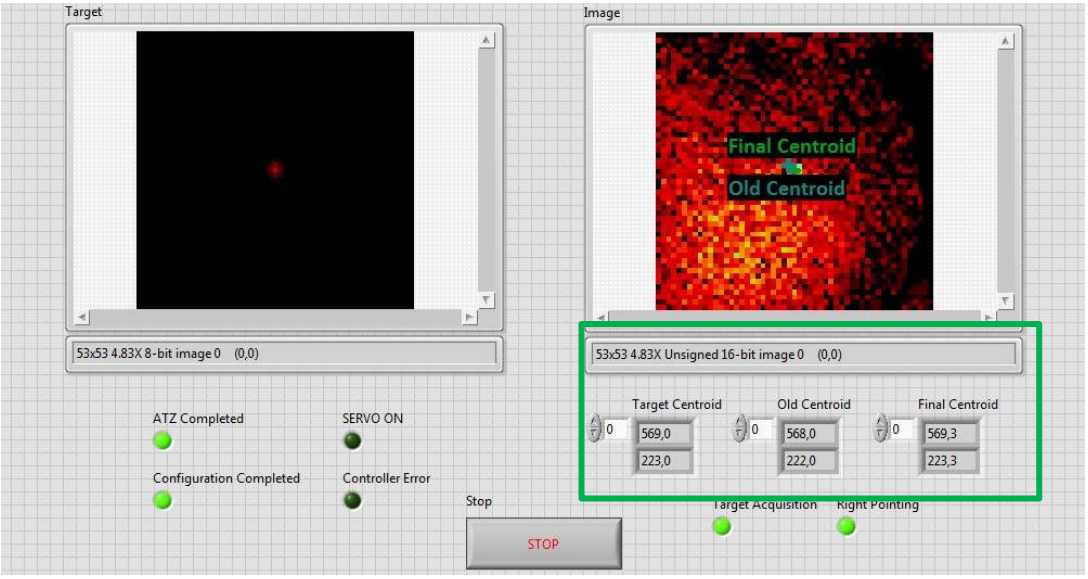

Figure 43. *Experimental Test 4-Results.*

The results of the Experimental Test 4 can be summarized as follows:

- the LISA constellation acquisition was correctly simulated;
- the target source beam was identified by the developed acquisition algorithm. The “Target Acquisition” flag activated and caused the piezo platform’s mode to change to the pointing stage. The “Old Centroid” was equal to (x_C, y_C) = $(568,222)$ pixels. The target spot’s expected position was $(x_{C,expected}, y_{C,expected})$ = $(568,222)$ pixels. Therefore, no “noise” pixels were erroneously assumed to be part of the target. This results in the validation of the identification final algorithm against the noise levels characterizing the laser speckle;
- the pointing accuracy was accomplished. The “Target Centroid” was the same as the Experimental Test 3. The “Final Centroid” was equal to $(x_{C,final}, y_{C,final})$ = $(569.3,223.3)$ pixels and the achieved precision was $(\Delta x_C, \Delta y_C)$ = $(0.3,0.3)$ pixels. Thus, the “Right Pointing” flag activated and caused the simulation to stop;
- no failures occurred.

Thus, the Experimental Test 4 fulfilled all the listed test objectives in 3.4.2.

3.5 Experimental Test 5

3.5.1 Test setup

The setup of the last experimental test is the described final breadboard (2.1.1). All the selected devices were enabled to simulate the LISA constellation acquisition process.

3.5.2 Test objectives

The test objectives are summarized as follows:

1. to simulate the LISA constellation acquisition. In this phase, laser speckle and secondary sources are added to the process;
2. to assess the effectiveness of the target identification software when laser speckle and secondary sources are introduced and evaluate the laser spot centroid;
3. to validate the centroid correction phase and achieve the LISA mission pointing accuracy;
4. to monitor the state of the system.

3.5.3 Test algorithms

- *Test objective 1.*

  Same as the Experimental Test 4 (3.4.3). **Figure 44** shows a sketch of the breadboard final control application.

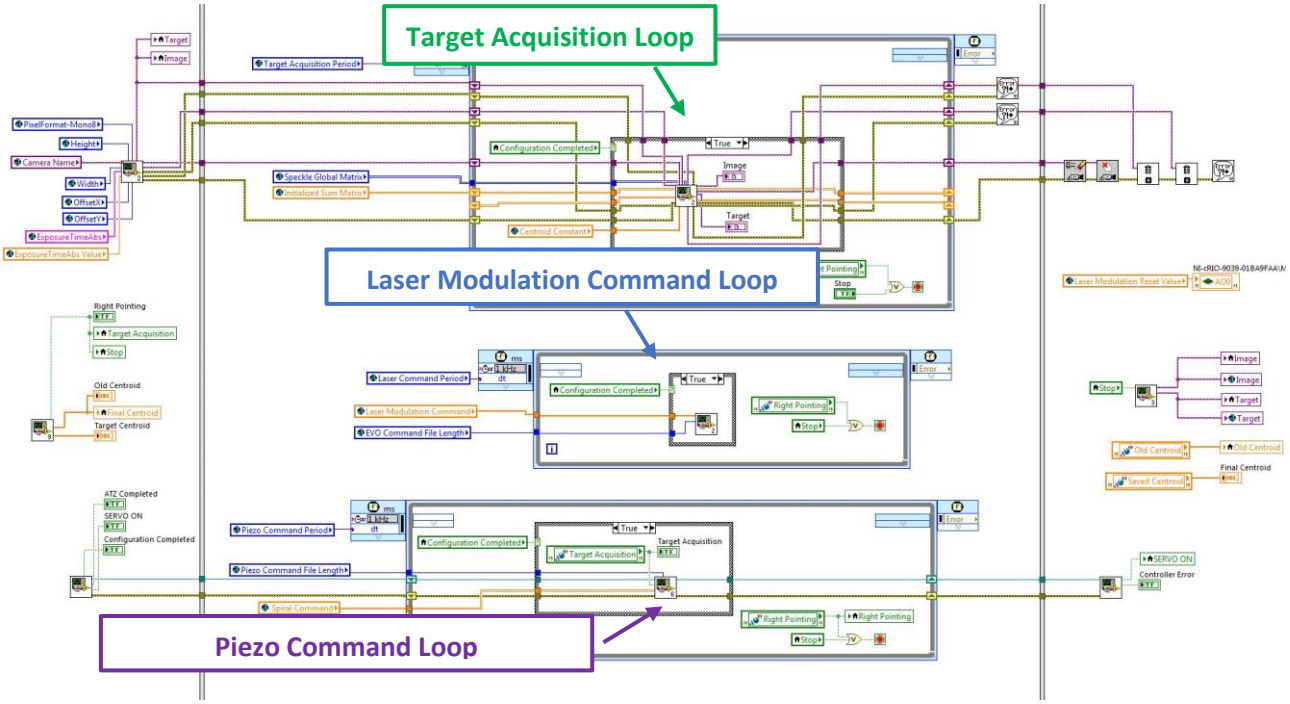

***Figure 44**. Control Application of the test breadboard.*

- *Test objective 2.*

  The target detection phase is successfully completed if the following conditions occur:

  - no obvious failures are identified;
  - no errors occur in the camera acquisition process and in the LabVIEW functions able to simulate the dynamics of the laser pointing of the sending and the receiving satellites;

- the “Call Library Function Node” does not display any error dialog box on the front panel;
- the target beam is identified, and the laser spot estimated centroid is saved. Then, the “Target Acquisition” flag activates. This causes the piezo tip/tilt platform’s mode to change to the pointing stage.

The implemented feedback to properly assess the effectiveness of the target identification software are:

- the “Target Acquisition” boolean indicator;
- the estimate of the spot centroid. Its value can be compared to the beam’s expected position to verify that neither stars nor “noise” pixels were erroneously assumed to be part of the target. This results in the validation of the identification final algorithm against secondary sources, the laser speckle, and the noise levels characterizing the installed hardware and the test environment.

- *Test objective 3.*
  Same as the Experimental Test 3 *(*3.3.3*).*
- *Test objective 4.*
  Same as the Experimental Test 1 (3.1.3).

3.5.4 Test results

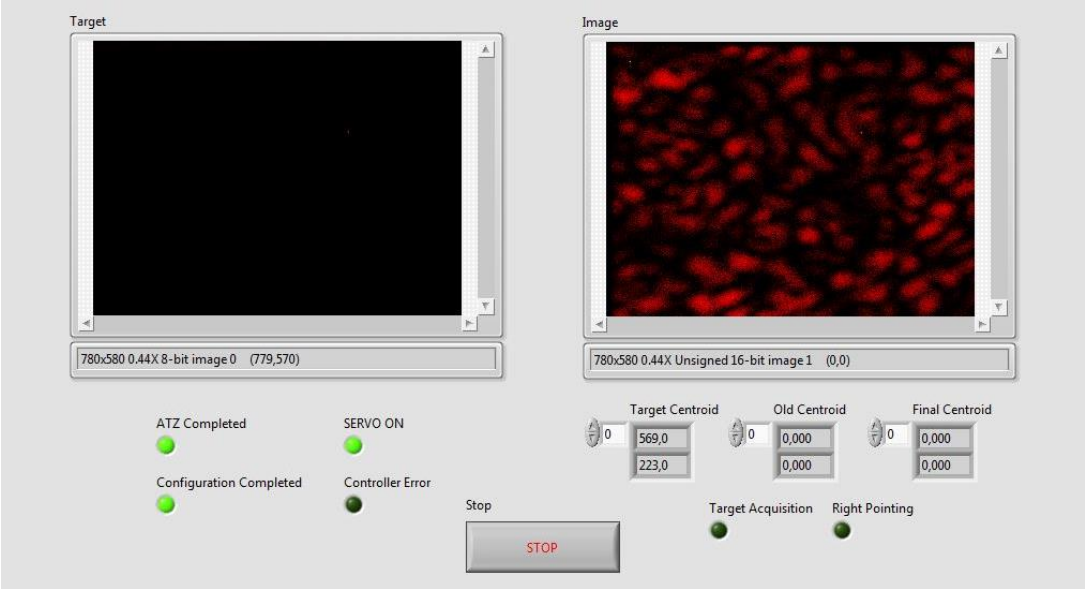

Figure 45. *Experimental Test 5-Front Panel.*

Figure 45 shows the front panel of the control application of the Experimental Test 5, which is the same as the Experimental Test 4.

The test results are provided in **Figure 46** and can be summarized as follows:

- the LISA constellation acquisition was correctly simulated;
- the target source beam was identified by the developed acquisition algorithm. The “Target Acquisition” flag activated and caused the piezo platform’s mode to change to the pointing stage. The “Old Centroid” was equal to $(x_C, y_C) = (568,222)$ pixels. The target spot’s expected position was

$(x_{C,expected}, y_{C,expected})$ = (568,222) pixels. Therefore, neither stars nor "noise" pixels were erroneously assumed to be part of the target. This results in the validation of the identification final algorithm against the secondary sources;

- the pointing accuracy was accomplished. The "Target Centroid" was the same as the Experimental Test 4. The "Final Centroid" was equal to $(x_{C,final}, y_{C,final})$ = (569.5,223.2) pixels and the achieved precision was $(\Delta x_C, \Delta y_C)$ = (0.5,0.3) pixels. Thus, the "Right Pointing" flag activated and caused the simulation to stop;
- no failures occurred.

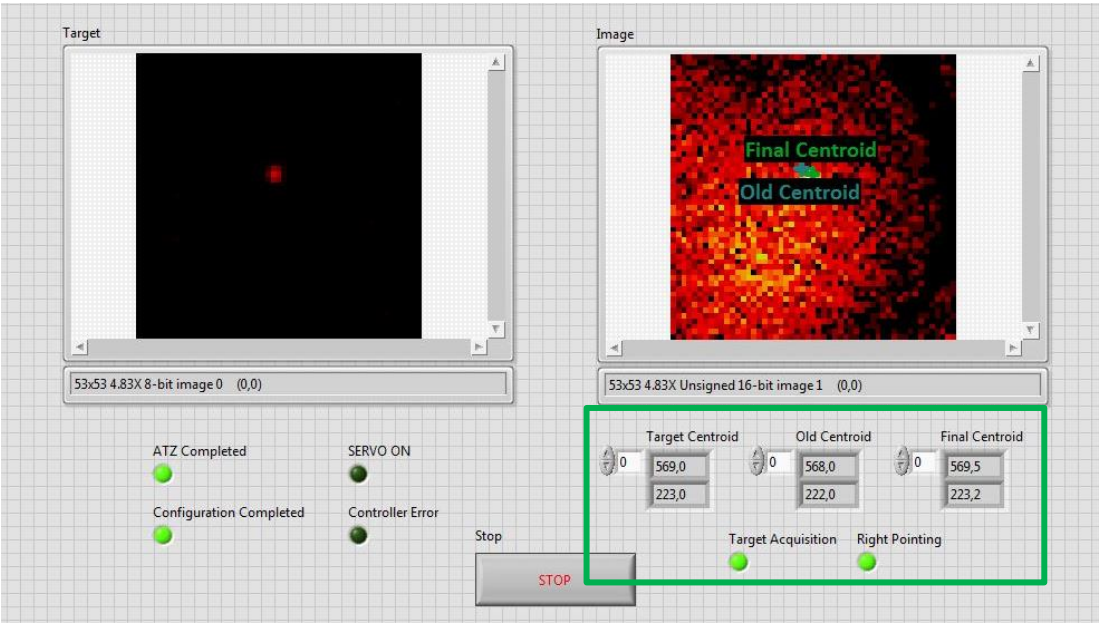

Figure 46. *Experimental Test 5-Results.*

Thus, the Experimental Test 5 fulfilled all the listed test objectives in 3.5.2.

Conclusions & Recommendations

The last chapter summarizes the major achievements of this paper.
The main goal was the realization and the validation of a breadboard able to simulate the LISA constellation acquisition, from the transmitting satellite's scanning phase to the attitude correction stage, which is performed to center the detected spot on the FOV of the QPD sensor. Furthermore, the link acquisition capability should be demonstrated in representative conditions, such as:

- detection of sub-picowatt variable beams;
- different noise sources (*e.g.*, background, Straylight, electronics);
- secondary sources (*e.g.*, stars).

To achieve the primary goal of this thesis, the following devices were added to the list of components of the basic setup (1.2):

- a Variable Beam Attenuator and a Single-Mode Fused Fiber Optic Coupler, to attenuate the laser source until achieving the power level characterizing the transmitting source, which is significantly reduced by the inter-spacecraft distance;
- a secondary laser source, to simulate a star in FOV of the receiving satellite's CAS, triggering the target identification software.

The second chapter (2.1.1) describes the hardware configuration of the final breadboard. Due to the lack of physical devices able to emulate the laser speckle random intensity distribution, synthetic speckle images were introduced, aiming at reproducing the LISA mission noisy environment. The test breadboard control application was programmed in LabVIEW, and the final setup was fully controlled by the Windows-based workstation of the *Optics Lab*.

The third chapter demonstrates the validation of simulation. The major achievements of the final breadboard can be summarized as follows:

- to simulate the dynamics of the laser pointing of the sending satellite by translating the spiral orbit of the platform into an intensity Gaussian law for the primary laser source. The power modulation control is accomplished using an Electronics Variable Attenuator directly controlled by the cRIO platform;
- to mimic the spiral movement of the FOV of the receiving satellite's CAS by translating the platform's orbit into a displacement law for the first piezo tip/tilt platform. The speed of the receiving spacecraft's scanning manoeuvre is correctly emulated by scaling the control angles according to the specifications of the test camera;
- to simulate secondary sources able to trigger the target acquisition process. This goal is accomplished by the introduction of a second laser source;
- to emulate the characteristics of the LISA mission noisy environment by the introduction of synthetic images of the laser speckle;
- to identify the target source beam by integrating the developed laser beam acquisition software (2.4);
- to simulate the receiving satellite's attitude actuators pointing correction that allows the proper centering of the detected beam on the FOV of the QPD detectors. The centroid

offset suppression is performed by deriving the tip/tilt angular correction to be sent to the digital controller of the piezo platform through an effective calibration law, and the required pointing accuracy is achieved.

In conclusion, the final breadboard can effectively simulate the LISA constellation acquisition from the optical point of view.

The second primary objective that is accomplished by the validation of the test system is the assessment of the effectiveness of the developed target identification software. It consists of four steps:

- *Ensemble averaging filtering method & Speckle removal;*
- *Gaussian smoothing filtering method;*
- *Background thresholding;*
- *Centroid Computation.*

The test results (3.2.4*,* 3.3.4*,* 3.4.4, 3.5.4) show how the proposed algorithm can guarantee the proper identification of a weak-light beam embedded in a strongly noisy environment. For each of the performed Experimental Tests, the output centroid is always almost equal to the beam's expected position (view **Figure 33**, **Figure 39**, **Figure 43**, **Figure 46**): therefore, neither stars nor "noise" pixels were erroneously assumed to be part of the target. This demonstrates the effectiveness of the selected noise mitigation and Signal-to-Noise ratio enhancement techniques and results in the validation of the identification software against secondary sources, the laser speckle, and the noise levels characterizing the installed hardware and the test environment.

To properly assess the effectiveness of the target identification algorithm, two critical issues shall be analyzed:

- *Centroid computation accuracy*
  As explained in the second chapter, to satisfy LISA strict pointing requirements, the precision of the centroid computation shall be ≤0.1 pixels. The performance analysis of the target identification algorithm (2.4.6) demonstrates how both the Gaussian smoothing and the background thresholding steps produce the loss of valuable detection information. This affects the accuracy of the improved centroid computation method (view **Table 19**). The 2-D convolution process induces some changes in the target matrix magnitude distribution, but this does not prevent the satisfaction of the precision requirements (view **Table 18**). Conversely, the threshold operation causes the suppression of the less intense target spot pixels. This results in the cancellation of their contribution to centroid computation, causing the failure to satisfy the centroid computation specifications. To ensure the satisfaction of the LISA mission pointing requirements, the beam position shall be estimated by applying the improved method to the images resulting from the Gaussian filtering step. Thus, in the final software, the background thresholding step is executed to suppress the remaining shot noise peaks after the smoothing filtering. Then, the resulting image is scanned to search for the brightest pixel. If the resulting pixel differs from $(0,0)$, the laser spot is identified, and the centroid computation is executed on the image emerged from the Gaussian smoothing step. If not,

the beam position is not estimated. The proper functioning of the target acquisition software is shown in the following figure.

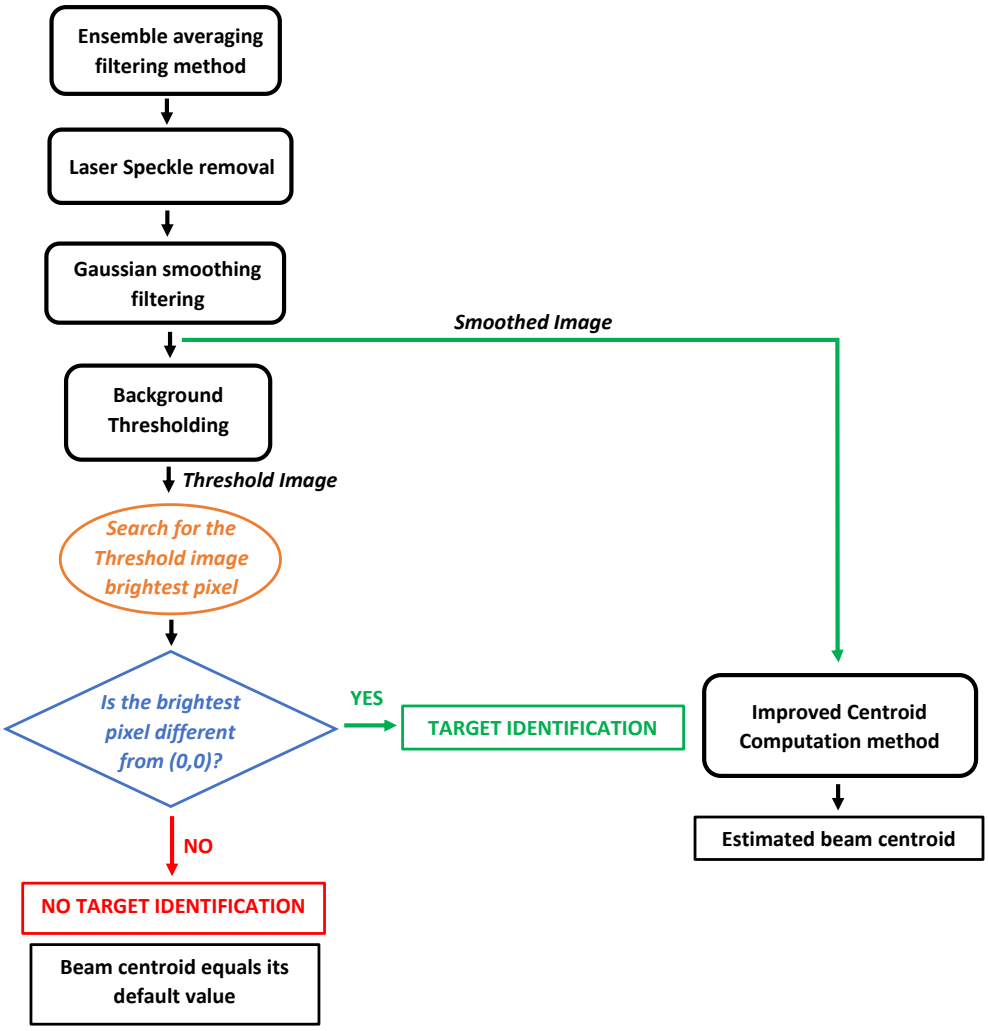

Figure 47. *Target identification software-Flowchart.*

- *Computational cost assessment*

  As explained in the first chapter (1.2.1), to properly guarantee the success of the LISA constellation acquisition, the search for the target beam and the centroid computation shall be performed in real-time. Therefore, the computational cost of the suggested software was determined. This estimate was obtained by running the identification algorithm for an image whose dimensions were equal to the resolution of the test camera. The resulting computational cost is approximately equal to $80ms$, of which about $60ms$ are caused by the Gaussian smoothing filtering step. As explained in the second chapter (2.4.1), the image acquisition frequency is f_{acq} = $10Hz$. Thus, two subsequent frames are sampled at a time distance of $100ms$. For the LISA application case, the need for noise mitigation and speckle removal causes the acquisition algorithm to be applied on the frame resulting from the difference between the images obtained by averaging two sets of 9 frames. Thus, the time distance between two subsequent images scanned by the target acquisition software is equal to $900ms$, which is much greater than the time needed to search for the new spot centroid. Therefore, the developed beam identification algorithms can cope with the real-time requirements of LISA.

In conclusion, the thesis objectives are accomplished by the proposed solution. The most critical step of the target acquisition software is the background thresholding, which is crucial to guarantee the proper operation of the constellation acquisition. As explained in 2.4.4., the threshold was selected by testing, starting from the analysis of the brightness of noise pixels remaining after Gaussian filtering. This study was conducted applying the first two steps of the detection algorithms on images containing just noise sources (*e.g.*, laser speckle and related shot noise). Due to the random nature of shot noise, the threshold value needed to suppress the remaining noise peaks after smoothing filtering is difficult to estimate a priori. The most robust strategy is based on an experimental evaluation of the residual noise intensity. This shall be performed during the calibration stage of the LISA mission before turning on the laser systems, so as not to alter the results of the noise estimate.

Starting from the description of the major achievements, some recommendations and suggestions for future improvements have been identified:

- to modify the hardware configuration of the final breadboard (2.1.1) aiming at the introduction of a device capable of physically simulating the laser speckle. This results in greater representativeness of the test system;
- to execute a rigorous Straylight analysis to evaluate the exact amount of reflected radiation that originates the laser speckle and de-normalized the analyzed random intensity patterns;
- to control the second piezo tip/tilt platform to simulate the transmitting satellite's platform jitter. This results in the analysis of the effects of the fluctuations of the beam intensity;
- to optimize the developed target identification software by introducing more effective noise mitigation and Signal-to-Noise enhancement techniques against the shot noise. This results in a reduction of the background threshold value, which causes the decrease of the signal average minimum intensity level the acquisition process can identify. This implies greater effectiveness of the software in the acquisition of weak signals;
- to optimize the parameters of the proportional-derivative control law of the closed-loop operating mode of the piezo tip/tilt platform, aiming at the stabilization of the pointing accuracy.

The validation of a breadboard able to simulate the LISA constellation acquisition leads the way to the know-how about the strict pointing and stability requirements introduced by the new generation of space optical payloads. The benefit of these applications is the capability of achieving precision at the level of the μrad or a fraction of it, typically on a platform whose stability can be thousands of times larger. However, the need for pointing stabilization and disturbances rejection implies the development of novel strategies and hybrid architectures to achieve both high-frequency vibrations suppression and beacon tracking.

The LISA mission, with specific application to the issue of constellation acquisition, is the best present paradigm of this evolution of optical pointing. Thus, the proposed work fits perfectly into the context of the development of a Pointing, Acquisition & Tracking prototype with the potential to achieve the strict pointing requirements characterizing the space optical payloads.

References

1. Hamid Hemmati, *"Deep Space Optical Communications"*, Deep space communications and navigation series, Jet Propulsion Laboratory California Institute of Technology, 2006
2. Oliver Jennrich, *"LISA technology and instrumentation"*, Class. Quantum Grav., 2009
3. P. Amaro-Seoane, et al, *"LISA Laser Interferometer Space Antenna: a proposal in response to ESA call for L3 mission concepts"*, 2017.
4. Noé Charpigny, *"An Executable System Model for Behavioural Analyses of the LISA Mission"*, Degree project in vehicle engineering, 2019
5. Francesca Cirillo, Peter F. Gath, *"Control System Design for the Constellation Acquisition Phase of the LISA Mission"*, Journal of Physics: Conference Series 154, 2009
6. John Goodman, *"Statistical properties of laser speckle patterns"*, Topics in Applied Physics, 1975
7. Ruihong Gao, Heshan Liu, Ya Zhao, Ziren Luo, Gang Jin, *"High-precision laser spot center positioning method for weak light conditions"*, Applied Optics Research Article, Vol. 59, No. 6, 2020
8. John Canny, *"A Computational Approach to Edge Detection"*, IEEE Transaction on pattern analysis and machine intelligence, Vol. PAMI-8, 1986
9. Gao Jie, Liu Ning, *"An improved adaptive threshold canny edge detection algorithm"*, International Conference on Computer Science and Electronics Engineering, 2012
10. Weibin Rong, Zhanjing Li, Wei Zhang and Lining Sun, "*An Improved Canny Edge Detection Algorithm*", IEEE International Conference on Mechatronics and Automation, 2014
11. Tom Thomas, *"Ensemble Averaging Filter for Noise Reduction"*, International Journal of Advanced Research in Computer and Communication Engineering, Vol. 5, Issue 8, 2016
12. Moo K. Chung, *"Gaussian Kernel Smoothing"*, University of Wisconsin-Madison, 2012
13. Matthew Brett, https://matthew-brett.github.io/teaching/smoothing_intro.html, "An introduction to smoothing", 2014
14. John C. Bancroft, *"Introduction to matched filters"*, CREWES Research Report, Vol. 14, 2002
15. Choimet Vianney, *"Acquisition, Tracking and Pointing Systems",* Research Internship Report, 2019